Warpage analysis on power module ceramic substrates

Master Thesis

Chieh Wang

TU Delft

Warpage analysis on power module ceramic substrates

MSC Thesis

by

Chieh Wang

Student Number:	5469635	
Defense date:	31st August, 2023	
Thesis committee:	Dr. René Poelma	Nexperia
	Prof. Dr. Guoqi Zhang	TU Delft
	Dr. Tomás Manzaneque	TU Delft
	MSc Dong Hu	TU Delft
Faculty :	Electrical Engineering, Mathematics Computer Science (EEMCS)	
Institution:	Delft University of Technology	

TU Delft

Abstract

This study deals with the challenge of warpage in power modules, vital components in the rapidly expanding electric and hybrid-electric vehicle industry. The variations in temperature during manufacturing, resulting in significant warpage changes, contribute to device cracks, delamination, and reduced reliability.

The primary focus is understanding and mitigating the warpage phenomenon in power module substrates. This warpage is induced by thermo-mechanical stresses during the assembly packaging process. The investigation begins by exploring the cause of warpage change by characterizing annealed copper properties and employing 2D finite element model (FEM) analysis. The study identifies plastic strain as the dominant cause of warpage change during process steps. Subsequently, a validated 3D FEM simulation model is developed to replicate practical annealing and sintering processes. Lastly, the project delves into factor analysis to identify critical variables influencing warpage. It underscores that balancing residual copper volume is crucial in warpage reduction. Additive and subtractive manufacturing techniques establish a correlation between the removal of copper volume and warpage reduction.

This project provides comprehensive insights into the manufacturing process of AMB substrate, warpage behavior, and effective strategies for reduction, constructing a solid foundation for future manufacturing and design.

Keywords: Power modules, AMB substrate, Warpage, Finite element model, Sintering, Additive technology, Subtractive technology

Acknowledgement

I extend my heartfelt gratitude to the individuals whose contributions have made this project possible. First and foremost, I am thankful to Dr. René Poelma for providing me with the invaluable opportunity to collaborate on this project with Nexperia. Your guidance, insightful discussions, and constructive feedback have been instrumental in shaping this project. I deeply and genuinely appreciate Dong Hu's consistent support and guidance throughout the project. The discussions with you have been pivotal in defining the project's direction, enriching its content, and offering constant encouragement to keep pushing forward. To Zichuan Li, I sincerely thank you for your extensive support in mechanical theory insights and discussions related to FEM simulation. Your input has greatly enriched the project's depth and understanding. I am also grateful to Professor Guoqi Zhang for granting me the opportunity to conduct my thesis research under the Electronics Components Technology and Materials (ECTM) research group. Your guidance and suggestions have been invaluable for the project's improvement.

I am thankful to Else Kooi Laboratory (EKL) for providing access to Class 100 cleanroom facilities and MEMs Lab resources for my experiments and measurements. My gratitude extends to the entire EKL team for their support. Special thanks to Ton Riemslag and Nico Geerlofs from the Department of Material Science for their assistance conducting material properties experiments and engaging in insightful discussions. I extend my appreciation to Bert Bakker from DEMO for helping me conduct the manufacturing process of milling the substrate. I am grateful to Roy Awater and Andrei Anisimov for providing access to the TMA and Keyence equipment, which were essential in completing the experiment. Thanks to Dr. Jiajie Fan, Cheng Qian, and Xuyang Yan from Shanghai Fudan University for your collaboration in the material properties experiment. I also want to acknowledge Nikhil Gupta from the ECTM department for engaging in discussions and supporting the project.

Lastly, I express my profound gratitude to my family and friends, who have consistently provided unwavering support and motivation throughout my journey. My deepest thanks go to my parents for allowing me to pursue my Master of Science studies at TU Delft University.

Chieh Wang
Delft, August 2023

Contents

List of Figures

List of Tables

1

Project Introduction

The automotive market has grown significantly with the progress of technology and the development of society. To promote a sustainable and environmentally friendly environment, electric vehicles (EV) and hybrid-electric vehicles (HEV) are penetrating the transportation market [1]. However, efficient energy conversion in the automotive industry requires integrating various semiconductor power components and constructing a packaging containment system for power modules [2]. The power module system operates at high power densities (over 200kW), voltage ratings (more than 800V), and current levels to ensure high performance and efficiency [3]. Thus, it is crucial to establish a packaging structure that facilitates fast and accurate electrical signal transportation, provides solid mechanical support, and guarantees high water and dust protection reliability. The packaging structure of typical power module devices is illustrated in Fig. 1.1.

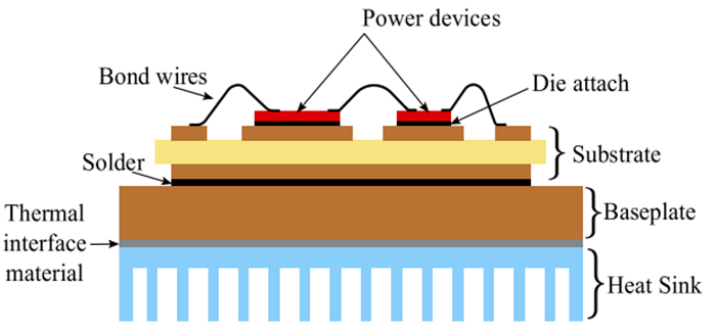

Figure 1.1: Schematic of the packaging structure of typical power module [3]

The device comprises multiple material layers, including a heat sink for thermal dissipation, a baseplate that provides structural support, a substrate for signal transportation or isolation, and a die that houses the integrated circuit. In junction with metal and ceramic layers, the substrate serves as the primary physical and electrical connection between the die and baseplate. The project's primary focus is understanding the substrate's warpage caused by thermo-mechanical stresses throughout the manufacturing process by using a finite element simulation model (FEM) and aiming to minimize this warpage

by employing additional manufacturing techniques.

1.1. Motivation and problem statement

Warpage, an out-of-plane deformation caused by unconventional bending or distortion, can occur due to stress differences based on the manufacturing process. In the substrate of power module devices, multiple metal and ceramic layers of varying thicknesses with different coefficients of thermal expansion (CTE) are stacked on top of each other. Significant temperature differences can arise during manufacturing and operation, leading to warpage. Warpage is a critical issue as it can introduce microcracks in the brittle ceramic layer and the delamination of the solder-substrate interface. Figure 1.2 shows examples of these defects. These defects impair electrical signal transportation, decrease heat dissipation rate, compromise device reliability, reduce the device's lifetime, lower production line efficiency, and increase costs [4]. Therefore, effective warpage management is essential in power module device design and manufacturing. Moreover, the literature on the cause of warpage during the manufacturing process of double-sided AMB substrates currently needs to be improved in its detailed physics theory explanations. Also, it lacks warpage-controlling models for double-sided AMB substrates with validated experimental results.

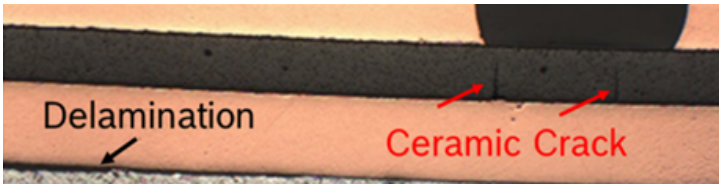

Figure 1.2: Ceramic crack and solder delamination [5]

The thesis aims to investigate the causes of warpage resulting from the manufacturing process, which induced thermo-mechanical stresses. Additionally, the study focuses on conducting simulation and experimental validation studies to determine how substrate pattern design and manufacturing techniques can effectively control the warpage of ceramic substrates.

1.2. Thesis objectives

The primary objective of the project is to provide a comprehensive understanding of the causes of warpage in power module devices and develop effective strategies to manage the warpage. The following are the research topics that will be discussed:

- Interpret physical theories related to the causes of warpage change.
- Investigate the primary factors of substrate design that affect warpage.
- Determine the influence of substrate pattern design by doing additive or subtractive manufacturing experiments.
- Analyze the influence of the sintering process on warpage.
- Validate the simulation results by comparing them with experimental data

1.3. Approach

The primary focus of this project is to investigate the factors driving warpage and achieve warpage reduction in AMB substrates. The approach involves utilizing simulation software to identify influential variables, optimizing substrate design, and validating the findings through additive and subtractive technology and annealing experiments. To attain the project objectives, the strategies can be categorized into three distinct but interconnected approaches: the experimental approach, the simulation approach, and the optimization approach, each contributing essential insights to achieve the research objectives. Figure 1.3 depicts the main approaching steps of the project.

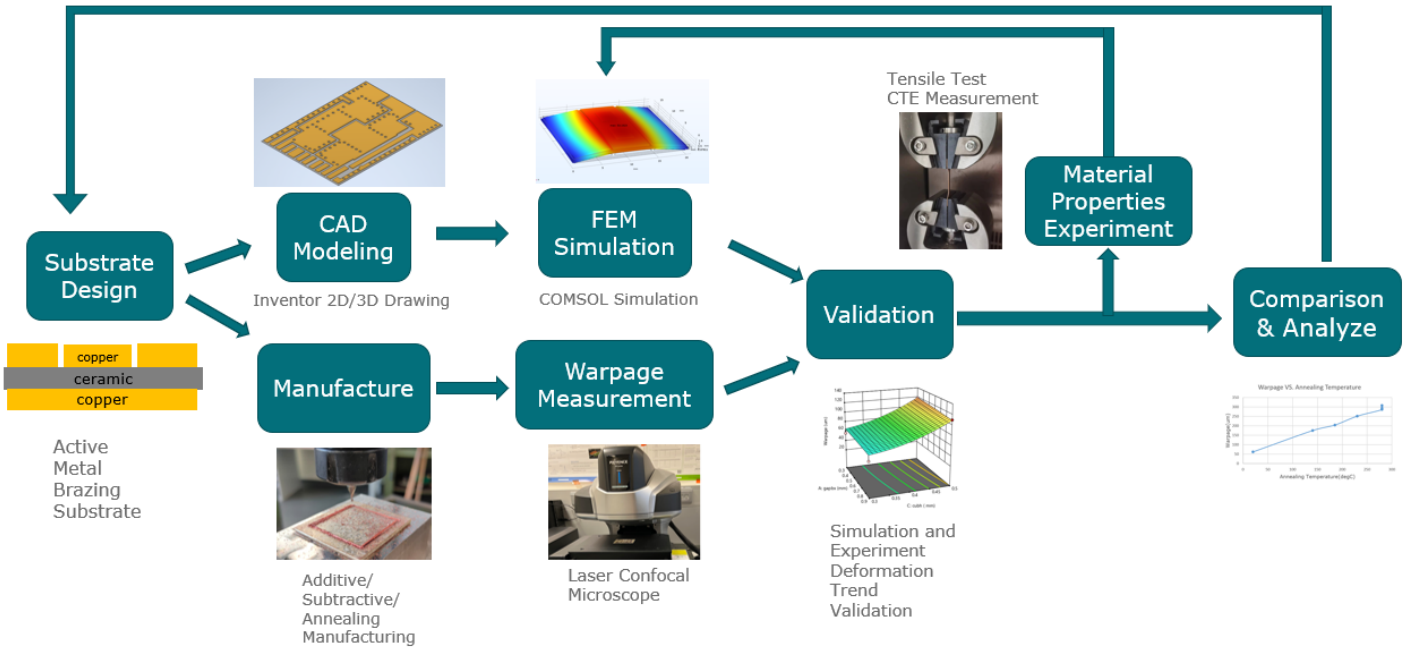

Figure 1.3: Main approaching steps in warpage analysis research

- **Experimental approach**:

  The experiment is initiated by acquiring various AMB substrate patterns and thicknesses from different suppliers and characterizing the copper material properties for further accurate simulation evaluations. To proceed with the manufacturing process, die sintering and annealing thermal treatments are adapted to examine warpage, measured by laser confocal microscope, tendencies under varying conditions.

- **Simulation approach**: Simultaneously, the simulation approach starts from COMSOL finite element models that replicate substrate deformation during manufacturing, utilizing the material properties. It enables the analysis of simulation results to understand warpage behavior, pinpoint potential factors, and investigate warpage tendencies under different conditions.

- **Optimization approach**:

  The optimization integrates findings and validating from experimental and simulation analyses to build up influence factors analysis. Response surface methodology (RSM) analytic method is

applied to identify the most significant pattern influences on warpage. Based on the influence factor, substrate structure redesign using subtractive and additive technology, such as computer numerical control (CNC) milling technique and 3D metal printing, are implemented to achieve the warpage reduction goal in simulation and experiment.

1.4. Outline

The thesis outline is as follows:

Chapter 2 overviews the warpage reduction strategies and discusses sintering and additive technologies. Chapter 3 includes the critical material properties extraction and the further 2D warpage deformation simulation to reveal the physics theory behind warpage. Chapter 4 compares the 3D simulation and the experiment result after the annealing process and analyzes the main factors affecting warpage. Chapter 5 demonstrates the AMB warpage influence by additive and subtractive approaches. Chapter 6 shows the warpage behavior on the AMB with a sintered die-attach layer. Chapter 7 contains the summary and recommendation of the project.

2

Literature Overview

2.1. Introduction

This chapter provides an overview of various warpage reduction strategies based on finite element simulations and experimental results. Additionally, the chapter delves into the manufacturing processes of substrates and die attachment, focusing on the most commonly used substrate materials in the power electronics packaging industry. The chapter also explores the potential of 3D printing technology in the power electronics packaging manufacturing process.

2.2. Ceramic substrate in power package

Printed circuit boards (PCBs) have been a widely used physical support and electrical transmission medium for connecting electronic components due to their high-density interconnect and low inductance in electronic devices[6]. However, the demand for high current and voltage requirements has emerged for the operation of power modules in automobiles such as electric vehicles (EV) and hybrid electric vehicles (HEV)[7]. As a practical solution, ceramic substrates have been introduced with superior thermal conductivity properties compared to PCBs [8]. The utilization of ceramic substrates in power module devices is motivated by their ability to withstand high temperatures, possess high mechanical strength, and offer high electrical isolation. Among the various ceramic substrate materials, aluminum oxide (Al_2O_3), aluminum nitride (AlN), and silicon nitride (Si_3N_4) are the most popular ones [9]. The material properties of ceramic substrate are presented in Table 2.1. While AlN exhibits higher thermal conductivity than Al_2O_3, Al_2O_3 displays a lower CTE mismatch with copper material ($\alpha = 16.3$ ppm/°C) in comparison to AlN [10]. Furthermore, Si_3N_4 offers high mechanical strength and better reliability behavior even after undergoing several thermal cycles, making it one of the most popular materials for power module applications [1].

Table 2.1: Material properties of ceramic substrate

Material Properties	AlN	Al_2O_3	Si_3N_4
Thermal conductivity [W/mK]	170	24	90
CTE [ppm/°C]	4.3	4.5	3.2

2.2.1. AMB and DBC substrate comparison

Direct bonded copper (DBC) and active metal brazing (AMB) ceramic substrates are prevalent in substrate manufacturing [11]. In the manufacturing process of DBC substrates, the copper layer and ceramic are heated to their eutectic melting temperature (1065°C), creating a solid connection between the ceramic and copper layer during the cooling process, as Fig.2.1 shows [12]. On the other hand, AMB substrates use an active metal layer consisting of Ag, Ti, and Cu to produce a metallurgical combination layer between the ceramic and copper layer [13]. The active metal layer of the AMB substrate generates a more potent bonding force and decreases thermal stress, resulting in higher reliability than the DBC substrate [14]. However, the significant differences in the CTE value between the copper and ceramic layer in AMB substrates cause massive warpage with residual stress during process temperature changes in the process [15]. Warpage adversely affects the connection between the substrate and chips or heatsink, reducing the thermal dissipation rate. It also subjects the substrates to excessive internal stress, leading to cracks and fractures, ultimately impacting the production line and quality [4]. As a result, reducing warpage is a critical research topic in the AMB substrate process.

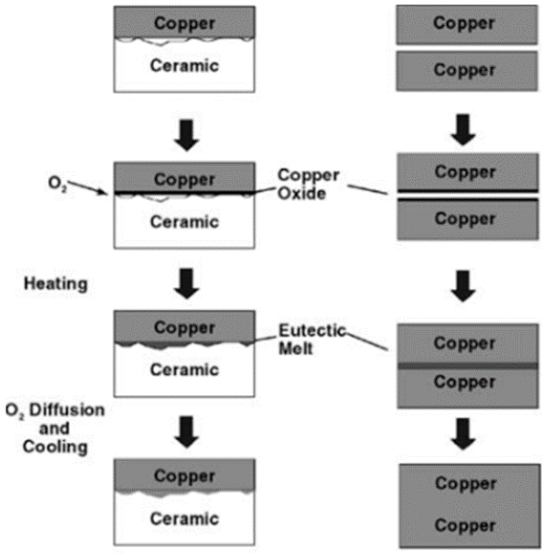

Figure 2.1: Manufacturing process of DBC Substrate[16]

2.2.2. Influence factors for ceramic substrate warpage

In M.Y. Tsai, et al. research, the effect of the thickness and length of a single-sided copper layer on the warpage is investigated. The study finds the thickness of the copper layer is positively correlated

with warpage, shown in Fig.2.2. The thicker copper layer results in larger warpage. Furthermore, the length of the copper layer also impacts the warpage, with longer copper layers resulting in increased warpage [10].

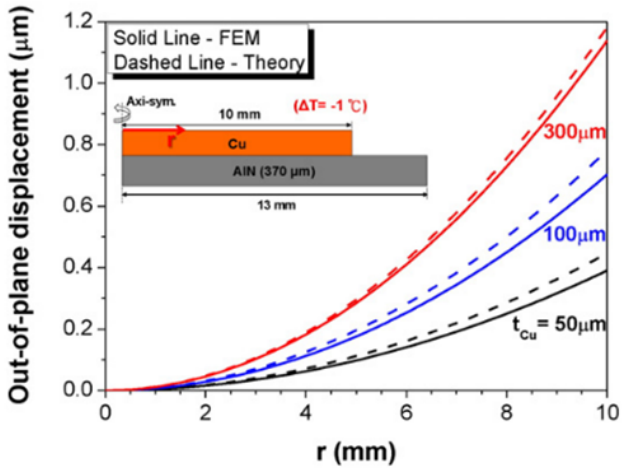

Figure 2.2: The relationship between displacement and the copper layer dimension

Emmanuel Arriola, et al. demonstrate the impact of adding a channel near the edge of the copper layer on the warpage of a substrate. The schematic is shown in Fig. 2.3. The research employs finite element analysis software to analyze the substrate warpage and its sensitivity to the channel size. The results indicate that adding a channel can lead to a substantial reduction in warpage to 48%. Moreover, wider channels have a pronounced influence on reducing the warpage compared to the narrow channels [17].

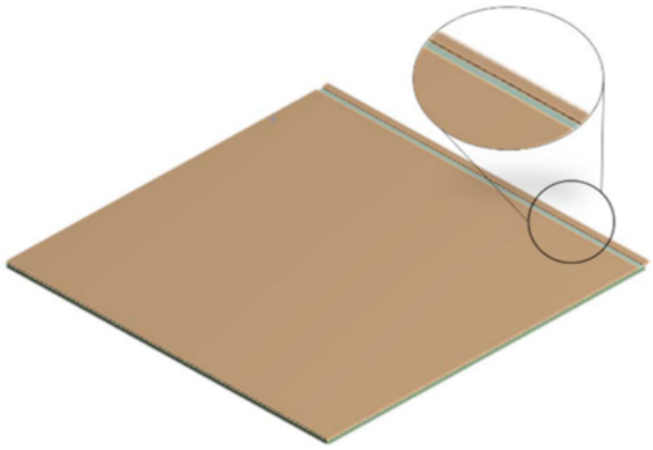

Figure 2.3: Schematic of a channel on the substrate

In [18], it proposes a capped-die flip chip package, shown in Fig 2.4 as a solution to reduce the warpage and stress during the underfill curing process. It is well-known that a significant amount of warpage occurs during the underfill curing, which results in a solid mechanical connection between the substrate and chip due to the CTE mismatch. To address the issue, the author designed a metal cap

that covers the die and dispenses an adhesive material with a similar glass transition temperature (Tg) into the gap between the cap and the die. The concurrent curing of the underfill and adhesive material, along with the thickness of the cap, can introduce an effective CTE to the capped die resulting in a better balance with the substrate. Based on the experimental results, the warpage can be reduced by up to 75% by adjusting the thickness and material of the cap.

Figure 2.4: Schematic of a capped-die flip chip package

Ling Xu, et al. investigate a ladder-shaped copper layer, shown in 2.5, using elastic and plastic material properties of copper. The study focused on the effect of copper layer thickness and the ladder shape on the number of thermal cycles, plastic deformation, and warpage. The results show that the thickness of the copper layer affects the von Mises stress distribution, with an increase in h1 causing the maximum von Mises stress to move from the second copper layer to the first. The width of the ladder tail, w2, was found to dominate the plastic distortion of the whole substrate, with larger values causing greater distortion. On the other hand, adjusting the value of w1 had a greater influence on warpage. A trade-off between the thickness and ladder tail changes was identified as affecting the warpage and plastic distortion. The findings of this study provide valuable insights for optimizing the design of ladder-shaped copper layers to improve the performance of electronic devices [19].

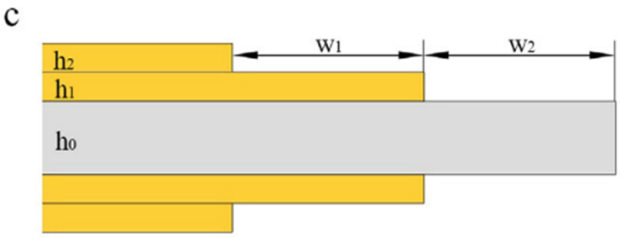

Figure 2.5: Schematic of ladder shape on the substrate

In [20], a double-sided substrate is employed to present the effects of using a clamp during the sintering process and the thickness of the backside copper layer on the warpage. The study found that using a clamp during the sintering process resulted in a warpage increase of only 2.5 times compared to that without clamping, which is three times larger. Furthermore, reducing the thickness of the backside copper layer was shown to reduce the warpage of the substrate panel by up to 55% after the sintering process.

2.3. Die attachment in microelectronics

Die attachment refers to creating a strong mechanical connection between the die and substrate to facilitate the transfer of electrical signals and heat dissipation in and out of the chip, as Fig.2.6 shows [21].

With the emergence of wide-bandgap (WBG) in semiconductors like silicon carbide (SiC) and gallium nitride (GaN) in power device development, it has become increasingly crucial to use die attachment materials that can withstand high-temperature operating environments exceeding 250°C, given the high voltage and power density performances of these materials [22]. In the industry, soldering and sintering are the two main die-attachment technologies for high-temperature devices [23].

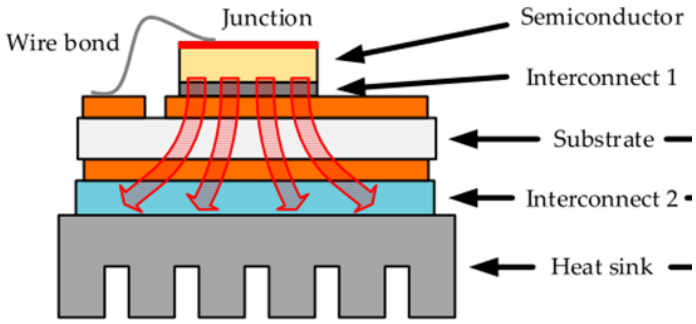

Figure 2.6: Heat dissipation path in power module [24]

The soldering process involves placing the solder material onto the die and substrate and creating a metallurgical interconnection between the two components. During the soldering process, several steps occur, including the placement of the solder material, it is melting onto the surface of the die and substrate, the occurrence of interfacial reactions, and the solidification of the solder material during the cooling session. Typically, high-lead solder materials achieve higher melting points and ensure a reliable connection, as Fig.2.7 shows [25]. However, due to environmental concerns and regulations such as the Restriction of Hazardous Substances (RoHS), the use of lead in soldering is promulgated. It is the responsibility to use alternative materials to pursue a more sustainable environment [26].

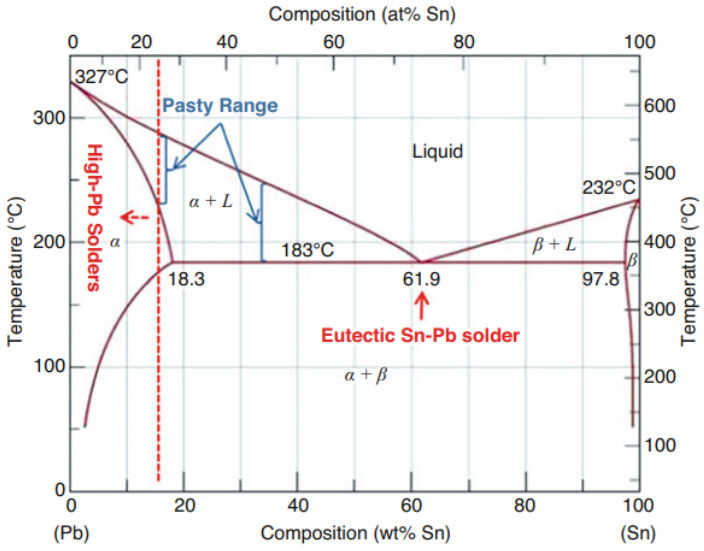

Figure 2.7: Sn-Pb binary phase diagram[25]

Sintering is developed as a more advanced technology of die attachment due to its superior reliability

and thermal conductivity compared to soldering technology [27]. Unlike soldering, sintering involves using a solid-state material composed of specific diameter particles bonded to the die and substrate through the application of heat and pressure without reaching the melting point. The sintering process typically involves several steps, including stencil printing, heating on a plate, and applying pressure to the die, shown in Fig. 2.8. As depicted in Fig.2.9, the state of the silver sintering paste changes during the process, ultimately resulting in a solid bond between the die and substrate [28].

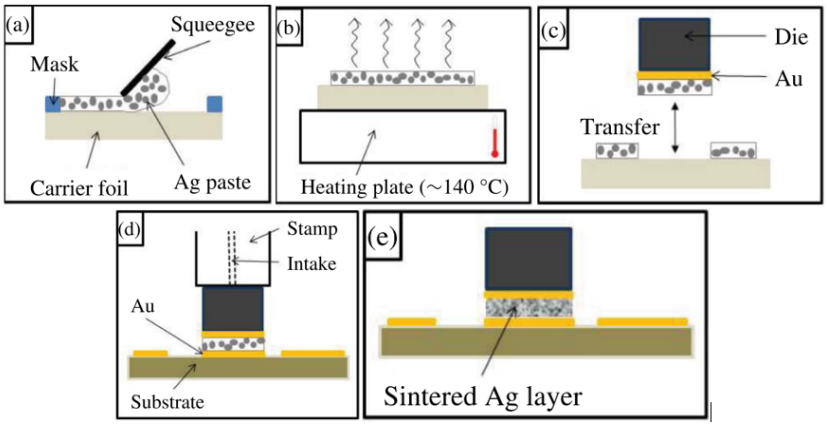

Figure 2.8: Manufacturing process of sintering[28]

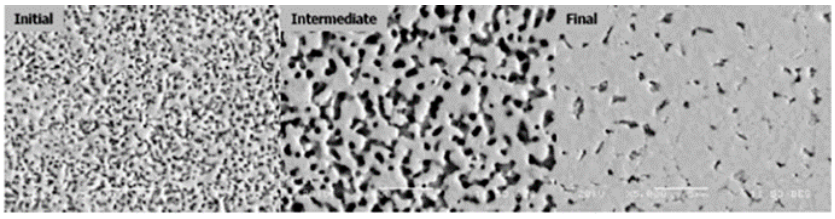

Figure 2.9: States change of silver sintering paste crosssection[25]

In Xiao et al. research, lead-free solder and nano-silver die attachment technology was compared to analyze their performance in thermal impedance, degradation, and shear strength [29]. The results showed that the sintering layer outperformed the solder layer in terms of thermal impedance, with the solder samples having 12% higher impedance than the sintering. Furthermore, the sintering layer had less degradation after 500 thermal cycles, whereas the soldering layer showed a degradation of 13%. For the thermal impedance, the solders samples have 12% higher than the sintering. The sintering also has less degradation after 500 thermally cycles compared with 13% of the soldering layer. Additionally, Dongjin Kim et al. present a study that demonstrated a significant decrease in the shear strength of the soldering layer (by 60%). In contrast, the sintering layer remained stable and sustained throughout the experiment. These findings suggest that sintering technology could be a better option for die attachment in high-temperature applications. Compared to soldering technology, it offers improved reliability, thermal conductivity, and shear strength.

2.4. 3D printing in manufacturing process

Figure 2.6 illustrates the interconnection of various layers within the device structure using interconnect paste for attachment. Nonetheless, this approach imposes constraints on heat dissipation efficiency and signal transmission speed and increases the CTE mismatch within the device layers. Consequently, the exploration of 3D metal printing is undertaken to enhance heat dissipation capabilities and mitigate the challenges posed by CTE mismatch. 3D metal printing is an additive manufacturing technique that offers greater manufacturing flexibility, production speed, and design complexity than traditional mass production methods allowing for the creation of intricate 3D structures [30]. Two standard methods of 3D metal printing are Binder Jetting (BJ) and Selective Laser Melting (SLM). In the Binder Jetting process, a binder droplet creates a solid connection of the copper powder, as shown in Fig.2.10 [31].

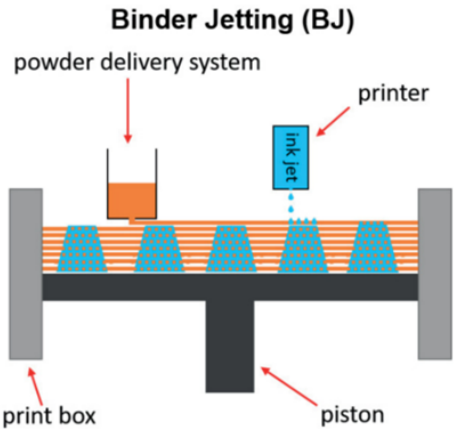

Figure 2.10: Schematic of binder jetting technology

Although the Binder Jetting process offers advantages such as high accuracy and productivity, some concerns arise due to the fact that the powder used needs to reach its melting point during the process. As a result, porosity and curing in future processes are the main issues that need to be addressed [32]. SLM method involves placing a thin powder bed and then using a laser beam to melt the powder fully, creating strong connections between layers and repeating the process until the final structure is formed, shown in Fig.2.11 [33]. The accuracy and solidity of the structure depend on controlling the laser speed, power, and hatch distance. Despite the slower printing speed compared to binder jetting and the use of a high-power laser, SLM is one of the most popular 3D printing methods due to its high resolution and more solid structure [32].

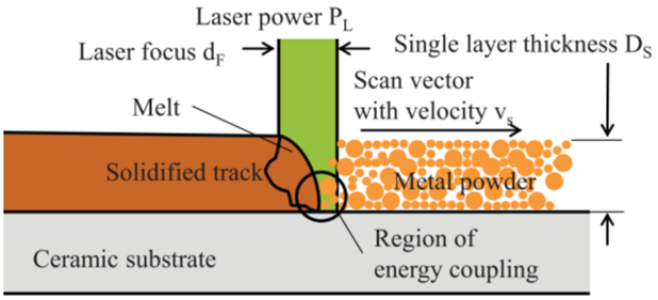

Figure 2.11: Schematic of selective laser melting technology

2.5. Chapter summary

This chapter provides a comprehensive discussion on various topics related to the manufacturing process of DBC and AMB substrates. It starts from the ceramic substrate material properties comparison to the substrate manufacturing step difference, then deep into warpage influence by manufacturing factors influence to analyze warpage reduction. Next, the die attachment techniques and the additive manufacturing technique are also discussed. Moreover, the chapter discusses the potential of additive manufacturing in packaging processes. However, limited research exists on the detailed reasons for warpage generation and simulation validation through experiments. In this project, we aim to explain the physics theory behind warpage generation and analyze the impact of additive and subtractive manufacturing on warpage.

3

Fundamentals of AMB Substrate Warpage

3.1. Chapter introduction

The chapter provides an overview of the AMB substrate manufacturing process and investigates the warpage deformation phenomenon. It covers the material properties measurement of copper, the detailed steps of the manufacturing process, and the boundary conditions used for analysis. The chapter aims to identify and explain the causes of warpage by applying a FEM model accompanied by mechanics of material theory interpretation. The study offers insights into the underlying mechanisms of warpage deformation by quantifying factors such as elastic, plastic, and thermal strains.

3.2. Manufacturing process flow of AMB substrate

The process flow outlined, shown in Fig.3.1, describes AMB substrates' fabrication process, beginning with brazing and continuing through the pattern etching process to the final annealing step. However, the AMB substrate experienced significant warpage changes and different curvature directions between each step during the process. The AMB substrate comprises three layers from top to bottom: copper, ceramic, and copper. In the first step, these three layers are joined by brazing at 800 °C, the reference temperature for the entire fabrication process. Secondly, it cools down to room temperature with a moderate cooling rate. Due to the symmetry structure, there is negligible warpage generated. Thirdly, the pattern on the front side copper layer is created using the etching process at room temperature. However, due to the unbalanced internal stress, it introduces the convex initial warpage in this step. Fourthly, to mimic the sintering process, the substrate undergoes an extra annealing process, heating up to 280 °C. At this temperature, the substrate is observed to have a concave shape. The final step cools down the substrate to room temperature again. The final warpage is roughly 4.5 times larger than the convex initial warpage.

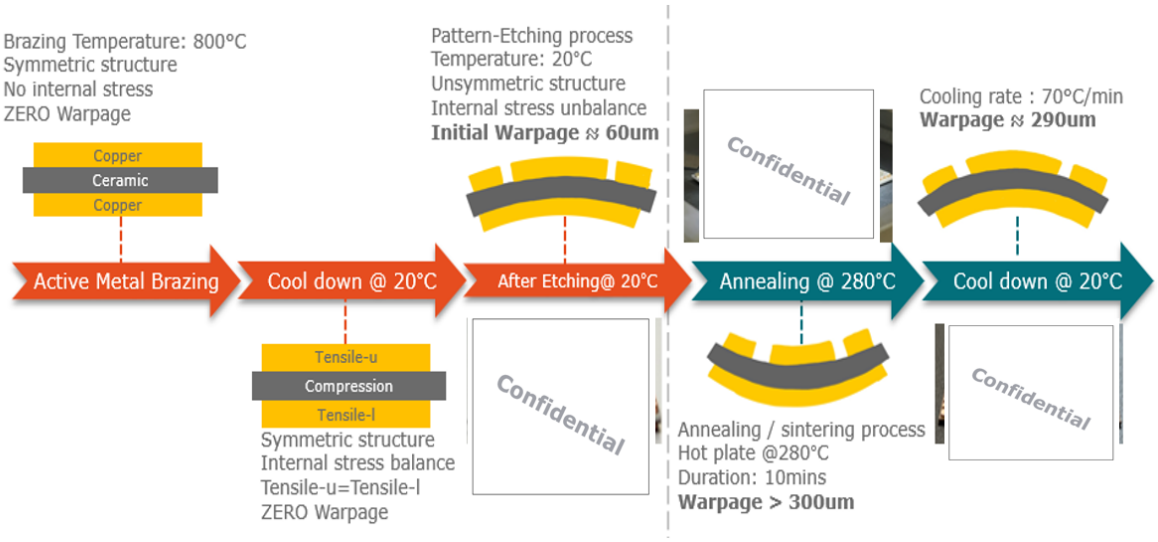

Figure 3.1: Manufacturing process flow of AMB substrate

3.3. Material properties measurement experiment

The material properties of copper play an essential role in finite element simulation. To obtain the proper copper material properties, the experiment of thermal expansion coefficient (CTE) measurement, tensile test, and nanoindentation experiment to collect the data for CTE, Young's modulus, yield stress, tangent modulus, and hardness proceeded.

3.3.1. Thermal expansion coefficient (CTE)

The CTE quantifies the variation in volume, size, or length due to fluctuations in temperature. It is symbolized by α and expressed in units per degree Celsius (1/°C). This coefficient signifies the proportionate change in length or volume to each degree Celsius of temperature change. Determining CTE data involves utilizing thermomechanical analysis (TMA) equipment, which measures the variations in material length as a function of temperature. Specifically, the employed TMA instrument is the Mettler Toledo TMA SDTA2+, depicted in Figure 3.2.

Figure 3.2: Picture of Mettler Toledo TMA SDTA2+ equipment

The experiment started with sample preparation, sample mounting, temperature program setting, and data acquisition and ended up with CTE calculation and analysis. To conform to the sample size requirement, a 0.8 mm thick sample was cut into 8 mm $\times$ 4 mm dimensions, as illustrated in Figure 3.3a. The sample was affixed to a quartz tube, enabling the detection of copper thickness variations, as depicted in Figure 3.3b. The temperature profile initiated at 25 °C, representing room temperature, increased to 365 °C at a rate of 5 °C/min, maintained a steady temperature for 10 minutes, and subsequently cooled to 25 °C at the same rate. Throughout this process, a nitrogen chamber environment was maintained to avert oxidation. Figure 3.3c illustrates the temperature settings for this thermal cycle.

Figure 3.4 displays the data extracted from the cooling phase spanning 365 °C to 25 °C, depicting the variation in copper thickness length. The CTE (α) was computed using the equation:

$$\alpha = \frac{\Delta L}{L \times \Delta T}$$

The calculated average CTE was determined to be 16.7 $\times$ 10^{-6} [K^{-1}].

Observations indicate inevitable fluctuations within the recorded data, potentially influenced by factors such as non-steady cooling temperatures, differences between the sample temperature and thermocouple measurements, and environmental vibrations that might impact length measurements.

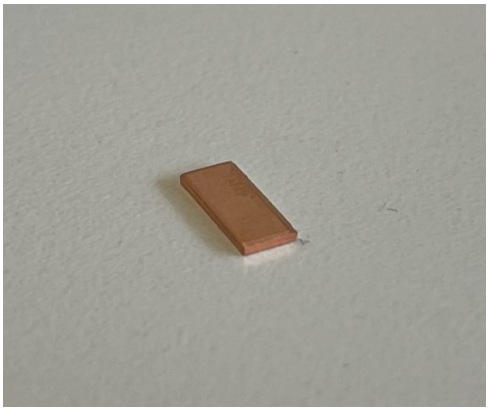

(a) Copper sample of TMA measurement

(b) Copper sample mounted on TMA equipment

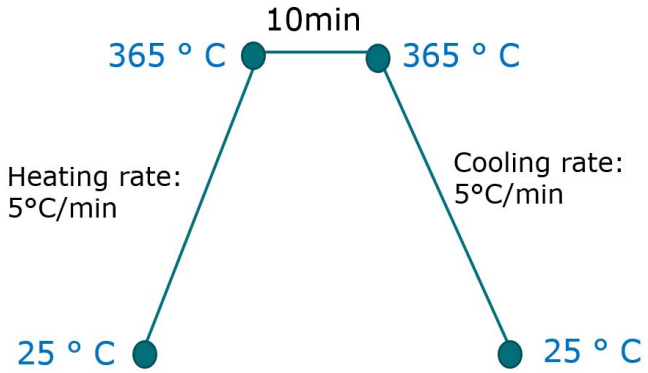

(c) Temperature setting of CTE experiment

Figure 3.3: TMA measurement process

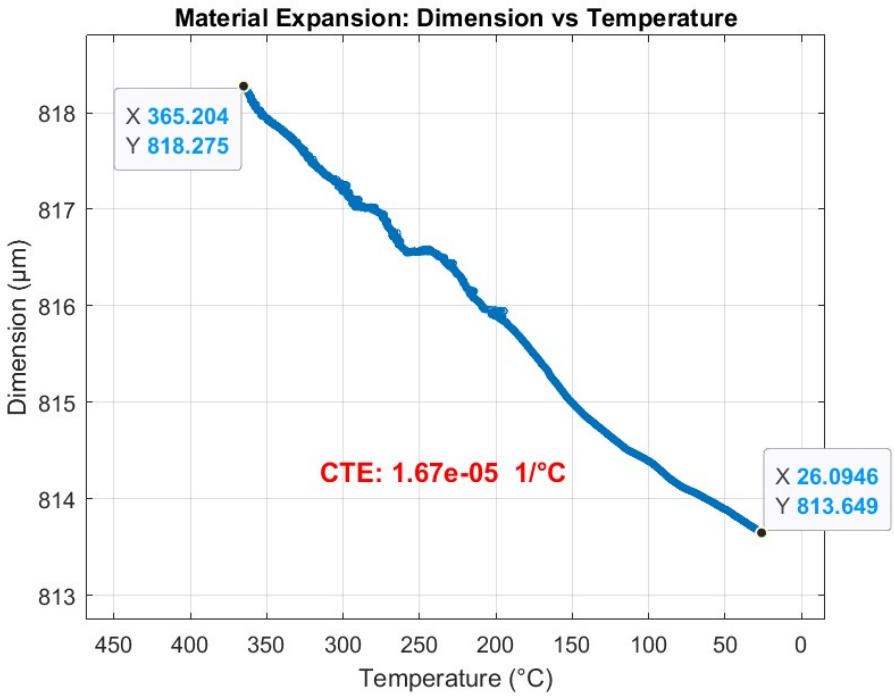

Figure 3.4: CTE measurement result plot: dimension vs. temperature

3.3.2. Tensile test

In order to acquire the material properties of annealed copper, such as Young's modulus, tangent modulus, and yield stress, it is essential to conduct a tensile test. During this test, a dog bone-shaped sample of the copper material is securely clamped between two clamps, and a controlled constant strain speed with axial force is applied until the sample fractures. The variation in sample length and the applied force are carefully recorded throughout the test. By doing the subsequent calculations, essential properties such as ultimate tensile strength, yield strength, elongation, and Young's modulus can be determined. The equipment for the tensile test was the MTS CMT 4304, as depicted in Figure 3.5.

Figure 3.5: Tensile test equipment: MTS CMT 4304

The tensile test was performed on the annealed oxygen-free copper (OFC) subjected to annealing at a temperature of 800°C. Figure 3.6 compares the original OFC and the annealed OFC, where the left side represents the original OFC, and the right side depicts the annealed OFC. A noticeable observation is the significantly larger grain size of the annealed OFC compared to the original OFC. The grain size measurement and calculation details will be discussed in section 4.2.

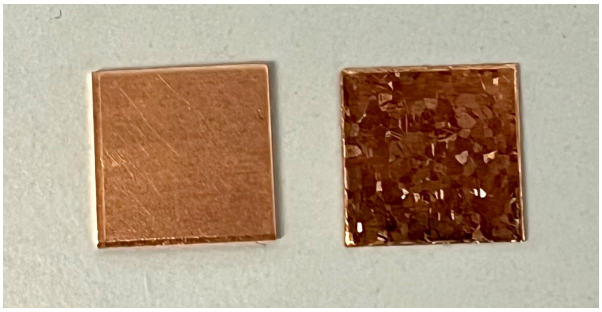

Figure 3.6: Pictue of original and annealed OFC

The experimental investigation involved evaluating the mechanical behavior of the samples at various environmental temperatures, starting from 20 °C, 95 °C, 170 °C, and up to 250 °C. The strain rate was set at 0.1 [1/s]. The dimensions of the specimens were 15 mm × 59 mm × 0.8 mm, and the effective dimension was 5 mm × 39 mm × 0.8 mm. Figure 3.7a represents a schematic diagram illustrating the dimensions of the copper dog bone specimen. Figure 3.7b demonstrates the crosshead arrangement used to hold the sample in place during the test. The displacement between two crossheads was measured and considered as the elongation of the specimens. Throughout the measurement, the specimens experienced a tensile force from their initial shape to the fracture point, undergoing both elastic and plastic hardening deformation. Figure 3.7c displays the deformed copper specimen following the completion of the tensile testing.

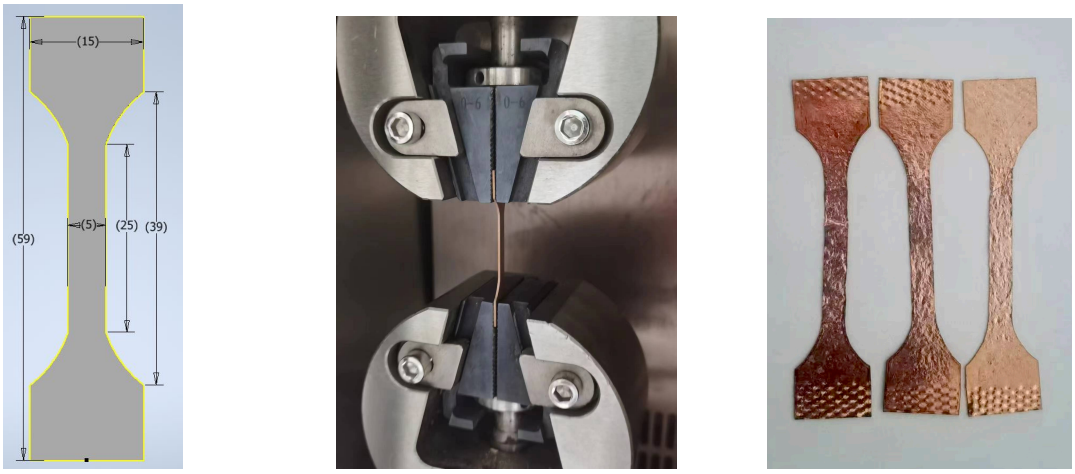

(a) Copper dog bone specimen schematic of tensile test

(b) Copper specimen mounted on tensile test equipment

(c) Deformed copper specimen after Tensile Testing

Figure 3.7: Tensile test experiment specimen and process picture

For the measurement result of the annealed OFC, Figure 3.8 illustrates the stress-strain curve of

annealed copper at four different temperatures. The overview of the stress-strain curve is presented in Figure 3.8a, and Figure 3.8b shows a detailed view of the elastic deformation and the initial stages of plastic deformation. Young's modulus was extracted by the slope of the first linear part of the stress-strain curve. Yield stress was calculated as the stress value corresponding to the 0.2% plastic strain. The tangent modulus was the slope of the stress-strain curve after the yield stress point and before the ultimate tensile stress point.

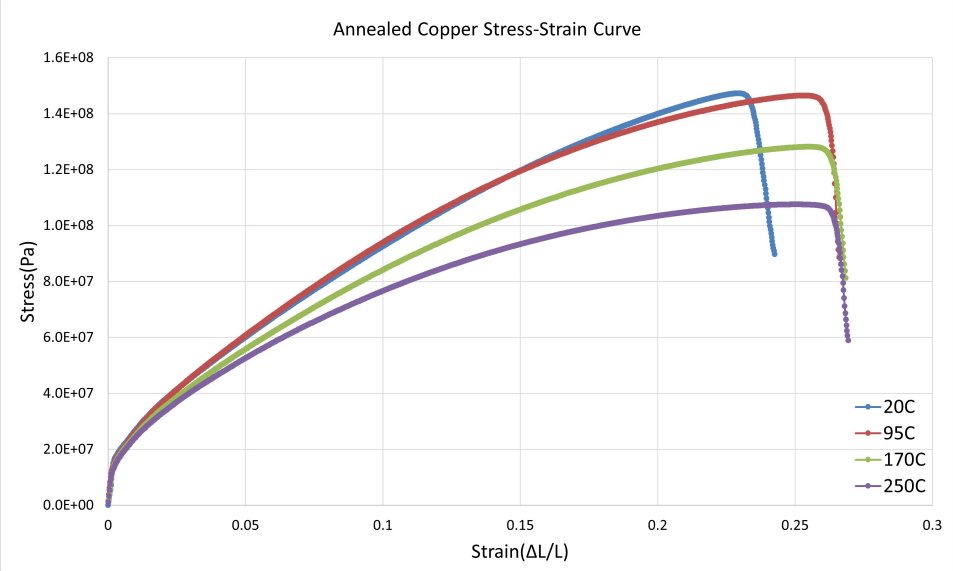

(a) Annealed OFC tensile test stress-strain curve

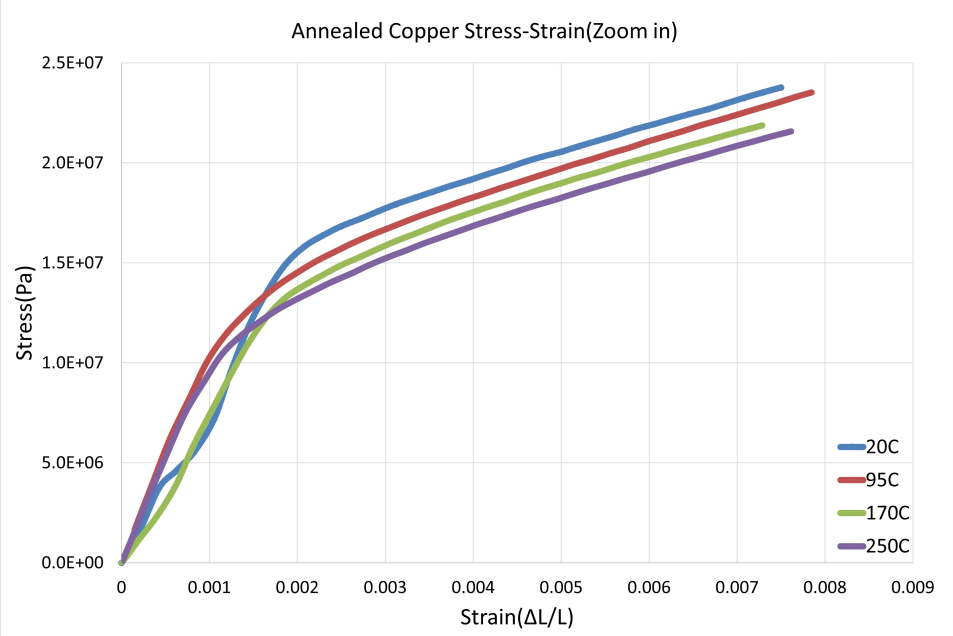

(b) Zooming in on the stress-strain curve of annealed OFC tensile test

Figure 3.8: Annealed OFC stress-strain plot

Table 3.1 provides the material properties of annealed OFC, including Young's modulus and yield

stress values at temperatures ranging from 20 °C to 250 °C. For Young's modulus, the measurements indicate values of 10.5 GPa, 10.2 GPa, 9.1 GPa, and 10.4 GPa for temperatures of 20 °C, 95 °C, 170 °C, and 250 °C, respectively. Notably, there is no significant variation in Young's modulus concerning the temperature difference. However, the yield stress values show a decreasing trend with increasing environmental temperatures, measuring 18.8 MPa, 17.5 MPa, 17.3 MPa, and 16.3 MPa for temperatures from 20 °C to 250 °C.

Table 3.1: Tensile test result of annealed OFC

Temperature	Young's modulus(GPa)	Yield stress (MPa)	Tangent modulus(MPa)
20 °C	10.5	18.8	674.4
95 °C	10.2	17.5	684.6
170 °C	9.1	17.3	591.7
250 °C	10.4	16.3	507.7

Table 3.2 provides the reference Young's modulus values for annealed copper, which are 8 to 9 times greater than the measured results. The discrepancy arises due to the experimental setup where the movement of the cross-head is measured as a displacement. This measurement includes the displacement of both the specimen and the machine [34]. Figure 3.9 illustrates the cross-head displacement measurement, which considers factors like the slippage of the gripper, clamping deficiencies, and the movement of the cross-head, thus influencing the measurement of Young's modulus, which is affected by the copper specimen and the loading equipment [35]. Notably, in the research conducted by Zhu et al., it was discovered that for grain sizes larger than 50 nm, Young's modulus value remains relatively constant. However, considering the uncertain results of Young's modulus from the experiment, the subsequent simulation will utilize the reference Young's modulus value for the analysis [36].

Table 3.2: Reference young's modulus of copper [37]

Temperature (°C)	20	50	150	250
Young's modulus (GPa)	96.89	92.1	89.6	79.8

Unlike Young's modulus, the yield stress value shows less significant influence from the displacement measurement. Figure 3.10 depicts the schematic of stress-strain curvature measured by both the extensometer and cross-head. In the research conducted by H.B. Motra et al., they found that the tensile strength measured by cross-head motion does not exhibit significant differences compared to the extensometer measurements [38].

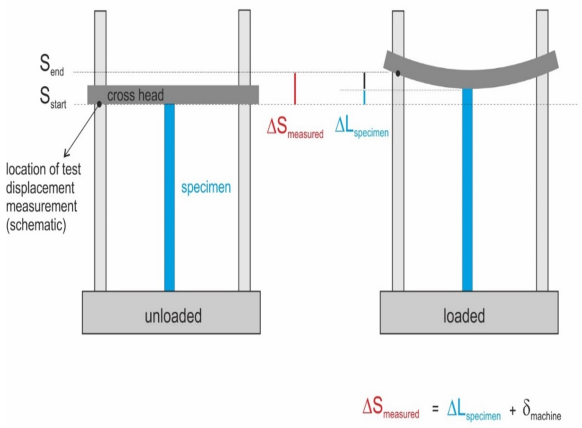

Figure 3.9: Schematic of the displacement measurement

The yield stress value can be referred to as the 0.2 % offset yield strength. This refers to the stress value at which the material experiences a permanent strain equal to 0.2% of its original length. To calculate the 0.2% offset yield strength, a parallel line is drawn from the linear slope of Young's modulus and offset by 0.002 strain. This line is then used to intersect with the stress-strain curve to obtain the yield stress value. The 0.2% strain occurs when the external tensile force is zero, and the plastic deformation happens within the specimen itself. The yield stress is mostly independent of equipment variables, gripping effects, and measurement errors [39]. Consequently, while the displacement measurement may significantly influence Young's modulus, the yield stress remains relatively unaffected by these factors.

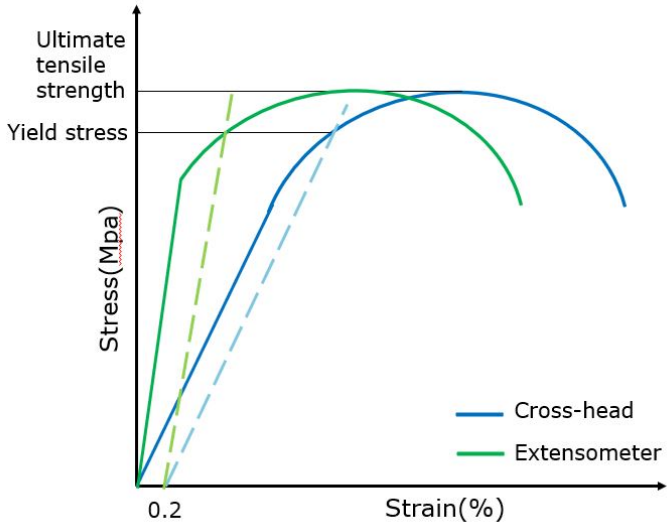

Figure 3.10: Schematic of stress-strain curvature measured by extensometer and cross-Head

The tangent modulus describes the relationship between stress and strain in the plastic deformation region. During the tensile test, the elastic deformation covers 0.2 % of the strain, while the plastic deformation spanned approximately 25% of the strain. It is reasonable to assume that the slippage occurring during the displacement measurement has minimal impact on the plastic regime. Hence, the

tangent modulus could be calculated from the stress-strain curve, as depicted in Figure 3.8a. To perform the calculation, we started from the 0.2 % yield point and proceeded to 0.14 strain, as the strain generated during the manufacturing process did not exceed 0.12. Therefore, a linear trendline was drawn between this strain region, and the slope of this linear trendline determined the tangent modulus.

3.4. FEM model of 2D AMB substrate

The internal stress and strain distribution that explains the deformation of the substrate during the manufacturing process from a thermo-mechanical view. To investigate, the finite element simulation was conducted to reproduce and explain the phenomenon. FEM is a widely used numerical method that solves problems using partial differential equations. In FEM, the structure was segmented into small pieces and solved with boundary conditions and parameter values to find the numerical solution. COMSOL software, one of the most popular FEM software packages, was used in the project to simulate and analyze the results, providing further evidence to support the observed warpage and deformation. A solid mechanics approach in physics was employed in the COMSOL to investigate the warpage and mechanical properties of AMB substrate. The 2D model was chosen to save the computation resources and make it easier to observe and analyze the deformation. The designed AMB 2D structure is depicted in Fig.3.11, where copper is used for the top and bottom layers, while the middle layer consists of a silicon nitride (Si_3N_4) material. On the top layer, the blue area indicates the trench parts that are etched during manufacturing.

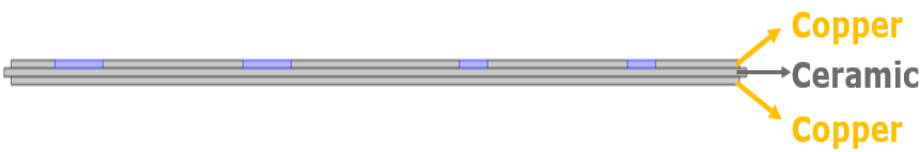

Figure 3.11: 2D structure of AMB substrate simulation

In the model, the ceramic layer, which is Si_3N_4, was assumed to be isotropic elastic material with known Young's modulus (E), Poisson's ratio (ν), and CTE as provided in Table3.3. However, the model did not consider the temperature dependence of Si_3N_4 material properties. On the other hand, the material properties of copper were highly dependent on temperature. Table 3.4 shows details of copper material properties, including the Thermal Expansion Coefficient (CTE), Young's modulus (E), Poisson's ratio (ν), yield stress, and tangent modulus. The yield stress and tangent modulus are used to describe the plastic deformation of copper during the simulation.

Table 3.3: Material properties of Si_3N_4[15]

Material	Si_3N_4
Young's modulus (GPa)	300
Poisson's ratio	0.28
CTE (K^{-1})	2.6×10^{-6}

Table 3.4: Material properties of copper in simulation model [37]

Temperature (°C)	20	50	150	250	500	800
Young's modulus (GPa)	96.89	92.1	89.6	79.8	64	58
Poisson's ratio	0.34					
CTE (K^{-1})	16.7×10^{-6}					

Table 3.5: Yield stress and tangent modulus of copper in simulation model

Temperature (°C)	20	95	170	250
Yield stress (MPa)	18.8	17.5	17.3	16.3
Tangent modulus (MPa)	674.4	684.6	591.7	507.7

Figure 3.12 presents the mesh and boundary settings used in the simulation. Due to the structural discontinuity, the geometry required segmentation into free tetrahedral shapes. The two-point boundary condition was set such that the left-lower corner point had a prescribed zero displacement in both the x and y directions. In contrast, the right-lower corner point only had a prescribed zero displacement in the y direction. These boundary conditions were set to prevent the rotation and slip on the surface and capture the deformation accurately during simulation.

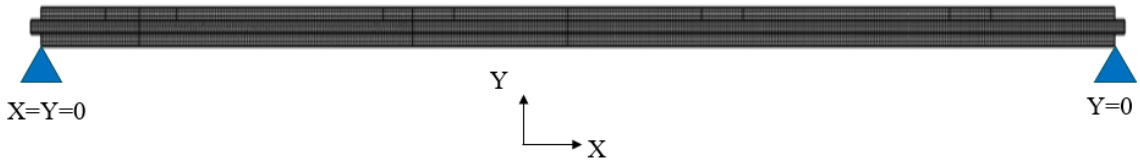

Figure 3.12: FEM mesh and boundary condition of 2D structure

During the simulation process, five steps were taken in the stationary study. These steps followed the manufacturing and annealing process, as mentioned in Fig.3.1. In the first step, the three layers' structure shown in Fig.3.11 was conducted at 800 °C. Next, the simulation environment temperature was cooled to 20 °C. Thirdly, the etching process was simulated using the deactivation function. This function enabled users to selectively disable specific components during certain study steps, allowing investigation into removing particular parts in real-world scenarios. Implementing this function involved modifying the elastic stiffness and density by reducing them to 10^{-5} times their original values. This adjustment was made to simulate the specific behavior of the system under consideration. Fourthly,

the temperature of the simulation environment increased to 280 °C. Lastly, step five cooled the unsymmetrical substrate back to 20 °C. The details of the evolution on the warpage will be explained in the following sections.

3.5. Strain deformation during manufacturing process

During the process, temperature differences occur in each step, resulting in strain variations primarily in the XX direction. The distribution of strain is related to the distribution of stress. The stress, in turn, generates moments on the substrate, leading to warpage. The relationship between stress, moments, and warpage will be discussed in Section 3.6.

The following analysis will be separated into the thermal and mechanical perspectives. The total strain of copper is expressed as:

$$\epsilon = \epsilon_t + \epsilon_e + \epsilon_p$$

, where ϵ, ϵ_t, ϵ_e, and ϵ_p are the total strain, thermal strain, elastic strain, and plastic strain, respectively. Thermal strain refers to the expansion or contraction resulting from temperature changes. Elastic strain is a reversible strain. If the force is removed, the elastic deformation is also disappeared. Plastic strain, on the other hand, is generated when the force applied is greater than the material's yield stress and is irreversible even when the force is removed. In the following explanation,ϵ_e,ϵ_p,and ϵ_t are used to exhibit the strain in XX direction.

A solid ceramic-metal hetero-interface is created during the brazing process in step 1. The three individual layers, which are copper, ceramic, and copper, respectively, are connected at a temperature of 800 °C. At that point, there is no internal stress, and no warpage is generated. In the FEM simulation, the 800 °C brazing temperature is set as the reference temperature. It represents the original condition of the structure without expansion, warping, or shrinking.

Following the brazing process, the substrate is cooled down to 20 °C in step 2. Despite the temperature change, no warpage is introduced because of the symmetric structure of the front and back side copper layers. However, significant internal stress is generated due to the significant differences in thermal expansion coefficients (CTE) between the materials (Cu: $16.7X10^{-6}[\mathrm{K}^{-1}]$, Si_3N_4: $2.6X10^{-6}[\mathrm{K}^{-1}]$), which helps to balance the structure. The thermal strain is calculated as follows:

$$\epsilon_t = \alpha(T - T^{ref})$$

where α is the thermal expansion coefficient and T^{ref})is reference temperature.

From a thermal perspective, the copper and ceramic layers can be treated as separate layers with different CTE, as indicated in Table 3.4 and 3.3. During the cooling phase, the copper layer undergoes more shrinkage than the ceramic layer due to its higher CTE. The shrinkage of the copper and ceramic layers is depicted schematically in Figure 3.13, where the dashed line represents the original size of the material, and the solid line represents the size after cooling.

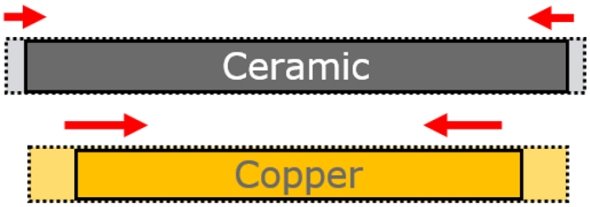

Figure 3.13: Schematic of copper and ceramic layer thermal behavior in cooling session

However, from a mechanical point of view, the fused parts generated in the brazing step are strongly connected. Specifically, points A and A', as well as points B and B' in Figure 3.14, are bonded to each other and not able to move relatively.

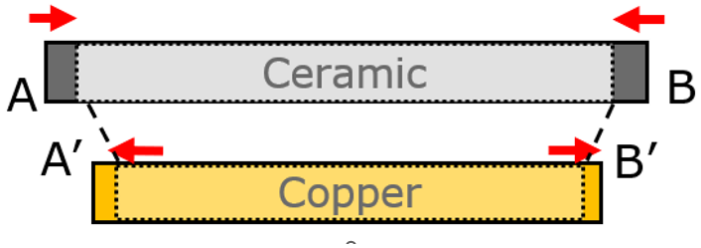

Figure 3.14: Schematic of copper and ceramic layer mechanical behavior in cooling session

As a result, to balance out the thermal and mechanical effects, the copper layers are subjected to tensile forces while the ceramic layer is subjected to compression forces. The balanced forces across the top copper and ceramic parts and the low copper and ceramic layer parts resulted in a negligible warpage. The stress distribution shown in Figure 3.15 reveals that the average von Mises stress in both copper layers is about 26.2 MPa, while the yield stress of copper, as listed in Table 3.3, is 18.8 MPa. This stress level indicates that the copper layers are in the plastic regime and undergo permanent deformation. The FEM simulation results in Table3.6 show the thermal, elastic, and plastic strain from step 2 to step 5. The row of step 2 in Table3.6 shows the value of plastic strain is 0.01086, and the elastic strain is 0.000269. The plastic strain is 40 times greater than the elastic strain, indicating that the plastic deformation dominates the overall deformation of the structure.

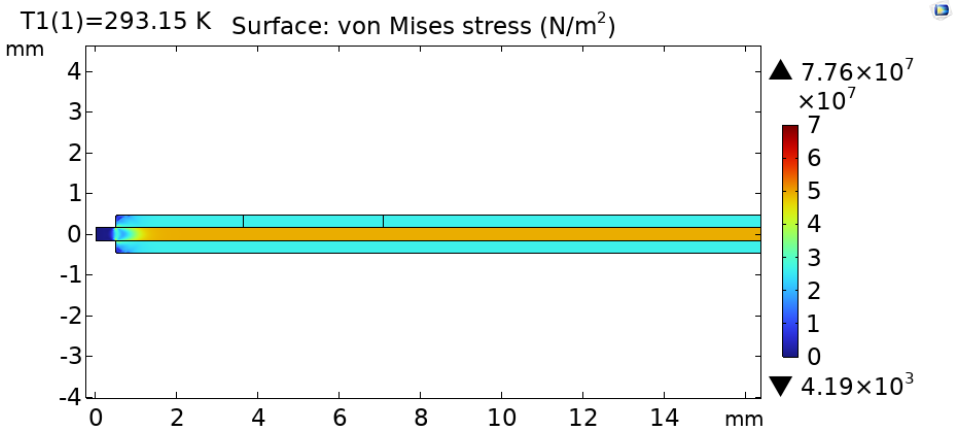

Figure 3.15: Von-Mises stress distribution of the AMB substrate in cooling session

Step 3 transfers the pattern to the copper layer using a chemical etching process at room temperature. The etching is performed exclusively on the front copper layer, partially removing some regions of the front copper layer. In contrast, the back side copper layer retains its original shape without the pattern. The environment temperature stays the same in the simulation setting as in the previous step. The parts being etched out are set in the deactivation function. The deactivation function reduces the specific component's material's elastic stiffness and density to make it disappear.

Consequently, the decrease in stress level distribution due to the etching process can be seen in Figure 3.16. The reduction in stress level is particularly noticeable in the trench areas where the material has been removed. This leads to a disruption in the balance of tensile stress. The stress release also reflects the elastic strain distribution, shown in Figure 3.17. As a result, the initial warpage in a convex shape is generated.

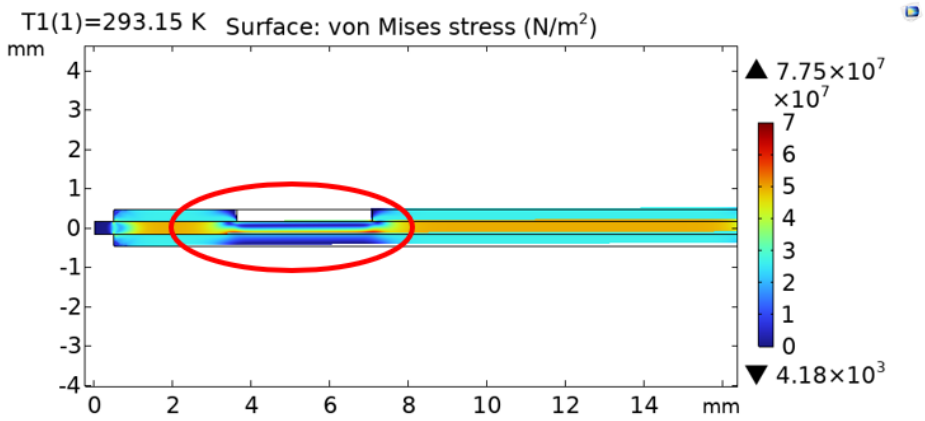

Figure 3.16: Elastic strain distribution of the AMB substrate after the etching process

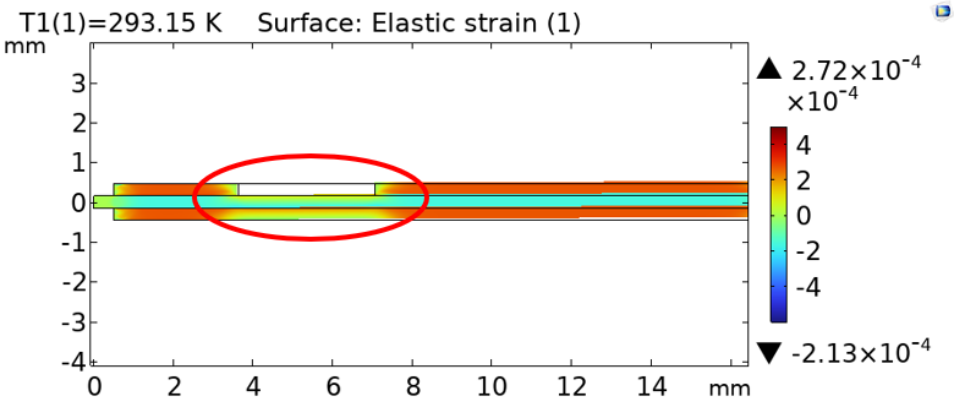

Figure 3.17: Elastic strain distribution of the AMB substrate after the etching process

In step 4, the annealing process occurs where the substrate is subjected to a hot plate at 280 °C for ten minutes. The simulation's environment temperature is also set at 280 °C. The temperature increases result in the expansion of the substrate layer. However, as the volume of copper on the backside is more than on the front side, the expansion force on the bottom is more significant, causing a transformation

in shape from convex to concave. The analysis is divided into thermal and mechanical perspectives to identify the copper deformation as in step 2. From a thermal perspective, the layer expands due to the temperature increase, resulting in a higher thermal strain value than in the previous step. However, the thermal strain value remains negative since the temperature remains lower than the reference temperature defined in the first brazing step. Figure3.18 shows the expansion of the copper and ceramic layers.

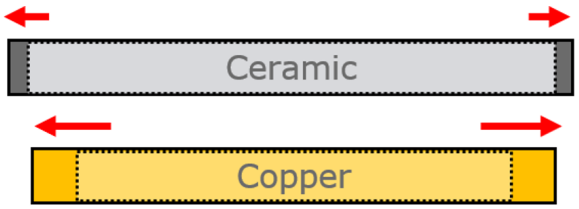

Figure 3.18: Schematic of copper and ceramic layer thermal behavior in annealing session

Due to the CTE mismatch, the copper layer expands more than the ceramic layer. From a mechanical perspective, the stress inside the copper becomes more compressive to prevent the fused part from delaminating, as shown in Figure 3.19. The plastic and elastic strain values are smaller than in step 2. As mentioned before, elastic strain is a reversible strain with the opposite sign compared to the previous step due to the direction of the force. However, the plastic strain reduction is because the compression stress is larger than the yield stress again. Due to the non-reversible characteristic, it only shows a slight reduction instead of the opposite sign as elastic strain shows.

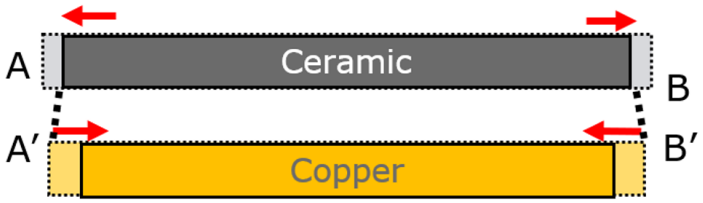

Figure 3.19: Schematic of copper and ceramic layer mechanical behavior in annealing session

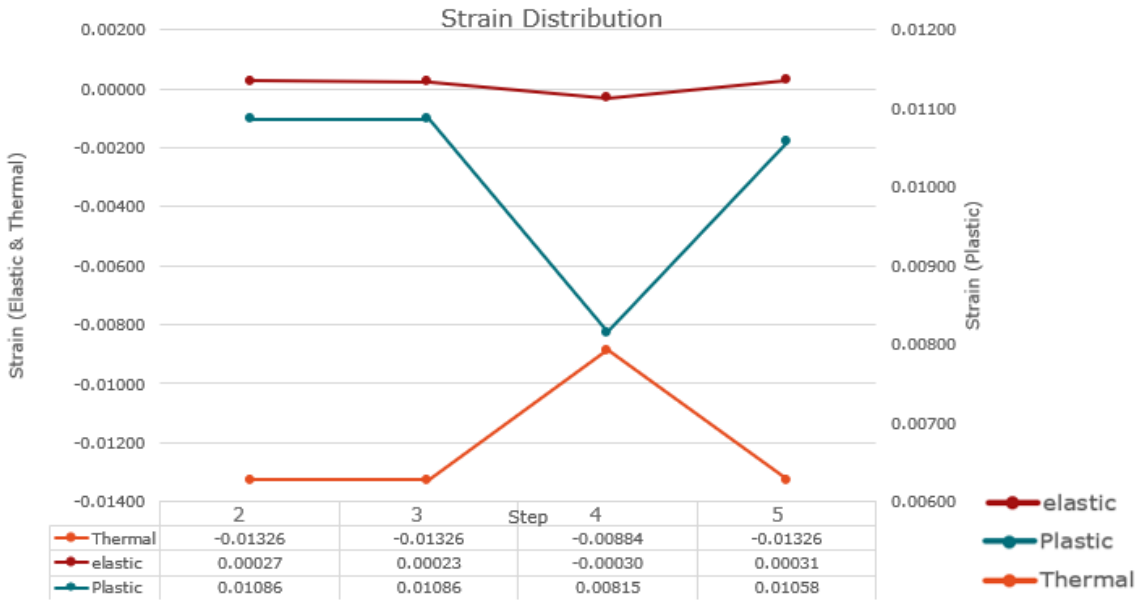

Figure 3.20: Strain distribution of thermal, elastic, and plastic strain in different steps

During the final process, the substrate is cooled from annealing to room temperature. The environment temperature is set as room temperature in the simulation setting. The copper layers tend to shrink more than the ceramic layer due to the CTE mismatch. Moreover, the plastic and elastic strain within the substrate remains to avoid the separation of the connection part. The temperature in this step is the same as in step 3, resulting in the same thermal strain value. However, the non-reversible plastic deformation has already compressed slightly back during the annealing step, and its value cannot return to the same value as in step 3. Table 3.6 shows that the value of the plastic strain increases slightly from the annealing process. However, it does not reach the level observed in the etching process. The elastic strain returns to the positive value due to the mechanical force inside the substrate. Figure 3.20 depicts the elastic, thermal, and plastic strain distribution in a line chart. It can be observed that while the thermal strain remains constant between the first and final steps, there are noticeable changes in the plastic and elastic strain values. The plastic strain exhibits a significant difference of 2.8×10^{-4}, substantially more extensive than the difference in elastic strain of 4×10^{-5}. The previous description discusses the relationship between stress and strain and the irreversible characteristic of plastic deformation. As a result, plastic strain deformation is the leading cause of the permanent shape deformation shape. In the following, the correlation between stress and warpage will be discussed.

Table 3.6: The 2D strain distribution of backside copper layer result from COMSOL simulation

Step	Thermal strain tensor	Plastic strain tensor	Elastic strain tensor
Step 2 Cool @293K	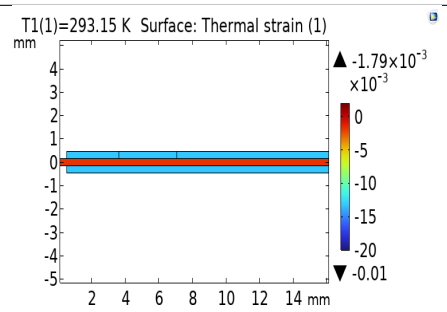 ε_T=-0.01326	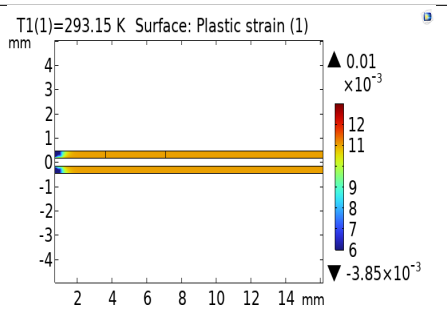 ε_p=0.01086	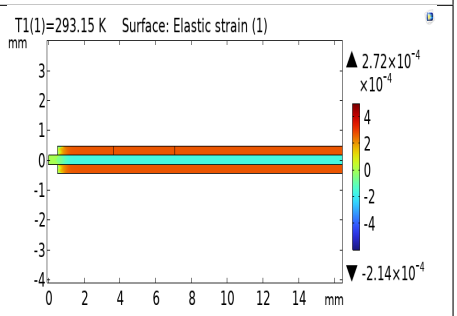 ε_e=0.000269
Step 3 Etch @293K	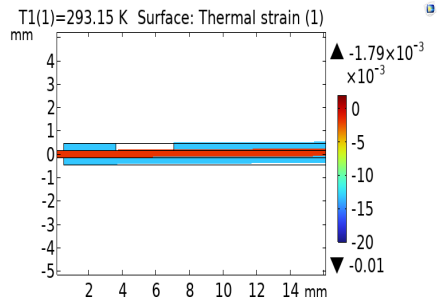 ε_T=-0.01326	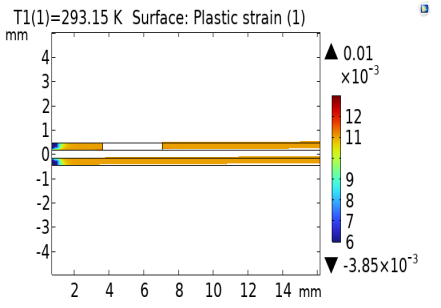 ε_p=0.01086	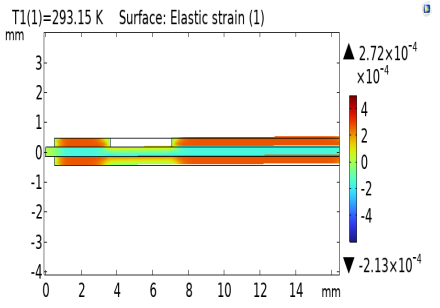 ε_e=0.000226
Step 4 Anneal @553K	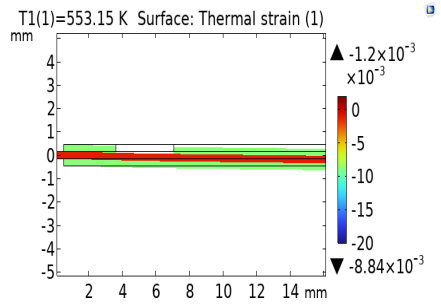 ε_T=-0.00884	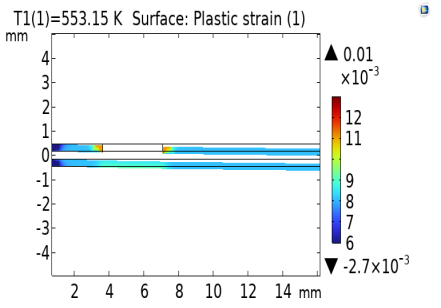 ε_p=0.00815	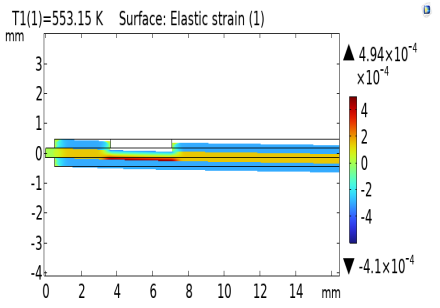 ε_e=-0.000297
Step 5 Cool @293K	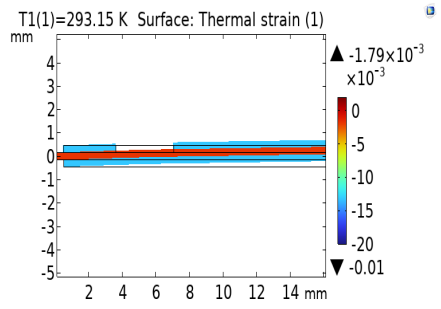 ε_T=-0.01326	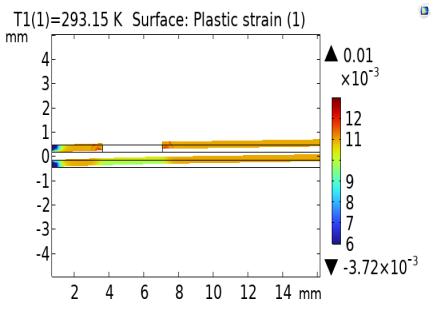 ε_p=0.01058	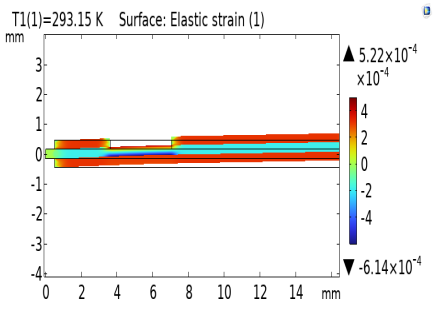 ε_e=0.000305

3.6. Moment variation during manufacturing process

The stress, influenced by the strain distribution, directly affects the moment variation of the warpage deformation. The solid connection between the copper and ceramic layer ensures no delamination

within the substrate. Consequently, the deformation experienced by both layers remains continuous. Additionally, as no external forces are exerted on the substrate, it attains a state of force and moment equilibrium within its structure. The stress distribution throughout the substrate generates moments, ultimately resulting in a warpage. The formula, calculated moment, presents the relationship between moment and force.

$$\tau = r \times F = \frac{d^2v}{dx^2}EI = \frac{1}{\rho}EI$$

τ is a moment, r is a vector from the force the moment measure point, F is force, $\frac{d^2v}{dx^2}$ and $\frac{1}{\rho}$ 1/ρ are curvature, and EI is flexural rigidity.

The second derivative of deflection can be approximated by curvature in the slight deflection. COMSOL analyzed the second derivative of deflection on the green line, shown in Figure 3.21. The resulting plot, shown in Figure 3.22, representing the second derivative of the deflection in step 5, displays four concave planes corresponding to the etching parts. This indicates curvature occurs precisely at the etching parts where moments are generated.

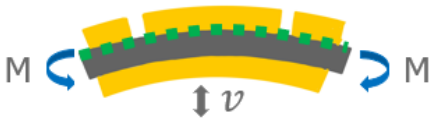

Figure 3.21: Schematic of the moment on the substrate and the stress distribution

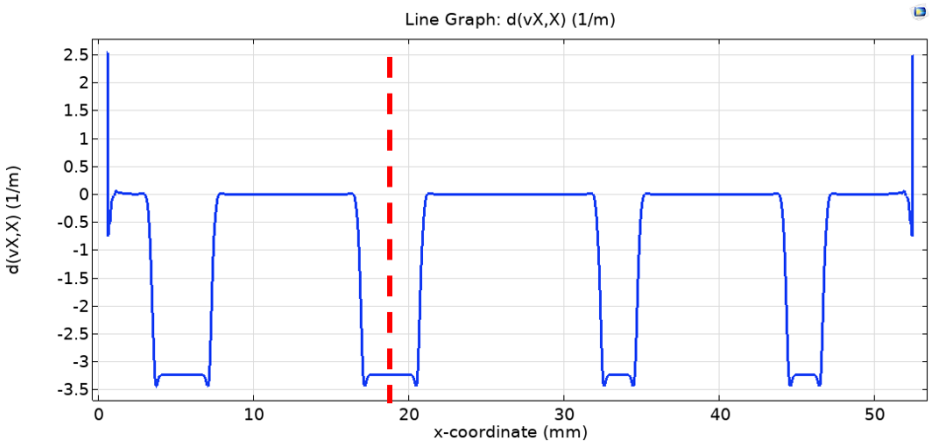

Figure 3.22: The line chart of the second derivative of deflection

To further illustrate the moment within the substrate during the process, the stress distribution in the cross-section of the etching position where is the red line in Figure 3.22 is examined. The figure 3.23 shows the result, which also used step 5 as a representative case.

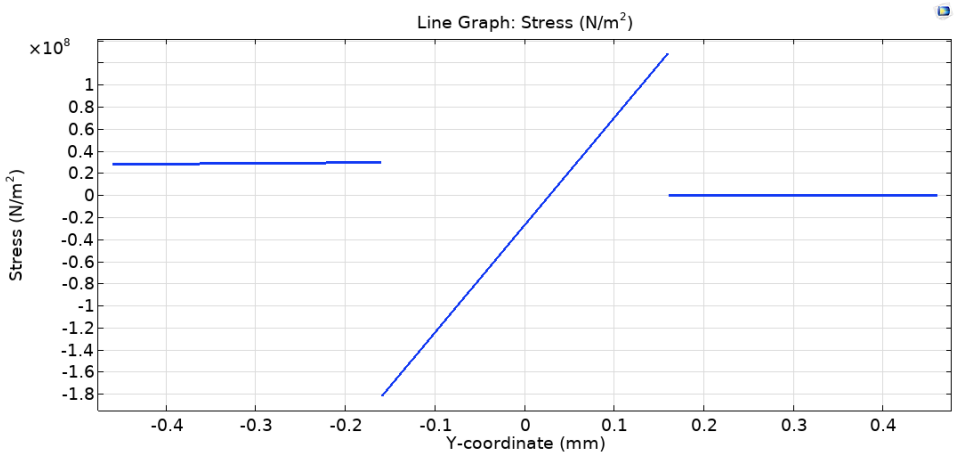

Figure 3.23: The stress distribution in the cross-section of the etching part at step 5

Due to the stress and moment equilibrium, the total value of stress and moment in this cross-section is zero. To facilitate moment calculation, the stress on the copper layer is treated as an external force, focusing on the stress distribution in the ceramic layer, which is the slope in the middle of Figure 3.23. The thickness of the ceramic layer is 0.32mm, but the zero-stress position is slightly offset from the center. To place the pivot point at the center of the ceramic layer's thickness and align with the zero-stress position, a translation of stress is performed. This ensures that the stress in the cross-section creates a couple of forces while maintaining force equilibrium, resulting in a remaining moment. To achieve a couple of forces, the calculation involves averaging the maximum and minimum stress values on the ceramic layer and subtracting this average stress value from the stress distribution on the ceramic layer. Figure 3.24 illustrates the force-translated concept.

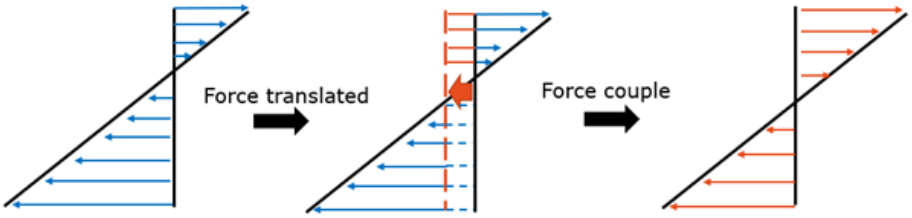

Figure 3.24: The schematic of force translated

To demonstrate the equilibrium of forces within the substrate, the following mathematical calculation is performed, along with a schematic illustration in Figure 3.25. Consider the equation of the original slant line:

$$y_1 = ax + b$$

The equation of the translated slant line, represented by the dashed line in Figure 3.25, after being moved a distance c, is:

$$y_2 = y_1 + c = ax + b + c$$

Calculate the average value of the maximum and minimum stress on the original slant line to get,

$$\frac{1}{2} \times (stress_{max} + stress_{min}) = \frac{1}{2} \times (ah + b + b) = \frac{1}{2}ah + b$$

To calculate the integral of the area covered by the translated slant line, the equation is integrated

$$\int_0^h y_2\,dx = \int_0^h ax + b + c\,dx = \frac{1}{2}ah^2 + bh + ch$$

If the translated slant line represents a couple of forces in equilibrium, the integral of the area covered by the translated line should be zero. Therefore, the value of c can be determined as

$$c = -\frac{1}{2}ah - b$$

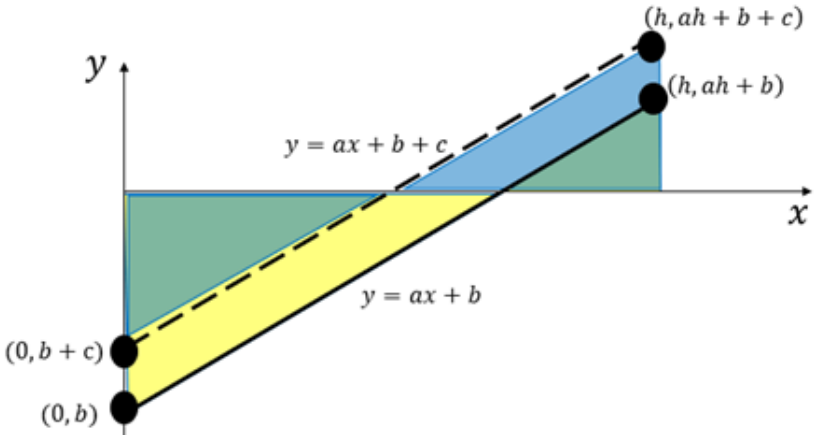

Figure 3.25: The demonstrating schematic of the force translated in slant line

As a result, the c value corresponds to the average value of the maximum and minimum stress on the original slant line. The new slant line is a force couple. This means that the translated slant line represents a force couple. Therefore, the moment of the ceramic cross-section can be calculated as follows:

$$\sum_{n=1}^{m} r \times F_{xx} = \int r \times \sigma\,dA$$

σ is XX direction stress, r equals y value, due to the divot point of force couple is at 0[mm].

The line graph in Figure 3.26 illustrates the distribution of the moment and strain within the substrate. Throughout the entire process, the moment value closely corresponds to the variation in warpage deformation. Initially, the moment is zero, but it decreases to a negative value after the etching process, which generates the initial warpage. During the annealing process at 280 °C, the moment increases to a large positive value. The sign change from negative to positive presents the warping direction changes from convex to concave. Finally, during the cooling session, the moment decreases further to a larger negative value compared to the value in step 3. This trend in moment values reflects the corresponding changes in warpage deformation. Compared with the strain value variation, although it also has a similar trend of the distribution, it doesn't clearly reflect the part where the initial warpage generates due to the strain illustrated by the horizontal deformation. This correlation indicates the moment is a crucial factor influencing the warpage deformation during the process.

In conclusion, the discussion above concerns stress-induced elastic, plastic, and thermal strain during the process. The non-reversible characteristic of plastic strain plays a crucial role in developing

permanent warpage. Furthermore, the stress distribution within the substrate generated moments that contribute to the occurrence of warpage. The trend observed at the moment distribution closely aligns with the deformation pattern of the warpage.

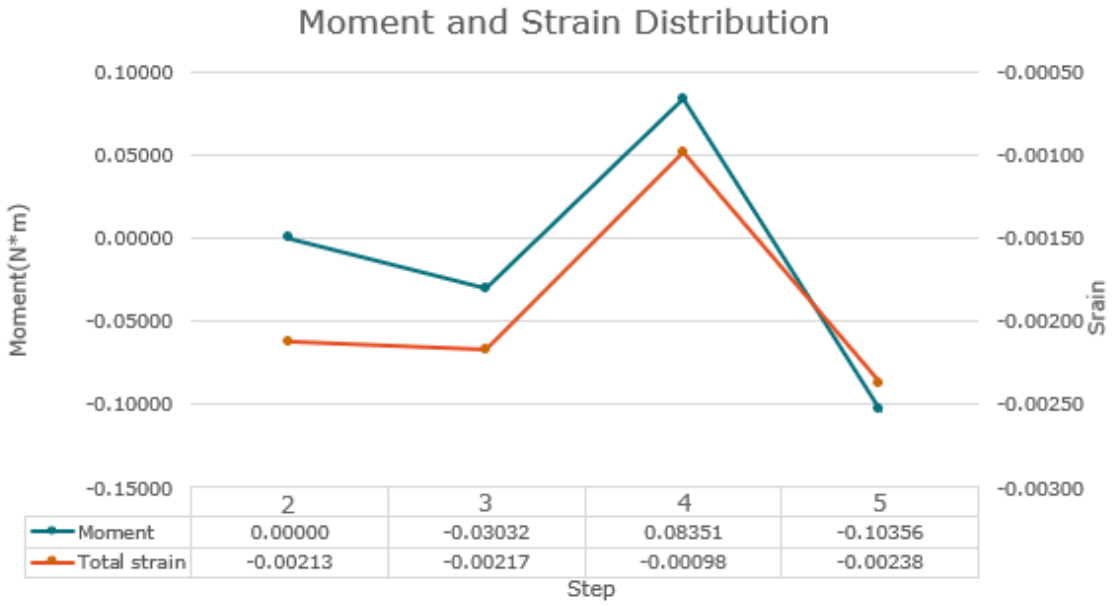

Figure 3.26: The line chart of the moment and strain distribution in the process step

3.7. Chapter summary

This chapter provides a comprehensive exploration of the manufacturing process of AMB substrates and delves into the underlying causes of warpage deformation. The process initiates with active metal brazing at 800°C, followed by cooling and etching at 20°C, leading to the generation of an initial convex warpage. Subsequent annealing at 280°C induces concave warpage, and further cooling to 20°C results in a significant convex warpage that is 4.3 times larger than the initial warpage.

For the construction of the FEM simulation model, the material properties of annealed copper are extracted through CTE measurements and tensile tests conducted at various temperatures. The obtained values include a CTE of 16.7×10^{-6}, a room temperature yield stress of 18.8 MPa, and a tangent modulus of 674.4 MPa.

To simulate the 2D FEM model, the boundary conditions prevent rotation and slippage by imposing zero displacement constraints on specific corner points. The simulation results reveal that warpage is primarily induced by variations in moments within the substrate. The moment is closely linked to the distribution of strain. The initial warpage arises from the elastic strain imbalance introduced during the etching process. Furthermore, the final warpage is attributed to plastic deformation occurring within the copper layer, which imparts an irreversible change resulting in substantial warpage variation. Importantly, the FEM simulation not only identifies the principal cause of the warpage but also accurately mirrors the observed warpage variation documented in the experimental results.

4

Effect of Substrate Geometry on Warpage

4.1. Chapter introduction

This chapter presents the FEM simulation results for two reference substrate samples, FRT and BSM, from different AMB substrate suppliers. These simulations are based on the manufacturing process, encompassing various heat treatments to assess their influence. Additionally, annealing experiments and subsequent warpage measurements are conducted and validate the simulation outcomes. Furthermore, the chapter delves into influence factor analysis of the optimal structural design employing response surface methodology (RSM). This analysis allows for aiding in creating an optimized structural design within the given layout parameters.

4.2. Sample reference of AMB substrate

Two different AMB samples with various dimensions and copper thicknesses were adopted COMSOL software to simulate and verify the warpage of 3D structures. To determine the dimensions of the substrates, the Dino-lite USBs microscope camera and Dino-Capture software were employed to capture detailed substrate images and measure the pattern dimension. Subsequently, a 3D substrate model was created using Inventor, a computer-aided design (CAD) software for mechanical modeling. Figure 4.1 presents the pictures of substrates and the 3D model built by CAD software. The area with silver metalization was ignored in the CAD model due to the negligible thickness.

The materials of each layer for both substrates from top to down are copper, ceramic, and copper. However, sample FRT has a thicker thickness of copper and grain size of copper compared with sample BSM. Table 4.1 shows the detailed dimension and grain sizes for both samples.

(a) Figure of sample BSM

(b) Figure of sample FRT

(c) 3D CAD Model of sample BSM

(d) 3D CAD Model of sample FRT

Figure 4.1: Figures and 3D CAD model of two reference substrates

Table 4.1: Spec of sample BSM and FRT

Sample	Sample BSM	Sample FRT
Dimension	53 mm $\times$ 39 mm	44.4 mm $\times$ 49 mm
Thickness (Cu/Si_3N_4/Cu)	0.3 mm/ 0.32 mm/ 0.3 mm	0.8 mm/ 0.32 mm/ 0.8 mm
Grain size	488.8 µm	733.45 µm

For the grain size quantification, the average grain intercept method was employed. This technique involves randomly drawing line segments across images and counting the number of grains intersected. The formula expresses the calculation:

$$Grainsize = \frac{number\,of\,grains}{line\,length}$$

The Keyence optical microscope was adapted to capture detailed images of the substrate, as depicted in Figure 4.2. For sample BSM and FRT, micrographs are illustrated in Figure 4.2a and 4.2b, respectively. The software, Image J, was utilized to process the images, positioning the line segments to determine grain size for both sample BSM and FRT. The computed grain size results for sample BSM

and FRT are 488.8 µm and 733.45 µm, respectively, as presented in Table 4.1.

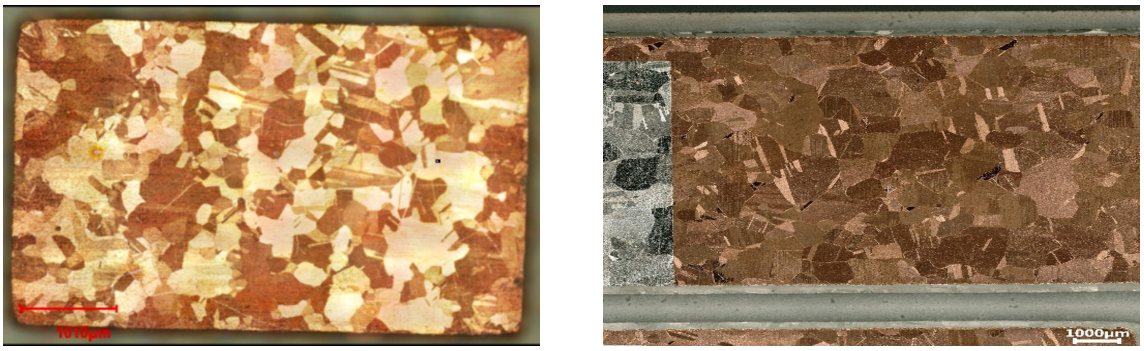

(a) Micrograph of sample BSM

(b) Micrograph of sample FRT

Figure 4.2: Micrograph of samples

4.3. FEM simulation of AMB reference sample

4.3.1. FEM model of AMB reference sample

In order to initiate the simulation, the 3D CAD file was imported into COMSOL software. The material properties were configured based on the data provided in Table 3.3, Table 3.4, and Table 3.5. Due to the simulation's three-dimensional nature, constrained displacements were defined, as illustrated in accompanying Figure 4.2. Figure 4.3 presents that boundary conditions were established at three specific points, denoted as A, B, and C, located at the three corners of the bottom copper layers. These boundary conditions restricted movement and rotation in those regions and constrained the movement exclusively along the z-axis for the four-sided ceramic layer, represented as D, as orange lines in Figure 4.3. Additionally, Figure 4.3 displays the outcome of the free tetrahedral mesh, along with the positions of the fixed points.

Figure 4.3: The schematic of the boundary condition of substrate

Table 4.2: Boundary condition of FEM simulation

Pre-displacement	Point A	Point B	Point C	Line D
X(mm)	0	Free	0	Free
Y(mm)	0	0	Free	Free
Z(mm)	0	0	0	0

The simulation began by simulating the cooling process of the structure with two symmetrical copper layers positioned atop and beneath the middle ceramic layer, starting from 800 °C and gradually reaching 20 °C. Subsequently, in order to model the etching procedure, the trenches, and circles on the pattern, which were utilized for the electrical isolation and solder stop, were rendered deactivated in this particular step. This deactivation function effectively reduced a large amount of the stiffness and density to render them non-existent. Since the substrate comprised an expansive master card measuring 190mm × 138mm, the giant mastercard was sectioned into pieces to become a small substrate. During the segmentation process, the z-displacement of the ceramic layer was essentially released. Consequently, in step 3, constraint D was eliminated, representing the initial warpage of the process. The subsequent phase simulated the annealing process, whereby the ambient temperature was elevated to 280 °C in step 4. Then, the substrate cooled down to 20 °C in the final step. The manufacturing process details are depicted in Figure 4.4.

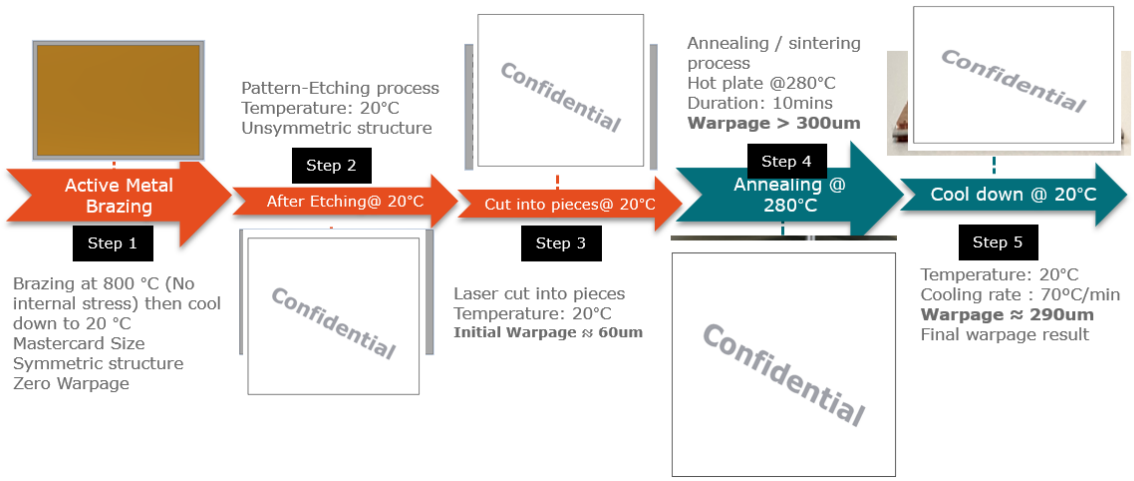

Figure 4.4: Simulation process flow of AMB substrate

4.3.2. FEM simulation results of AMB reference sample

The subsequent results of the simulation, based on the FEM settings mentioned in subsection 4.3.1, depict the simulation warpage of the substrate before and after the annealing process. This sub-chapter presents these results, including 3D perspectives and 1D cross-sections of the warpage. The 1D simulation result is the line on the top copper layer. The central line of sample BSM is considerably concealed by the trench, thereby impacting the observation of the warpage. Consequently, a black dashed line is utilized in Figure 4.5 to denote the position for measuring warpage deformation. This approach facili-

tates precise measurements in the experiment, particularly due to its crosses multiple holes within the pattern, ensuring accurate assessment.

Figure 4.5: The schematic of the 1D measurement position

1. Warpage deformation in the manufacturing process in FEM simulation

   Following the simulation setting mentioned above, Table 4.3 presents the simulation results for sample BSM, illustrating the z displacement at various stages. The warpage deformation starts from -5 µm, 62.8 µm, -220.7 µm and ends up with 227.5 µm. It illustrates the progression of warpage deformation, beginning from nearly zero warpage, the generation of the initial warpage, the emergence of convex warpage during annealing, and culminating in pronounced concave warpage. This depiction mirrors the same deformation trend in Figure 3.1.

Table 4.3: Warpage deformation in the manufacturing process in FEM simulation

Sample	Sample BSM	
Step	2	3
Warpage	-5 µm	62.8 µm
Result	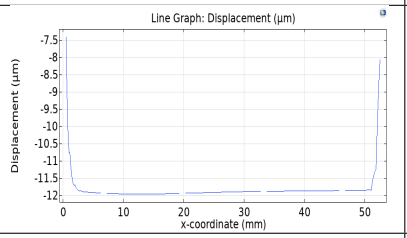	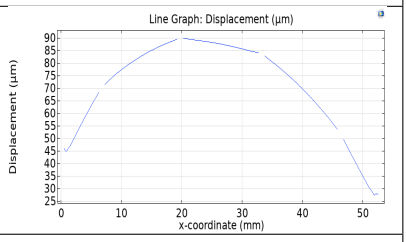
Step	4	5
Warpage	-220.7 µm	277.5 µm
Result	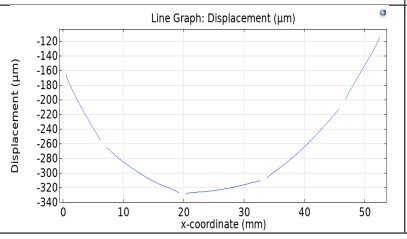	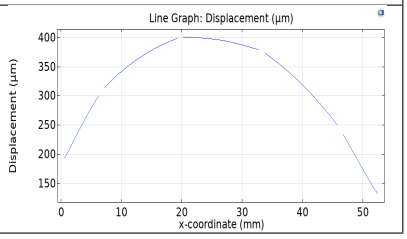

2. Initial warpage and final warpage result in FEM simulation

Table 4.4 presents the warpage simulation result before and after the annealing process for both substrates in 3D perspective, 1D view, and the warpage value. The initial and final warpage of sample BSM is 62.8 µm and 263.1 µm, respectively, while sample FRT is 32.7 µm and 116.5 µm, respectively. The warpage changes for samples BSM and FRT, calculated as the final warpage divided by the initial warpage, are 418.9 % and 356.3 %, respectively. The simulation results clearly show a significant difference in warpage caused by the annealing process.

Table 4.4: Initial Warpage and Final Warpage result in FEM simulation

Sample	Sample BSM	Sample FRT
Initial warpage	62.8 µm	32.7 µm
Before annealing 3D perspective		
Before annealing 1D perspective	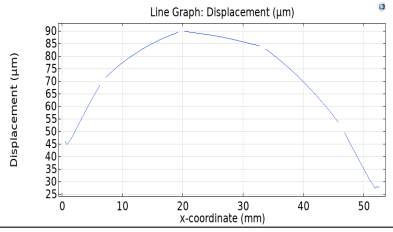	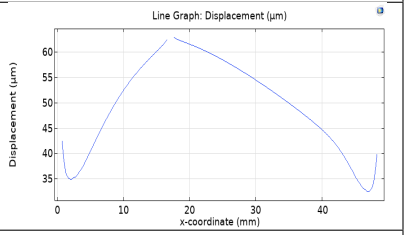
Final warpage	263.1 µm	116.5 µm
After annealing 3D perspective		
After annealing 1D perspective	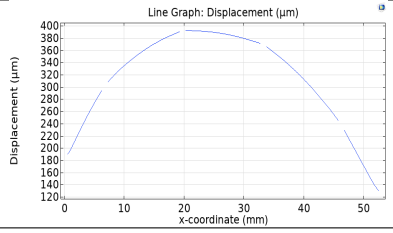	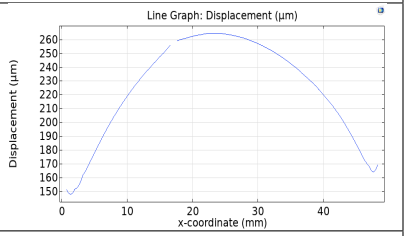
Warpage change ($\frac{Finalwarpage}{Initialwarpage} \times 100\%$)	418.9 %	356.3 %

3. Warpage simulation result after different annealing temperature

The simulation explored the relationship between the annealing temperature and the warpage value. The simulation encompassed a series of four distinct temperature steps, starting at 140 °C

and progressing through 185 °C, 230 °C, and culminating at 280 °C. Every temperature step was an iterative annealing cycle comprising heating up to the specific temperature and cooling down to a room-temperature session. The sample BSM was adopted as the chosen specimen for this analysis. The simulation results are presented in Table 4.5, illustrating the final warpage value under different annealing temperature conditions. The final warpage under different annealing temperature conditions: 205.9 µm, 214 µm, 223.5 µm, and 244.8 µm, respectively. The variation of the final warpage concerning annealing temperature can be visualized in Figure 4.6. From the results, it is evident that there is a positive correlation between annealing temperature and warpage. As the annealing temperature increases, the change in the final warpage becomes more significant, indicating a stronger influence of higher temperatures on the warpage of the sample BSM.

Table 4.5: Warpage simulation result after different annealing temperature

Temperature	140 °C	185 °C
Final warpage	205.9 µm	214 µm
Figure	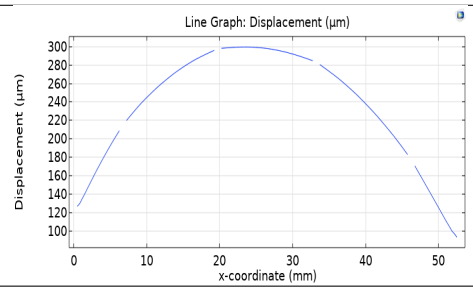	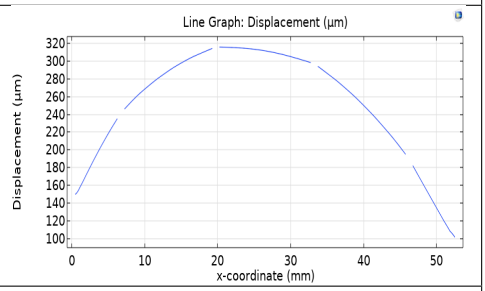
Warpage change	327.8 %	347.7 %
Temperature	230 °C	280 °C
Final warpage	223.5 µm	244.8 µm
Figure	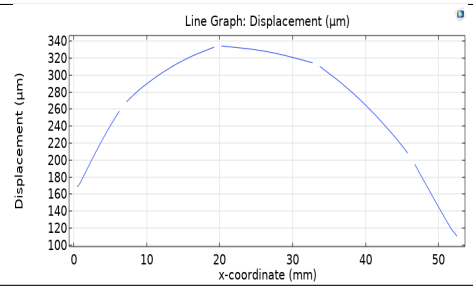	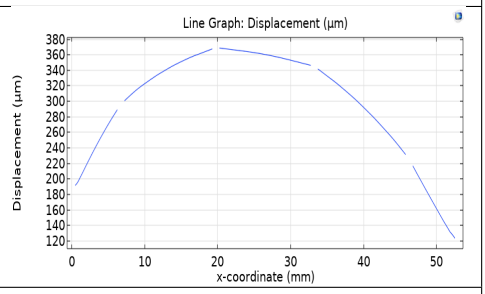
Warpage change	355.9 %	389.8 %

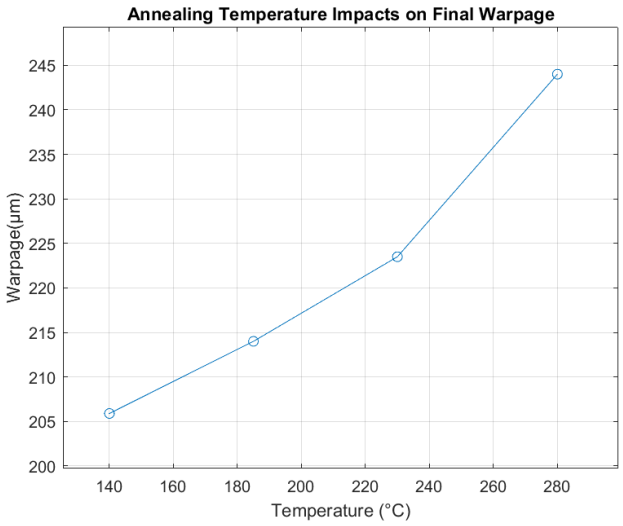

Figure 4.6: Correlation between annealing temperature and final warpage in FEM simulation

4. Warpage simulation result after multiple annealing sessions

   The simulation also incorporated multiple annealing sessions to investigate whether repeated heating and cooling cycles affect the warpage. In the simulation setup, two additional annealing sessions were introduced in addition to the original setting. As a result, a total of three annealing cycles at 280 ° C were simulated in the model. The final warpage, shown in Table 4.6, after each annealing cycle, is 263.1μm, 276.4μm, and 286.5μm, respectively. The simulation result presents the sightly increase on the final warpage.

Table 4.6: Warpage simulation result after multiple same temperature annealing sessions

Sample	Sample BSM		
Annealed	280 °C		
Cycle Number	First	Second	Third
Warpage	263.1 μm	276.4 μm	286.5 μm
Result	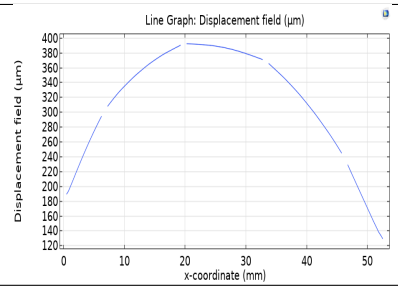	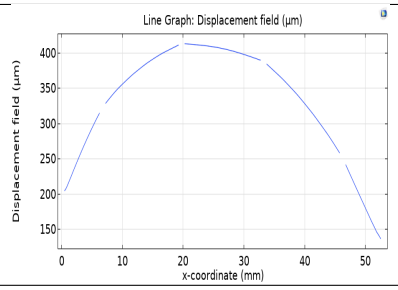	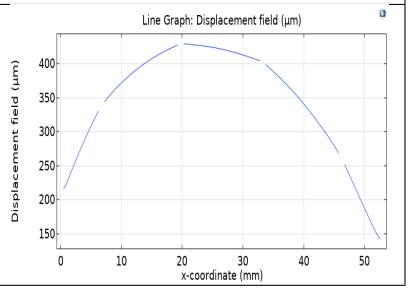

4.4. Warpage measurement of AMB reference sample

4.4.1. Annealing experiment

Subsection 4.3.2 discussed the warpage variation before and after the annealing process in FEM simulation. To validate the simulation result, the warpage of substrate before and after the annealing

process was experimented with and measured using microscope equipment. A high-speed heating system, the Tresky To-Heating unit, shown in Figure 4.7, was used in the annealing experiment. In the experiment, the substrate was put on a hot plate, which was heated by the Tresky To-Heating unit and covered with a 50 µm PTFE foil and steel cover on top of it to insulate air. The heating rate was 13 °C/sec, starting from room temperature to 280 °C and dwelling at that temperature for 10 minutes, then cooling down to room temperature. The whole temperature flow, illustrated in Figure 4.8, followed a sintering process temperature setting. During the heating, the nitrogen gas with a 5 L/min rate was ejected inside the chamber to prevent oxidation. Warpage value was measured before and after the annealing experiment following the dashed line in Figure 4.5.

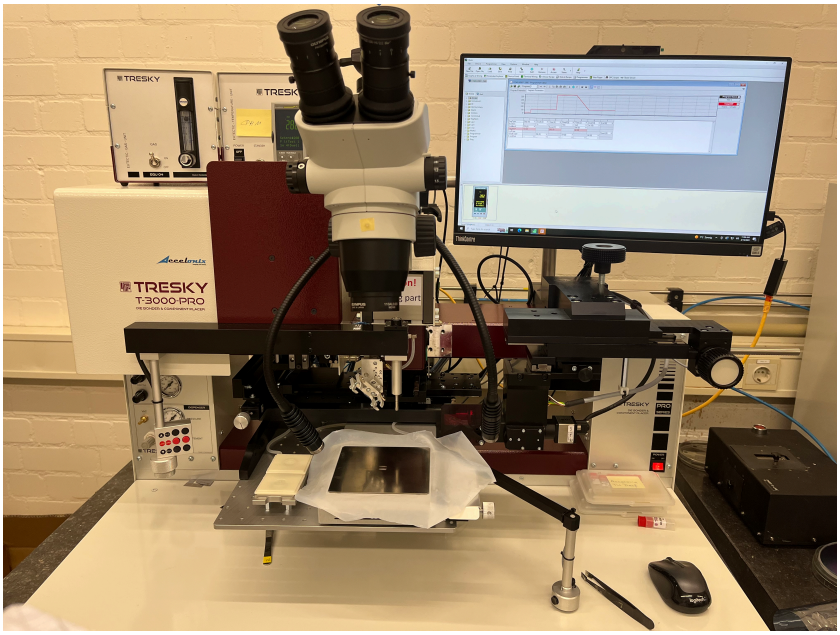

Figure 4.7: A picture of high-speed heating equipment

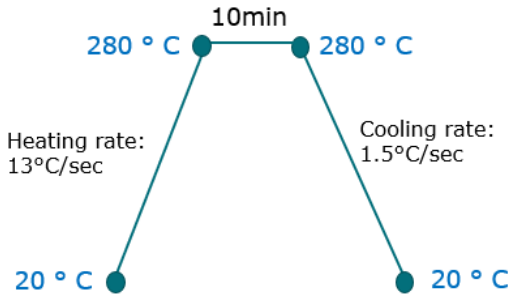

Figure 4.8: Annealing experiment temperature setting

4.4.2. Equipment for Warpage measurement

To determine the warpage value and shape of the substrate, a VKX-200 laser confocal microscope and a VR series wide-area 3D microscope were used, depicted in Table 4.7. These non-contact 3D surface profiles detected height variation, surface roughness, dimension, and other related parameters.

Table 4.7: The comparison of warpage measurement wquipment

Equipment	VKX-200 (laser confocal)	VR-5000
Resolution	1 nm	0.1 μm
Field of view range	narrow	wide
Principle	Laser+optical	Optical
Location	EKL	Aerospace
Measurement period	2 hour(One strip)	1 min (Full view)
Equipment picture		
Result	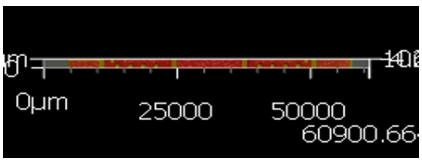	

The VKX-200 microscope incorporates two light sources, which are white light and laser source, to get the height information and color information, respectively. The laser source is a point light source capable of scanning the field of view using an X-Y scanning optical system. A light-receiving element detects the reflected light from each pixel. At the same time, the objective lens adjusts along the Z-axis to capture the reflected light intensity at different Z-axis positions. The highest intensity of reflected light corresponds to the focal point, which provides height information. Meanwhile, the CMOS camera captures color information by detecting the reflected light from the white light source. This process involves capturing multiple two-dimensional images at different depths and stitching them together to create a three-dimensional structure. The specific equipment used is VKX-200 with 0.1nm resolution in EKL CR100.

On the other hand, the wide-area 3D microscope in the VR series is equipped with two cameras: one for low magnification, providing a broader field of view, and another for high magnification, offering high resolution. Structured light is emitted from the transmitter lens and projected onto the surface of the object. The receiver lens detects the reflected light, which contains information about surface topography, including any bands or bends. Triangulation is then utilized to measure the height variance of the surface. The particular equipment is the VR-5000 with a resolution of 0.1 μm, located in the Material Physics Lab at TU Delft aerospace department.

In terms of performance, the VKX-200 has a higher resolution, while VR-5000 offers faster measurement speed. Consequently, for the subsequent measurement, the VKX-200 is used for one-line

measurement, while the VR-5000 is utilized for full-picture measurement. Considering the resolution, the following measurement would be done by VKX-200.

4.4.3. Warpage measurement results

Using the laser confocal equipment, the measurements of the substrate's warpage are presented as follows:

1. Initial warpage of reference samples

   Table 4.8 displays the initial warpage measurement results for samples BSM and FRT. Initial warpage refers to the warpage of the substrate as provided by the supplier prior to any additional manufacturing process, such as annealing. The initial warpage of sample BSM is 66.72 µm, and sample FRT exhibits an initial warpage of 44.1 µm.

Table 4.8: The initial warpage measurement result of substrates

Sample type	Sample BSM	Sample FRT
Initial warpage	66.72 µm	44.1 µm
Result	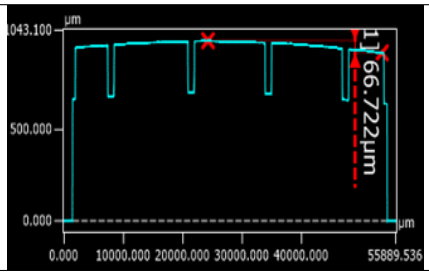	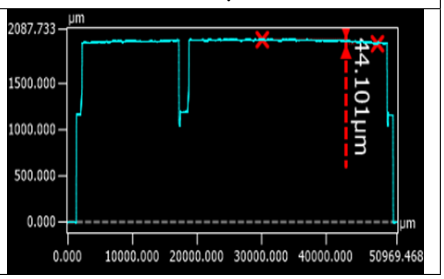

2. Warpage after the annealing process

   Table 4.9 presents the warpage measurements at room temperature after finishing the 280 °C annealing experiment. The final warpage of sample BSM is recorded as 268.25 µm, while sample FRT exhibits a final warpage of 143.18 µm. Comparing these values with the initial warpage, it is observed that the warpage changes of sample BSM and FRT are 429 % and 324.7 %, respectively, after the annealing process.

Table 4.9: The warpage measurement result after annealing process

Sample type	Sample BSM	Sample FRT
Final warpage	286.25 µm	143.18 µm
Warpage change ($\frac{Finalwarpage}{Initialwarpage} \times 100\%$)	429 %	324.7 %
Result	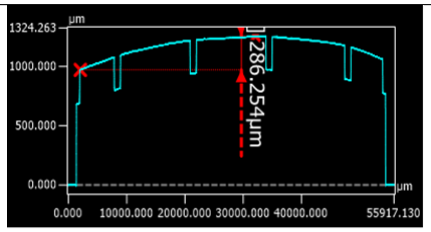	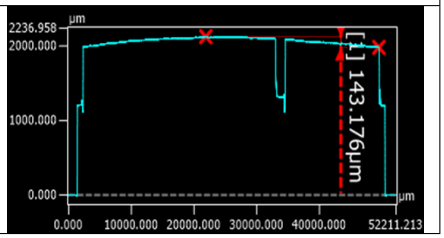

3. Warpage after different annealing temperature

   During the experiment, the relationship between warpage and annealing temperatures is examined. Sample BSM is subjected to different annealed temperatures, specifically 140 °C, 180 °C, 230 °C, and 280 °C, respectively. The warpage measurements, as displayed in Table 4.10, are recorded at room temperature after the annealing process is finished. All measurements were consistently taken from the same position. However, due to the substrate's orientation was reversed during measurements for temperatures of 140 °C and 230 °C. These specific figures' results in Table 4.10 are mirrored compared with others.

Table 4.10: The warpage measurement result after different annealing temperatures

Sample	Sample BSM	
Temperature	140 °C	180 °C
Final warpage	174.78 µm	203.97 µm
Warpage change ($\frac{Finalwarpage}{Initialwarpage} \times 100\%$)	282.2 %	329.3 %
Result	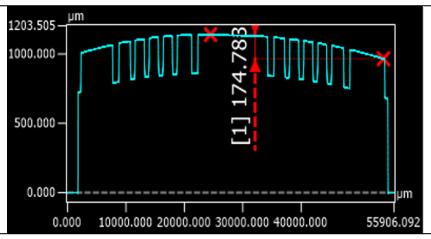	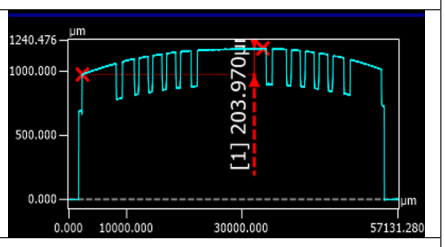
Temperature	230 °C	280 °C
Final warpage	251.1 µm	285.6 µm
Warpage change ($\frac{Finalwarpage}{Initialwarpage} \times 100\%$)	429 %	463 %
Result	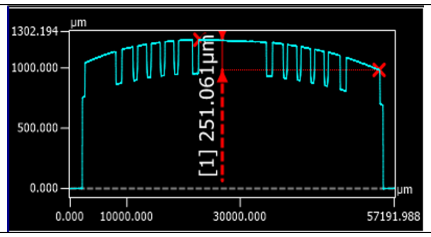	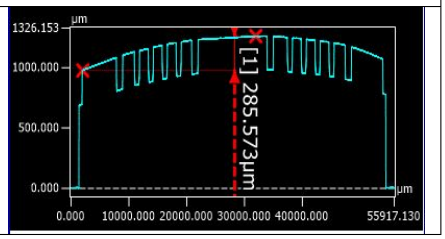

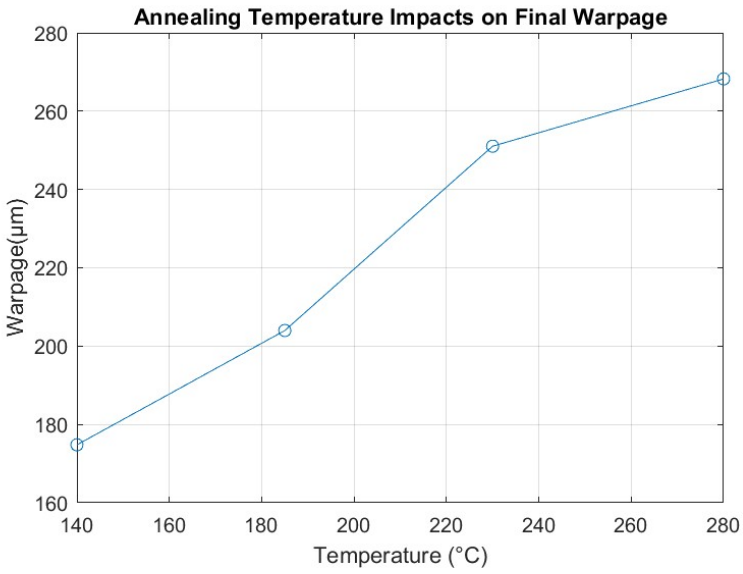

Figure 4.9: Correlation between annealing temperature and final warpage

4. Multiple annealing session

   The investigation considered the impact of multiple heat and cool sessions. In the experiment, sample BSM underwent three annealing sessions at 280 °C, and the warpage after each session was recorded, as shown in Table 4.11. Observing the table, the warpage value fluctuated between 286.25 µm to 307.36 µm, resulting in a variance of 21 µm. The warpage slightly increases in the second round but reduces to 293.21 µm in the third round. Notably, the maximum floating variance accounts for only 7.3 % of the warpage value recorded in the first round of annealing. As a result, the amplitude of warpage variation in the multiple annealing experiments is not significant. It can be concluded that the most significant influence on warpage deformation occurs during the initial annealing round.

Table 4.11: The warpage measurement result after different annealing cycles

Sample	Sample BSM		
Annealed	280° C		
Cycle Number	First	Second	Third
Warpage	286.25 µm	293.22 µm	307.36 µm
Result	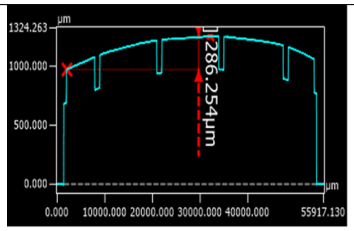	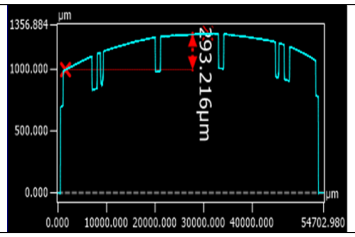	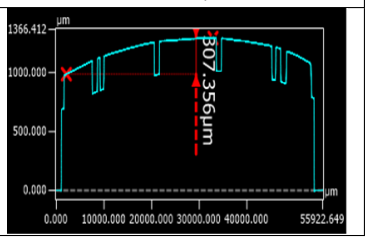

4.5. Comparison of simulation and experimental results

Both the FEM simulation and annealing process experiment implemented the warpage deformation analysis. The results of the data are going to be compared in this section.

1. Comparison of the initial and final warpage data

   Table 4.12 compiles the initial warpage, final warpage, and warpage change based on simulation and experimental results for sample BSM and FRT. The final warpage of BSM in both results is approximately more than four times different than the initial warpage, while for sample FRT, it is around three times different. sample FRT exhibits a more significant difference in warpage results than sample BSM. The thicker copper layer This is attributed to the fact that sample FRT has a copper layer that is 2.3 times thicker than sample BSM. The comparison reveals that the warpage simulation results are consistently smaller than the experimental results for both substrates. This divergence can be attributed to the simulation's initiation at a high temperature of 800 °C. This comprehensive temperature range from 800 °C to 20 °C incorporates copper volume shrinkage, contributing to the data collection. The initial and final warpage results in the simulation consider the copper shrinkage in the first step. However, in contrast, the experimental results solely focus on the warpage disparity during the annealing process. Consequently, the variations in warpage values are influenced by this contrasting scope of analysis. Also, the inaccurate material properties based on the CTE and tensile test experiment can contribute to the error between the simulation and experiment results.

Table 4.12: The initial and final warpage comparison

Sample	Sample BSM		Sample FRT	
Data type	Simulation	Experiment	Simulation	Experiment
Initial Warpage	62.8 µm	66.72 µm	32.7 µm	44.1 µm
Final Warpage	263.1 µm	286.25 µm	116.5 µm	143.18 µm
Warpage change ($\frac{Finalwarpage}{Initialwarpage} \times 100\%$)	418.9 %	429 %	356.3 %	324.7 %

2. Comparison of warpage in the different annealing temperature

   Table 4.13 compares the final warpage results obtained after subjecting the sample to different annealing temperatures ranging from 140 °C to 280 °C. Both the simulation and experimental results show an increasing trend in the final warpage with higher annealing temperatures. However, it is observed that the experimental results exhibit a more significant change in warpage compared to the simulation results.

   This error is because of the inaccurate material properties model, which is extracted from CTE and tensile tests. As described in Table 3.5, which outlines the material properties of copper used in the simulation model, properties beyond 250 °C are not provided due to measurement limitations. Additionally, properties like tangent modulus do not show a substantial change between temperature differences due to the influence of displacement measurement by the cross-head.

Consequently, the simulation's warpage changes do not exhibit as pronounced differences as the experimental results, where the actual annealing process substantially impacts the warpage of the sample.

Table 4.13: The warpage in different annealing temperature comparison

Sample	Sample BSM			
Temperature	140 °C	185 °C	230 °C	280 °C
Simulation Warpage	205.9 μm	214 μm	223.5 μm	244.8 μm
Experiment Warpage	174.78 μm	203.97 μm	251.06 μm	287.3 μm
Simulation Warpage Change ($\frac{Finalwarpage}{Initialwarpage} \times 100\%$)	327.8 %	347.7 %	355.9 %	389.8 %
Experiment Warpage Change ($\frac{Finalwarpage}{Initialwarpage} \times 100\%$)	282.2 %	329.3 %	429 %	463 %

3. Comparison of warpage in several annealing cycles at 280 °C

   The simulation and experimental warpage results, each of which underwent three annealing cycles, are recorded in Table 4.14. There is no substantial difference, no more than 24 μm, in the warpage between each heating session and between the simulation and experimental results. However, oth results show at least a 20 μm warpage difference between the first and the third heating cycle. The most substantial warpage change occurred during the first annealing session. In contrast, in the subsequent second and third annealing cycles, the accumulated plastic deformation within the structure caused a slight increase in the warpage value, but the change was not remarkable.

Table 4.14: The warpage in several annealing cycles at 280 ° C comparison

Sample	Sample BSM		
Cycle Number	First	Second	Third
Simulation Warpage	263.1 μm	276.4 μm	286.5 μm
Experiment Warpage	286.25 μm	293.22 μm	307.36 μm

Through a comparison of simulation and experimental findings, a compelling alignment between the two is evident. This congruence underscores the simulation's capacity to replicate the experimental outcomes, thereby confirming the validation of the Finite Element Method (FEM) model through experimental verification. This robustly validated model will be a reliable foundation for subsequent optimization endeavors.

4.6. Factor analysis of structural design

After demonstrating the simulation and measurement results show a similar warpage trend as the manufacturing process, it is essential to analyze the impact of copper's pattern design factor on warpage behavior. A simplified AMB structure was created within the COMSOL software to achieve the goal. The structure comprised three copper pads of identical length and width on the front side of the substrate, as well as a complete copper pad on the back side, as illustrated in Figure 4.10. This pattern design was derived from considerations in MOSFET (Metal-Oxide-Semiconductor Field-Effect Transistor) signal transmission and factor analysis. Specifically, MOSFET involves three pinouts—gate, source, and drain—thus necessitating the design of three copper pads. Moreover, choosing a regular geometric shape for this pattern design aims to streamline factor analysis, enabling clearer influence observation.

The figures present a schematic representation of the structure and highlight the specific positions and symbols of the representative variables. The simplified structure is utilized to investigate the influence of factors such as the edge between copper and ceramic, the presence of the copper trench, and its thickness. Specifically, Cu_s represents the thickness of front two-sided copper pads on the front side; Cu_m denotes the thickness of the middle copper pad on the front side of copper; Cu_b indicates the thickness of the back side copper pad; gap_f signifies the width of the edge between the ceramic and front side copper layer in the x and y directions; gap_b represents the width of the edge between the ceramic and backside copper layer in x and y directions. Lastly, gap represents the trench width between the front side copper pads.

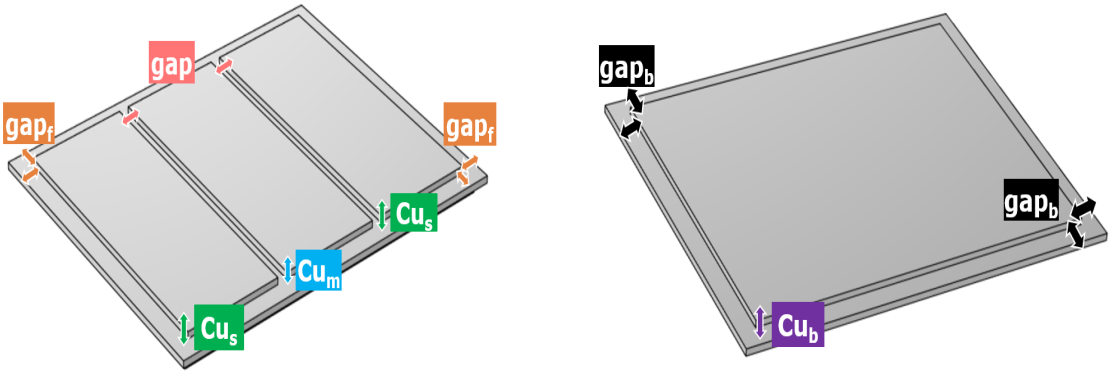

(a) Schematic of the front side three copper pads AMB substrate

(b) Schematic of the back side of AMB substrate

Figure 4.10: Schematic of the AMB substrate for factor analysis

Table 4.15: The symbol and value range of the influence factor

Variable		Minimum	Maximum
Thickness	Cu_s	0.3mm	0.8mm
	Cu_m	0.3mm	0.8mm
	Cu_b	0.3mm	0.8mm
Edge	gap_f	0.5mm	1.5mm
	gap_b	0.5mm	1.5mm
Trench	gap	0.5mm	1.5mm

To comply with the AMB substrate design rule from suppliers, certain limitations were imposed on the thickness of the copper and the dimensions of the edge and trench. To follow the design rules, the copper thickness on both sides varied in the Design of Experiment (DOE), set explicitly from 0.3 mm to 0.8 mm. Similarly, the edge and trench dimensions ranged from 0.5 mm to 1.5 mm. The parametric sweep function was employed to simulate the DOE outlined in Table 4.15, which generated simulations for all combinations of the sweep parameters. The parameters were based on a central composite design rule built inside the Design-Expert software, which incorporated the mathematical and statistical methods of Response Surface Methodology (RSM). It also offered analytical and graphical tools to aid in interpreting results. Table 4.16 presents nine warpage results corresponding to different parameter settings. The complete data for the simulation results can be found in Appendix C. RSM was employed to analyze the correlation between Warpage and various variables.

Table 4.16: The warpage results corresponding to different parameters

Factor	$Cu_s[mm]$	$Cu_m[mm]$	$Cu_b[mm]$	$gap_f[mm]$	$gap_b[mm]$	$gap[mm]$	$Warpage[\mu m]$
1	0.3	0.3	0.3	0.5	0.5	0.5	63.8
2	0.3	0.3	0.8	1.5	0.5	0.5	1351.4
3	0.3	0.8	0.3	0.5	1.5	1.5	-635.1
4	0.3	0.8	0.8	1.5	0.5	0.5	790.4
5	0.55	0.55	0.55	1	1.8	1	94.9
6	0.8	0.3	0.3	0.5	1.5	1.5	-500.8
7	0.8	0.3	0.8	0.5	1.5	0.5	805.5
8	0.8	0.8	0.3	0.5	1.5	1.5	-949.4
9	0.8	0.8	0.8	1.5	1.5	0.5	75.9

RSM is a statistical technique widely used for system optimization and process improvement. It allows for exploring relationships between variables and response results by fitting a mathematical model such as linear, cubic, quadratic, etc. To analyze the relationships and determine the significance of different parameters, the analysis of variance (ANOVA) method is utilized. ANOVA helps identify the parameters that have the most significant impact on the dependent variable and establishes the relationship between the dependent and independent variables. To facilitate these analyses, the Design Expert software was employed. It offered analytical and graphical tools to aid in the interpretation of results. The statistical analysis began by importing the simulation results from Table 4.16 and Appendix C into

the Design Expert software. Then, by assessing the p-value to determine the significance and adaptability of the coefficient of determination, the suitable linear model is chosen. The linear equation with interaction terms is

$$Y = \beta_0 + \sum_{i=1}^{k} \beta_i x_i$$

,where β_0, β_i are regression coefficients for intercept and linear coefficients respectively, x_i is independent variables.

Next, the ANOVA method was employed to analyze the results, and the findings are presented in Table 4.17. The table contains the model and fit statistics. The model encompasses all the variations that impact the response and is used to calculate significant characteristics. It considers various factors that contribute to the response. The fit statistics show the adjusted and predicted regression value to present how the analysis model can fit with the data.

Table 4.17: The warpage results corresponding to different parameters

Source	Sum of squares	F-Value	P-value	
Model	4.44×10^7	686.72	<0.001	significant
Cu_s	6.07×10^6	563.7	<0.001	significant
Cu_m	7.93×10^6	735.8	<0.001	significant
Cu_b	3.34×10^6	3099.2	<0.001	significant
$gapf$	7.4×10^3	0.68	0.41	
$gapb$	6.7×10^3	0.62	0.43	
gap	4.9×10^4	4.55	0.0358	significant
Fit Statistics	R^2	Adjusted R^2	Predicted R^2	Adequate Precision
	0.98	0.9786	0.9738	109.6

Table 4.17 provides information about different sources, including factors under examination, accompanied by key statistical metrics. Below are definitions and explanations of the provided metrics:

- Source: This identifies the origin of the variance, including the specific factors being investigated.
- Sum of squares: A measure quantifying variability by summing the squared deviations between the overall average and individual observed values.
- F-value: The ratio of variance between sample means to variance within the samples. It assesses whether the result is statistically significant.
- P-value (Prob>F): The probability of seeing the observed F-value if the null hypothesis is true. If the P-value is less than 0.05, it indicates that the source of variance is significant, meaning it substantially influences the response.
- R^2: A measure of the variation around the mean explained by the model. R^2 closer to 1.0 signifies a better fit.
- Adjusted R^2: A measure of the variation around the mean explained by the model, adjusted for the number of terms in the model. Adjusted R^2 should be close to 1.0.

- Predicted R^2:A gauge of the model's ability to explain variation in new data. It should not have a difference of more than 0.2 with Adjusted R^2.
- Adequate precision: A measure indicating the signal-to-noise ratio, used to compare predicted values to the average prediction error. A value exceeding 4 signifies a model with reliable adequacy for discrimination.

Based on the simulation result, a predictive model can be listed in a code equation. All the units of the factors are normalized in this coded equation. The maximum value of factors is all coded as +1, and the minimum is referred to as -1. The code equation is used to predict the response to re-creating the result and identify the relative impact of the factors by comparing the factor coefficients. The equation is:

$$Warpage = 91.23 - 284.6Cu_s - 324.13Cu_m + 613.56Cu_b + 10.34gap_f - 9.82gap_b + 25.76gap$$

The coefficient value in the equation represents how large the factor influences the result. The absolute value of the coefficient, which relates to the thickness of copper, is larger than 200, and the coefficient, which relates to the trench size, is lower than 30. It depicts that the factor of the thickness of the copper layer to the final warpage is stronger than the trench size. Figure 4.12 displays the 3D surface plot of the analysis result. Figure 4.11a presents the thickness of copper mostly controls the warpage. Additionally, the balance of the copper volume on the back and front side is important to get smaller warpage. From the function, the Cu_b value has an opposite value than Cu_s and Cu_m. The total absolute value of Cu_s and Cu_m is also smaller than Cu_b, which means in the same thickness, the influence of frontside copper is smaller than the backside. To get the smaller warpage, it is crucial to have a thicker backside copper than the front side. The relation between them is also posted in Figures 4.11c. For gap_f and gap_b, they depict the gap width between the copper layer and ceramic for the front and backside, respectively. The value of gap_f and gap_b also show opposite but similar values. It means the influence of gap_f and gap_b are almost similar. Figure 4.11b depicts the relation between gap_f and gap_b. Regarding gap, its value is twice as large as that of gap_f. This observation underscores the fact that the trench situated in the middle exerts a more significant influence on the outcome compared to the side trenches.

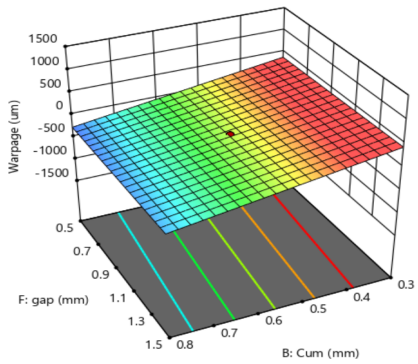

(a) The 3D Surface plot of the relation between Copper thickness and gap

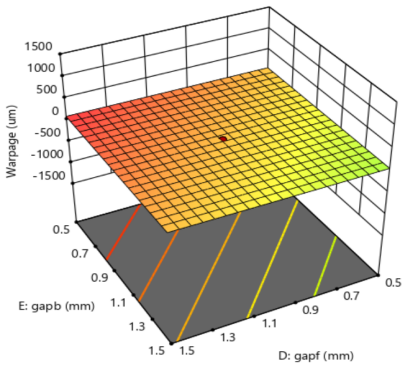

(b) The 3D Surface plot of the relation between frontside gap and back side gap

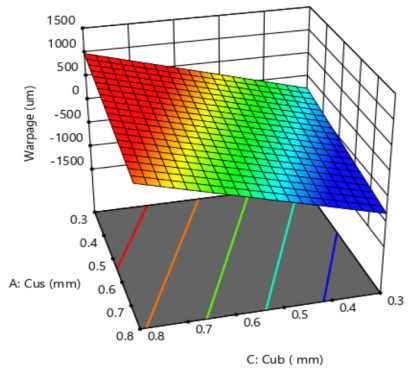

(c) The 3D Surface plot of the relation between the front and back side copper thickness

Figure 4.11: Exploring the 3D surface plot of factor relationships

4.7. Optimal structure design

Based on the factor analysis discussion, the dimensions of the three-pad structure design before and after optimization are outlined in Table 4.18. These dimensions were derived from numerical optimization via RSM analysis results. Notably, within the optimal configuration, the values of Cu_s and Cu_m surpass that of Cu_b in a concerted effort to balance warpage, as deduced from the analysis. Furthermore, by adjusting the values of gap_f, gap_b, and gap, the warpage is influenced to attain the desired optimal outcome. The optimal result is 26.1 μm, presented in Figure 4.12b. Compared with the warpage result before optimization, which is 103.6 μm, shown in Figure 4.12a, it reduces 74.8 % of the warpage.

Table 4.18: The optimal dimension value of three-pad structure

Factor	$Cu_s[mm]$	$Cu_m[mm]$	$Cu_b[mm]$	$gap_f[mm]$	$gap_b[mm]$	$gap[mm]$	$Warpage[\mu m]$
Before	0.8	0.8	0.8	1.5	1.5	1.5	103.6
After	0.8	0.8	0.74	1.5	1.5	0.5	26.1

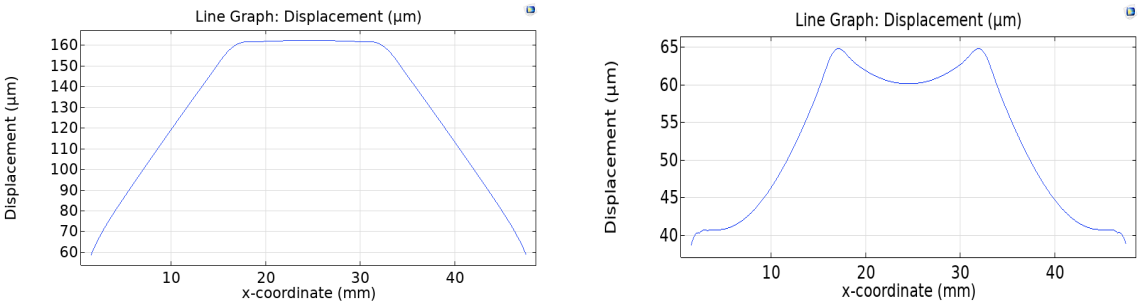

(a) Simulation warpage result of the three-pad structure before optimization

(b) Simulation warpage result of the three-pad structure after optimization

Figure 4.12: Simulation warpage result of the three-pad structure after optimization

4.8. Chapter summary

In the chapter, the outcomes of FEM simulations consistently mirror the variations in warpage observed in experimental results across diverse manufacturing process setups. The process of simulating the 3D AMB substrate is established, including the boundary conditions. A comparison of warpage changes before and after subjecting the structure to a 280 °C annealing process is conducted. It reveals the warpage values, increasing from 62.8 µm to 263.1 µm (a growth of 418.7%) in simulation and from 66.7 µm to 286.3 µm (an increase of 429%) in the experiment. It presents the harmony between simulation and experimental outcome, which verified the authenticity of the FEM model. Furthermore, the consistently increasing trends in warpage change, progressing from 140 °C to 280 °C, along with stable warpage observed during three successive annealing cycles in simulation and experimentation. It indicates warpage change is influenced by temperature value and dominantly by the first annealing cycle. Additionally, through the RSM analysis of the three-pad pattern design, the equilibrium of residual copper volume is pointed out as the crucial factor influencing warpage. Remarkably, the optimization of the three-pad structural configuration demonstrates a reduction of 74.8% in warpage.

5

Effect of Subtractive and Additive Process on Warpage

5.1. Chapter introduction

In the RSM analysis, the copper residual volume influenced the final warpage significantly. As a result, in the chapter, the new substrate structures, based on the pattern of sample FRT, are designed to analyze the effect of subtractive and additive structures. By doing additional manufacturing process experiments accompanied by FEM simulation, the relationship between the residual metal volume and warpage will be discussed.

5.2. Subtractive copper pattern design and manufacturing

In the RSM analysis result, the residual copper volume for both the front and back sides was a critical influence factor of the warpage. In the sample FRT, the backside residual copper volume is more than the front side. As a result, the subtractive pattern on the backside copper layer is designed to analyze the correlation.

The pattern design initiative began with a basic rectangular ring structure, chosen to simplify and facilitate dimensional analysis by adjusting the width and length parameters while also considering processing convenience. Four distinct pattern designs were implemented on the backside copper layer, as illustrated in Figure 5.1, providing a schematic representation of the design.

Design S1, S2, and S3 have the same outer rectangle dimension of 35 mm $\times$ 34.4 mm. Design S1 features a small rectangle ring with a trench width of 1.5 mm and a thickness of 0.4 mm, as Figure 5.1a shows. Design S2 showcases a medium rectangle ring with a trench width of 3mm and a thickness of 0.4 mm, as Figure 5.1b shows. Design S3 involves a larger rectangle ring with trenches widths of 4.4 mm and 5 mm and a thickness of 0.4 mm, as Figure 5.1c shows. Design S4 presents removing the entire surface of the backside copper with 0.11 mm, as Figure 5.1d shows. The aim of comparing designs S1,

S2, and S3, which remove the same thickness of copper trench but with different ring sizes, is to observe the effect of residual copper volume. On the other hand, designs S3 and S4, which all remove the same amount of copper from the backside, will be used to examine the impact of patterns.

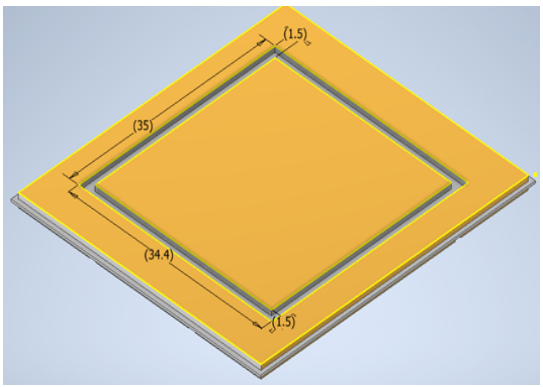

(a) Schematic of design S1 pattern on back-side copper layer

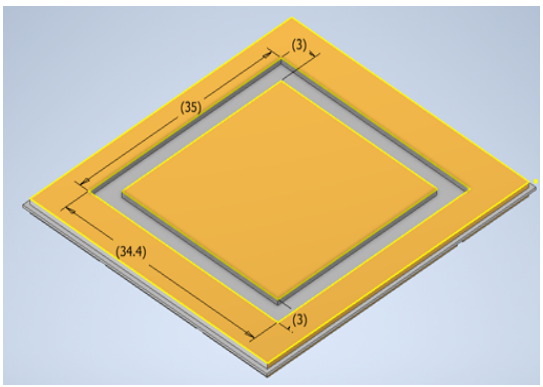

(b) Schematic of design S2 pattern on back-side copper layer

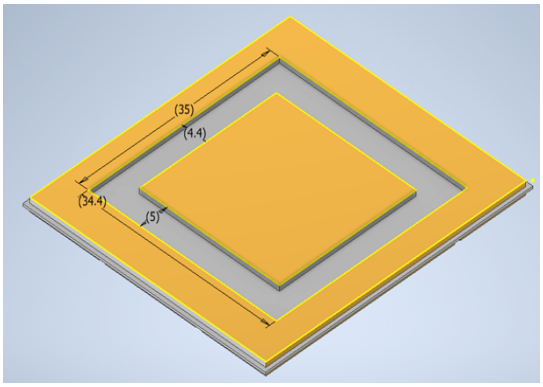

(c) Schematic of design S3 pattern on back-side copper layer

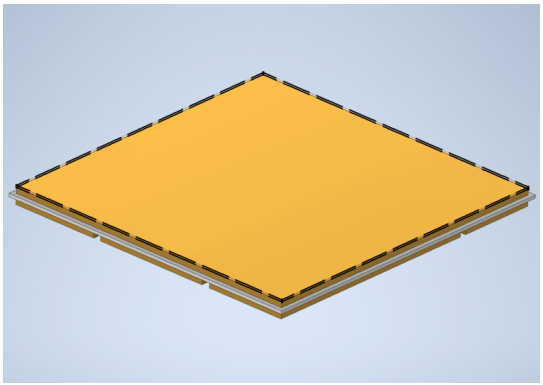

(d) Schematic of design S4 pattern on back-side copper layer

Figure 5.1: Schematic of pattern design on backside copper layer

The chosen manufacturing process for shaping a workpiece is subtractive, which involves removing material to achieve the desired shape. It is accomplished through various methods, such as cutting, drilling, and grinding. Two methods emerge when considering the options for the subtractive experiment: laser cutting and milling. The comparison of laser cutting and milling technology is shown in Table 5.1.

Laser cutting utilizes a high-powered laser beam to precisely cut through or engrave materials. The Precision Mechanical Engineering Lab employed laser cutting equipment with 15 W power and an ultraviolet wavelength of 355 nm. Copper is a highly reflective metallic material across most wavelengths. A higher absorptivity implies that the material efficiently absorbs the laser energy, leading to increased surface temperature and facilitating the laser ablation process. This phenomenon is demonstrated in Figure 5.2, which illustrates copper's absorptivity across various wavelengths. It depicts that copper reflects over 55 % of laser at 532 nm, and copper's absorptivity increases as the laser's wavelength decreases. Consequently, the ultraviolet wavelength of 355 nm was chosen for the copper laser cutting process.

Table 5.1: Comparison of subtractive manufacturing technology

Manufacturing process	Laser	Milling
Type	OPTEC	Fehlmann
Location	PME	DEMO
Speed	Slow	Fast
Accuracy	Medium	High
Manufacturing Process Picture	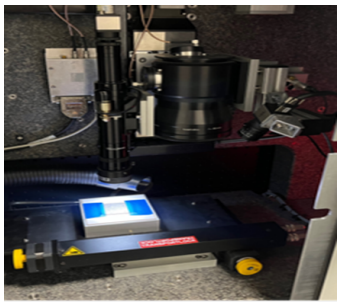	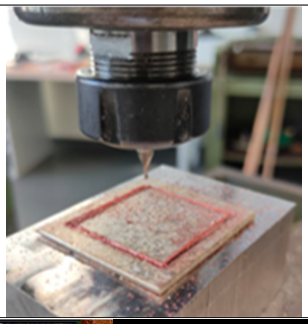
Result	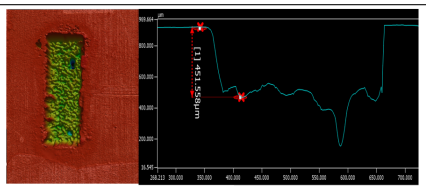	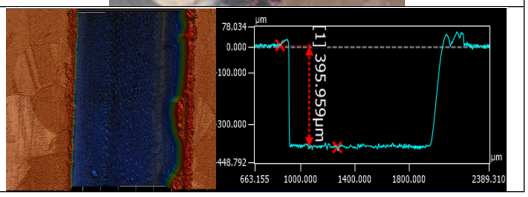

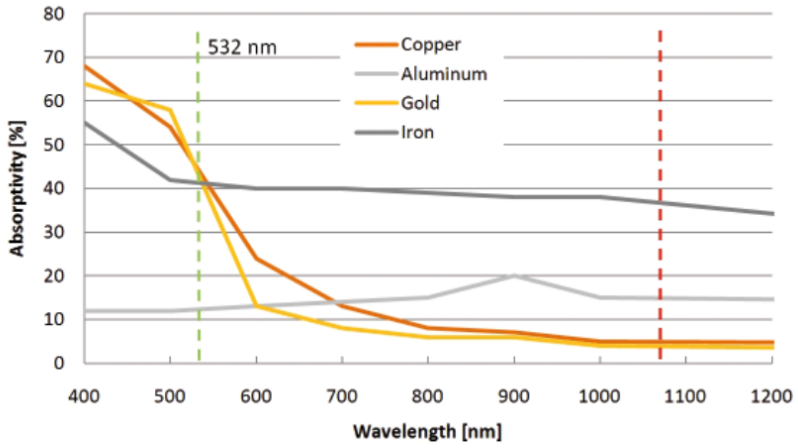

Figure 5.2: Absorptivity of different metal groups with the frequency wavelength [40]

However, due to the low power and the deep-wide trench structure from the design, laser cutting proved to be time-consuming and resulted in noticeable slope walls within the trench, as indicated in Table 5.1. Consequently, the preferred technology for the subtractive manufacturing process is milling. Milling is a manufacturing technique that uses rotary cutters at a spinning speed of 12732 rpm and feeds 255 mm/min to remove material from workpieces. This method offers high accuracy and speed and produces a level milling surface. Therefore, milling technology was adopted for the subsequent subtractive manufacturing procedures. Four designs were presented in Figure 5.1, and as part of the subsequent steps, the milling process was applied to the backside copper of sample FRT. The milling process results can be observed in Figure 5.3.

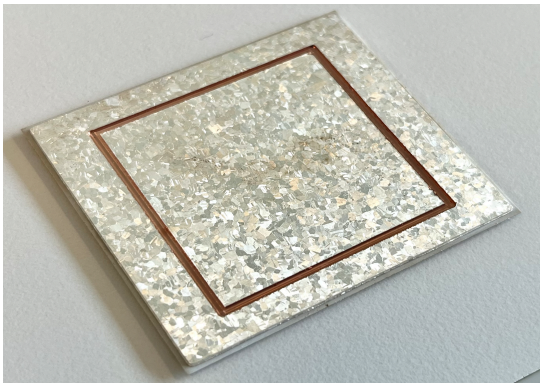

(a) Milling result of design S1 pattern on backside copper layer

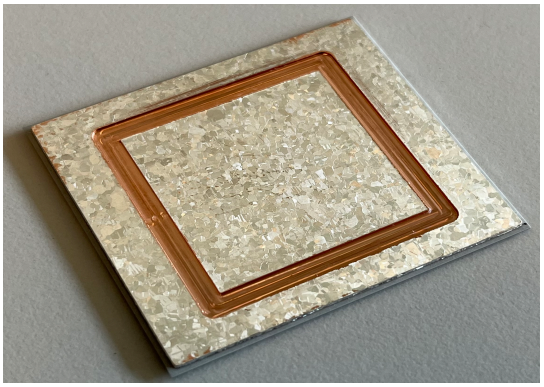

(b) Milling result design S2 pattern on backside copper layer

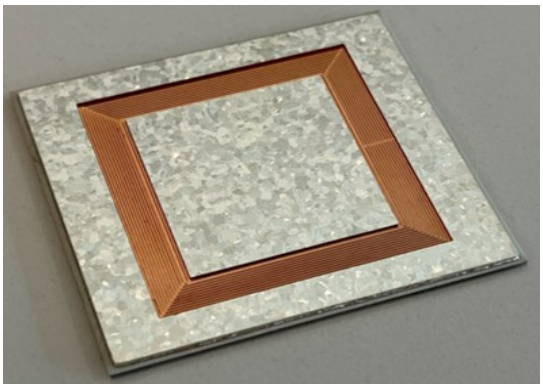

(c) Milling result design S3 pattern on backside copper layer

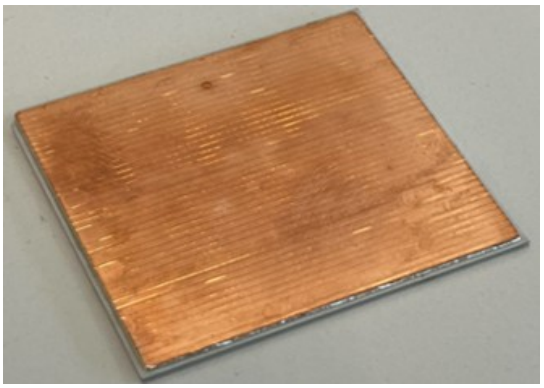

(d) Milling result design S4 pattern on backside copper layer

Figure 5.3: Milling result pattern design on backside copper layer

5.3. Warpage measurement of subtractive manufacturing

Table 5.2 provides the warpage measurement results of the sample FRT substrate before the subtractive manufacturing process, initial warpage, and after the milling and annealing process at 280 °C, final warpage. The original warpage values for the samples were relatively similar, which are 44.1 µm, 49.97 µm, 49.15 µm, 50.28 µm, and 53.29 µm, respectively. Upon comparing the milling results of the small ring (S1), medium ring (S2), and large ring (S3) on the backside, it is defined as the varied volume of copper removed from each. Specifically, the copper removed from the small ring amounts to 79.68 mm^3, from the medium ring, it is 152.16 mm^3, and from the large ring, it is 225.6 mm^3. After the annealing process, the warpage values are measured to be 116.69 µm, 96.94 µm, and 50.37 µm, respectively. It shows a significant decrease in the final warpage by comparing the substrate without the milling process, which is 149.3µm (a decrease of 222.7 %), depicted in Table 5.2.

Table 5.2: The warpage measurement of the subtractive pattern design

Sample	Sample FRT	
Design	Original	S1
Action	No milling	Small Ring
Initial Warpage	44.1 µm	49.97 µm
Final Warpage	149.3 µm	116.69 µm
Changing rate	324.7 %	234 %
Final Warpage Result	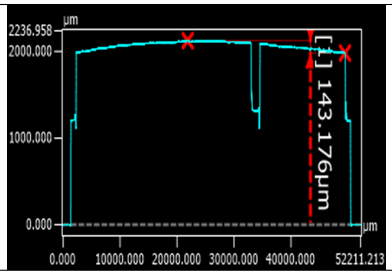	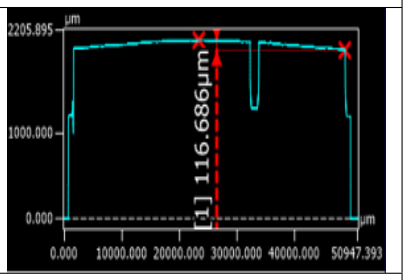
Sample	Sample FRT	
Design	S2	S3
Action	Medium Ring	Large Ring
Initial Warpage	50.28 µm	49.15 µm
Final Warpage	96.94 µm	50.37 µm
Changing rate	193 %	102 %
Final Warpage Result	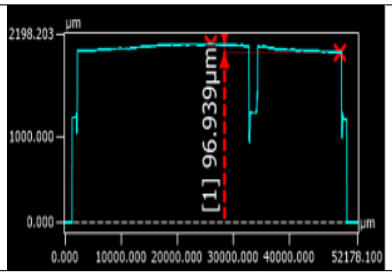	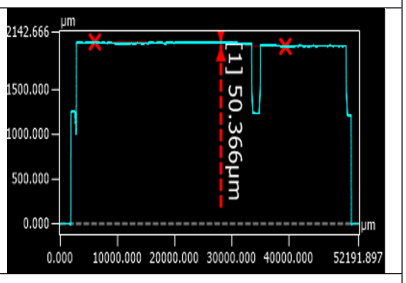
Sample	Sample FRT	
Design	S4	
Action	Whole surface	
Initial Warpage	53.29 µm	
Final Warpage	77.88 µm	
Changing rate	146 %	
Final Warpage Result	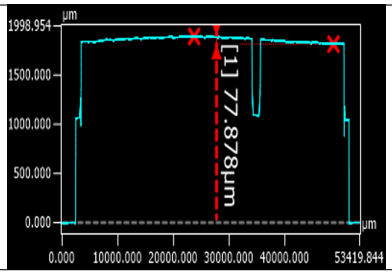	

These results also demonstrate a relationship between the residual copper volume and the warpage of the substrate. A more balanced copper volume on both sides of the substrate corresponds to a minor

final warpage. To further examine the impact of pattern influence on the warpage, design S3 and S4 are analyzed. These designs removed a similar amount of copper, approximately 225.6 mm^3 and 226.195 mm^3, respectively. The final warpage measurements for design S3 and S4 are 50.4 µm and 77.9 µm, respectively. It shows the warpage reduction affected by the subtractive pattern design and the extra stress added to the substrate. The cutting tool cut the substrate with a spinning sharp blade during the milling experiment. The cutting tool's extra stress on the surface and the heat generation during the milling influence the final warpage. Design S4 has a larger area that needs to be cut out by milling compared to design S3. As a result, it presents a more significant warpage value. The comparison of the relationship between final warpage and Copper milling volume is shown in Figure 5.4.

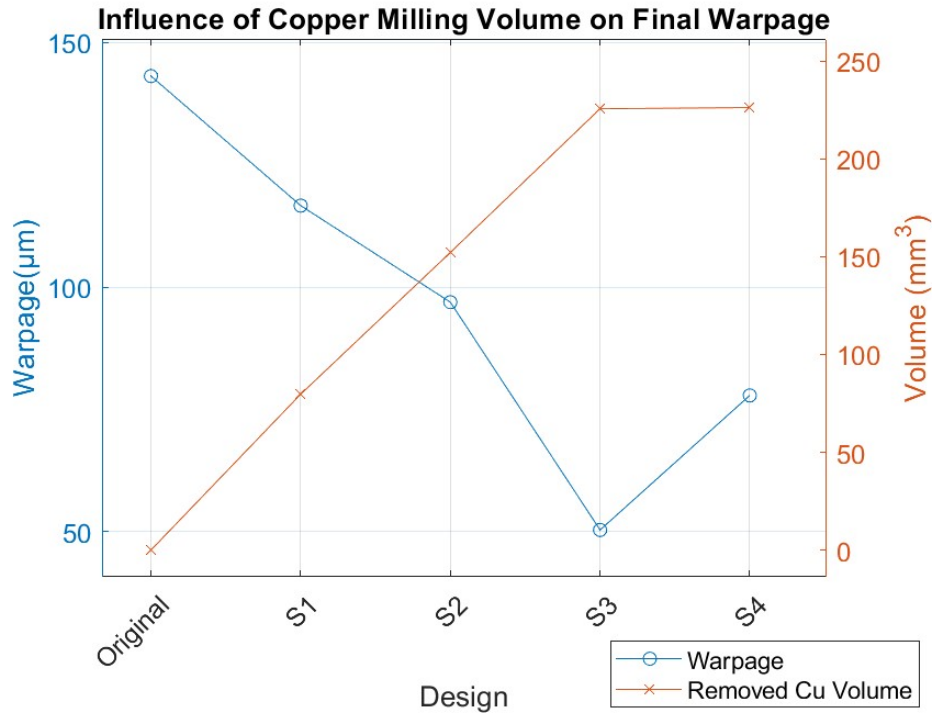

Figure 5.4: The relationship between final warpage and copper milling volume

5.4. FEM simulation of subtractive copper pattern

Following the subtractive pattern design in section 5.2, the FEM simulation was also conducted for the new design. The simulation began with the cooling process from 800 °C to 20 °C to replicate the first step of AMB substrate manufacturing. Subsequently, a specific part of the upper copper layer was deactivated to simulate the etching procedure. Following this, the constraints on all four sides were removed to model the segmentation process. Additionally, the milling-out pattern on the backside copper, designed in section 5.2, was deactivated. Finally, the annealing process was simulated, with the temperature first elevated to 280 °C and then gradually cooled down to 20 °C to complete the simulation.

Table 5.3: Warpage simulation result of subtractive pattern design

Sample	Sample FRT	
Design	Original	S1
Cu removed	0	79.68 mm^3
Final warpage	116.5 µm	47.7 µm
Simulation result	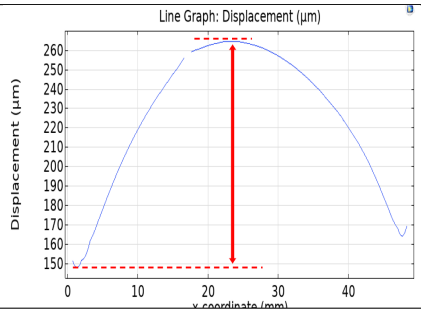	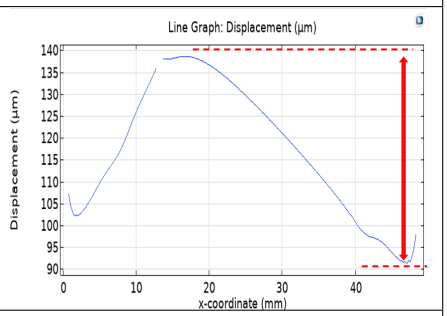
Design	S2	S3
Cu removed	152.16 mm^3	225.6 mm^3
Final warpage	23.8 µm	15.6 µm
Simulation result	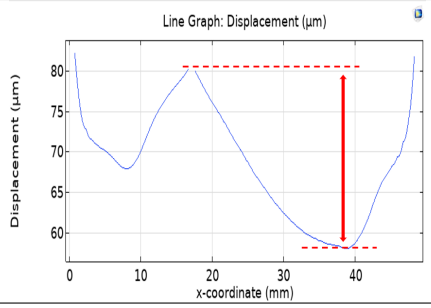	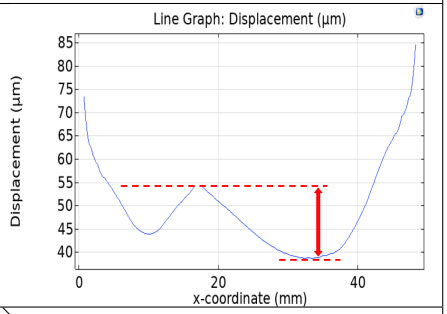
Design	S4	
Cu removed	226.2 mm^3	
Final warpage	-53.3 µm	
Simulation result	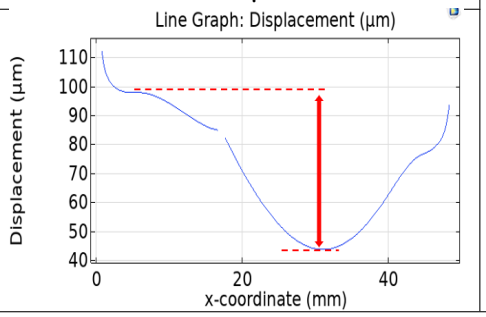	

Table 5.3 shows the simulation result for four different designs. The value is extracted from the middle line on the front side of the substrate. The value of the final warpage represents the substrate's value after the subtractive manufacturing process and undergoing the annealing process. The copper removed volume on the back-side copper layer for four pattern designs from S1 to S4 are 79.68 mm^3, 152.16 mm^3, 225.6 mm^3, and 226.2 mm^3, respectively. The final warpage for four pattern designs from S1 to S4 is 47.7 µm, 23.8 µm, 15.6 µm, and -53.3 µm, respectively. In the simulation result, the curvature is bending upwards on two sides of the substrate and gets more serious when the copper removed volume increases, and also, the warpage value range is smaller. It started affecting the temperature change in

the first step. Due to the large temperature difference, the thick copper layer shrinkage and generate large internal stress, which makes the numerical calculation error. Since it all primarily occurs at the edge of the result, they have been omitted from the warpage calculation. The calculation is performed between the red dashed lines, as indicated in Table 5.3, to minimize the impact of errors and ensure a more accurate analysis.

The original final warpage without a subtractive pattern is 116.5 μm. Compared with the original substrate's final warpage, removing an amount of copper on the back-side substrate has decreased the warpage based on the result of design S1, S2, and S3. Design S3 and S4 removed a similar amount of copper volume. However, the warpage result significantly differs due to the change in stress distribution.

The simulation's final warpage values exhibit a decreasing trend from design S1 to S3. This is considering that the volume of copper removed from the backside of the substrate increases in these designs. This phenomenon underscores the impact of residual copper volume, particularly on the backside copper, on the warpage outcome. The key insight is that a larger volume of copper removal within a similar pattern configuration correlates with a diminished final warpage result. Upon comparing design S3 and S4, where the removed copper volumes are nearly identical, it becomes evident that the pattern's configuration plays a significant role. Design S4 yields a more substantial reduction in warpage. The rationale behind this observation lies in the imbalance of copper thickness across the substrate's surface. In the case of design S4, the unbalanced copper thickness distribution triggers pronounced plastic deformation to accumulate in areas covered by the front-side copper. This accumulation, in turn, exerts a discernible influence on the ultimate warpage deformation.

5.5. Additive structure design and manufacturing

Based on the RSM analysis result, the balancing of the copper volume of both sides of the AMB substrate is a critical factor in reducing warpage. Subsection 5.3 used the milling technology to reduce the copper volume on the backside layer to reduce the warpage. As a result, the additive structure on the front-side copper layer is also considered helpful in copper volume balancing. Instead of traditional manufacturing processes, using attachment paste to establish a strong connection between different structures, the direct printing structure, without any attachment material, which impacts heat dissipation and electrical signal transmission between the substrate and the structure, is the target of the design. 3D metal printing technology was adopted to finish the additive manufacturing process to construct the three-dimensional object layer by layer. Due to the limitation of 3D metal printing on the copper substrate, the structure of the design starts from a simple and functional structure. In structure design A1, several 3 mm height pillars with different diameters of 1.5 mm, 2.5 mm, and 3 mm are shown in Figure 5.5. The pillars can not only be the metal volume balance but also can be the interconnect in the future of substrate design.

Figure 5.5: 3D printing structure design A1

To construct the design shown in Figure 5.5, the 3D SLM Printing technology is adopted for manufacturing. SLM technology utilizes a high-power laser to melt laser powder layer by layer, creating the desired structure. For design A1, the 3D printing laser equipment, LASERTEC 30 SLM in DEMO, was requested to manufacture the structure. It used a ytterbium fiber laser with 1070 nm wavelength to build the structure by Ti_6Al_4V material, a titanium and aluminum alloy, melting at 1640 °C. During the manufacturing, the equipment built the 50 µm layer, repeating layer by layer to construct the structure. Table 5.4 displays detailed information on the LASERTEC 30 SLM equipment.

Table 5.4: Additive manufacturing equipment

Equipment	LASERTEC 30 SLM Gen2
Location	DEMO
Material	Ti_6Al_4V
Laser type	Ytterbium laser
Laser velocity	0.742m/s
Laser power	219Watt
Equipment Picture	

The printing process was applied to the frontside copper of sample FRT. The results of the 3D printing results can be observed in Figure 5.6. The warpage measurement results will be discussed in

the following subsection.

Figure 5.6: 3D Printing result of design A1 pattern on sample FRT

5.6. Warpage measurement of additive manufacturing

Adopting the Keyence microscope can measure the warpage before 3D printing and after the printing and annealing. Table 5.5 represents the measurement results for the original substrate and the 3D printing. For the original substrate and design A1, respectively, the initial warpage of sample FRT is 44.1 µm and 44.2 µm, the final warpage is 116.5 µm and 98.13 µm, and the warpage changing rate is 324.7 % and 222 %. Compared with the annealing result, the experimental result of 3D printing significantly influences the warpage reduction.

Table 5.5: The warpage measurement of additive structure design

Sample	Sample FRT	
Design	Original	A1
Initial warpage	44.1 µm	44.2 µm
Final warpage	143.2 µm	98.1 µm
Changing rate	324.7 %	222%
Initial warpage result	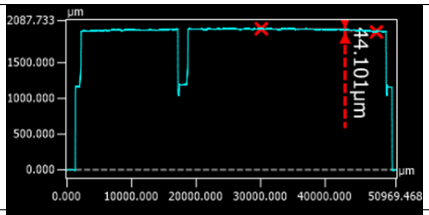	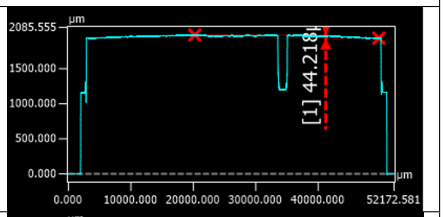
Final warpage result	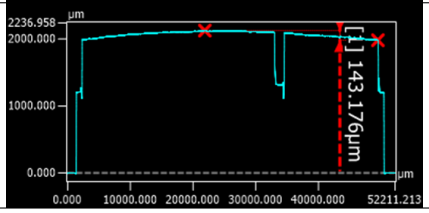	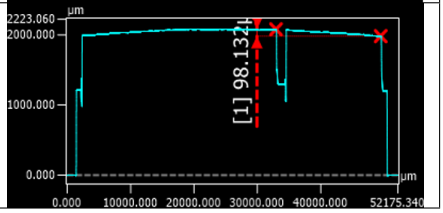

5.7. FEM simulation of additive structure

Building upon the subtractive pattern design illustrated in Figure 5.5, the FEM simulation was executed for the updated configuration. The simulation initiated the cooling process, starting from 800°C and reaching 20°C. Then, a specific region of the upper copper layer was deactivated to emulate the etching procedure. This was followed by removing constraints on all four sides to replicate the segmentation process. Moreover, the printing structures on the front-side copper were activated. Finally, the simulation accounted for the annealing process, involving the temperature increase to 280 °C and cooling to 20 °C, concluding the simulation.

Table 5.6 collects the simulation result of the original FRT substrate and 3D printing structure design. The final warpage result of the original and 3D printing is 116.5 µm and 48.9 µm, and the warpage change is 356.3 % and 158.7 %. Compared to the two results, the additive structure effectively reduces the final warpage result.

Table 5.6: Warpage simulation result of additive structure pattern design

Sample	Sample FRT	
Design	Original	A1
Final warpage	116.5 µm	48.9 µm
Warpage change	356.3%	158.7%
Final warpage simulation result	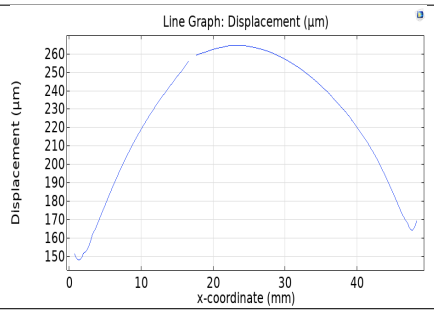	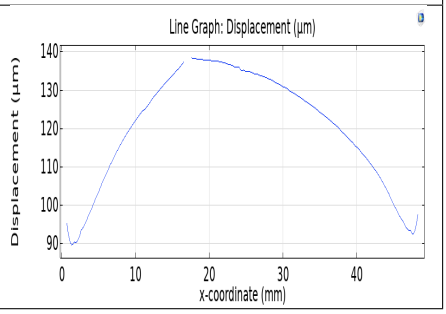

5.8. Comparison of simulation and experimental results

The FEM simulation and the additional manufacturing process experiment results are collected to compare.

1. Comparison of subtractive pattern result

   Table 5.7 compiles the warpage results obtained from both subtractive pattern FEM simulations and experimental measurements. For design S1, S2, and S3, both simulation and experimental outcomes corroborate the trend of warpage reduction as the volume of removed copper increases. However, it is evident that the experimentally measured warpage values consistently surpass their simulation results.

   This difference between experimental and simulation results can be attributed to the milling process employed in the experiments. The milling process introduces additional factors, such as heat generation and external stress, onto the surface, which can amplify the warpage effects. This

effect becomes more pronounced, particularly in the experimental result of Design S4. However, the simulation's attempt to emulate the milling process involved only the deactivation of the rectangle ring portion without accounting for the added stresses or constraints associated with clamping and other milling dynamics. Consequently, this disparity is responsible for the observed variations between the simulation and experiment results.

Table 5.7: The warpage in subtractive structure comparison

Design	S1	S2	S3	S4
Cu Removed Volume	79.68 mm^3	152.16 mm^3	225.6 mm^3	226.2 mm^3
Simulation	47.7 µm	23.8µm	15.6 µm	-53.3 µm
Experiment	116.7 µm	96.9 µm	50.4 µm	77.9 µm

2. Comparison of additive structure result

   Table 5.8 compares simulation and experimental outcomes for the additive structure. Both results demonstrate a reduction in warpage, with a notable difference between the simulation and experimental values. Specifically, the simulation results exhibit a more significant reduction in warpage compared to the experimental outcomes.

   This discrepancy can be attributed to the differences in the additive manufacturing process itself. During the 3D printing experiment, the ytterbium laser melted the Ti_6Al_4V material, whose melting temperature was 1640 °C. This localized melting introduced substantial heat generation within the specific region where the structure was built. This heat was dissipated through the copper's high thermal conductivity. However, the simulation did not account for the heat generated by the laser printing process.

   The absence of this crucial heat generation mechanism in the simulation is a primary factor leading to the observed error between the simulation and experimental results. As a result, the simulation's warpage reduction prediction appears to exceed the experimental reality.

Table 5.8: The warpage in additive structure comparison

Sample	Sample FRT	
Data type	Simulation	Experiment
Initial warpage	30.8 µm	44.2 µm
Final warpage	48.9 µm	98.13 µm
Warpage Change ($\frac{Finalwarpage}{Initialwarpage} \times 100\%$)	158.7 %	222%

5.9. Chapter summary

This chapter includes evaluating the subtractive and additive structure designs through simulation and experimentation, employing milling and 3D laser printing technologies. The subtractive experiment yields a correlation between the volume of removed copper and the resulting final warpage, achieving

a reduction of 222.7 % compared to the original warpage magnitude. The simulation results reinforce this correlation, confirming that a larger removed copper volume corresponds to a smaller warpage.

In the additive structure approach, the results prove the additional metal structure on the front side copper layer can reduce warpage. The experimental outcome showcases a substantial 102.7 % reduction in warpage through 3D printing technology. Similarly, the simulation results indicate a decrease of 197.6 % in warpage. The difference can be attributed to the simulation ignoring the substantial heat generated at the localized printed region.

Both the subtractive and additive structures, validated through simulation and experimentation, consistently demonstrate substantial reductions in warpage. These findings underscore the significance of balancing residual copper volume and importing the new manufacturing method inside the power module substrate manufacturing.

6

Effect of Sintering Process on Warpage

6.1. Chapter introduction

The purpose of this chapter is to provide an introduction to the sintering technology and equipment employed in the conducted sintering experiment. Furthermore, the chapter outlines a step-by-step demonstration of the sintering procedures, highlighting the specific temperature and pressure settings utilized. The warpage resulting from the sintering process is measured and apposed against the warpage in the annealing process for comparative analysis. A FEM simulation model of the sintering process is also created and compared to experimental results.

6.2. Sintering technology

The sintering process serves as a die attachment technique to establish a robust connection between a die and a substrate. Its primary goals encompass attaining elevated thermal conductivity, compatibility with high-temperature settings, and creating a durable bonding link. This process entails the application of heat and pressure to the die and substrate, compacting the sintering paste to form a dense bulk without reaching the melting temperature. The complete sintering procedure involves distinct stages: material preparation, application of sintering paste, the core sintering process, and the subsequent cooling phase. Each of these stages will be explored in greater depth within this chapter.

6.2.1. Equipment of sintering process

The Die Bonder T-3000-PRO, illustrated in Figure 4.7, was employed within the EKL MEMS lab to facilitate the sintering procedure. This equipment executed individual die bonding tasks, commencing from the pick and place operation and extending to pressure application for die attachment. For the heating component of the sintering process, the Die Bonder T-3000-PRO was integrated with a hot plate. Furthermore, it incorporated nitrogen gas flushing to counteract oxidation during the process. This

integrated configuration guaranteed practical die attachment while upholding meticulously controlled oxidation conditions.

6.2.2. Procedures of sintering process

The sintering process comprises several key stages, including substrate preparation, die pick and placement, the application of pressure, as well as heating and subsequent cooling sessions. A comprehensive overview of the sintering process procedures is depicted in Figure 6.1, which will be detailed in the ensuing sections.

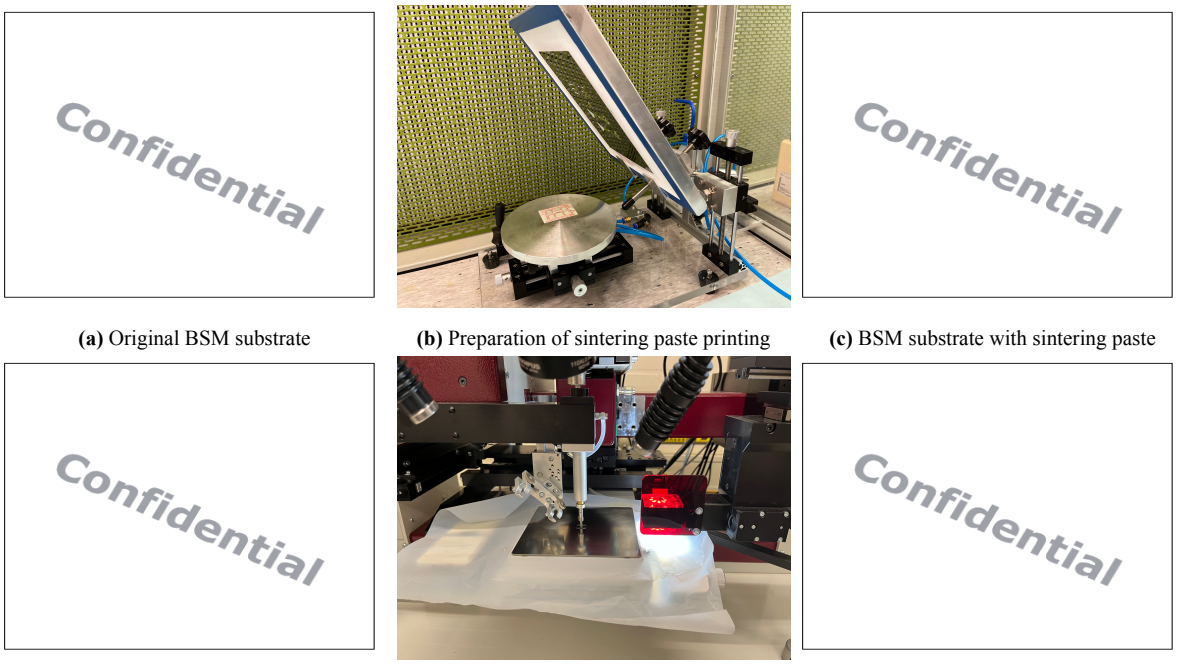

(a) Original BSM substrate

(b) Preparation of sintering paste printing

(c) BSM substrate with sintering paste

(d) Die placing on BSM substrate

(e) Pressure and heat in sintering process

(f) Sintering result of BSM substrate

Figure 6.1: Sintering process procedures

1. Sintering paste application

   The sintering paste is the adhesive layer that establishes the connection between the die and the substrate. Figure 6.1a illustrates the BSM substrate before the application of sintering paste. To precisely regulate the thickness and dimensions of the sintering paste, a stencil plate featuring a 1cm x 1cm cavity was utilized as a printing template, as shown in Figure 6.1b. The outcome, depicted in Figure 6.1c, showcases the BSM substrate with the applied copper sintering paste. Subsequently, to facilitate the drying process of the sintering paste, the substrate was placed in a 110°C oven for 5 minutes.

2. Die placement

   The MOSFET chip was carefully positioned onto the copper paste layer on the preheated hot plate. Utilizing the pick and place functionality, the die was precisely situated in its designated location, as exemplified in Figure 6.1d.

3. Sintering process with pressure and heat applying

   A combination of heating and pressure was employed to establish a robust connection between the die and substrate. A steel plate, along with a covering of PTFE Teflon paper, was utilized to prevent oxidation during this phase shown in Figure 6.1e. Nitrogen gas, comprising 3% hydrogen at a flow rate of 5 L/min, was introduced into the chamber throughout the heating and subsequent cooling stages. Further details regarding the temperature and pressure settings can be found in Figure 6.2.

4. Cooling down and result presentation

   Subsequently, the hot plate and the substrate were gradually cooled to room temperature, marking the completion of the sintering process, as depicted in Figure 6.1f.

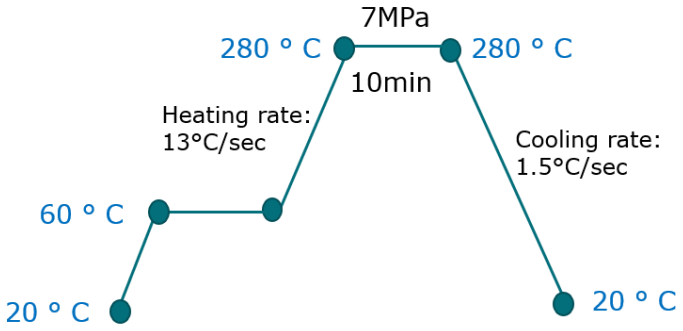

Figure 6.2: Pressure and temperature setting during the sintering process

Figure 6.3 shows the sintering outcomes for the sample FRT. It is apparent that the color of the copper layer closely resembles that of the original substrate, highlighting the effectiveness of utilizing a Teflon paper cover in conjunction with Nitrogen and Hydrogen gas to prevent oxidation.

Figure 6.3: Sintering result of BSM substrate

6.3. Warpage measurement of sintering process

Table 6.1 compiles the warpage measurement outcomes of sample BSM in the annealing process and sintering process. The final warpage measurements result of annealing is 286.25 µm, and the sintering result is 279.4 µm. Notably, in the case of the BSM substrate, the final warpage, 279.4 µm, was already subtracted thickness of the die and sintering paste, which amount to 207.4 µm and 40 µm, respectively. The ultimate warpage outcomes for both cases exhibit similarity, differing by only 6.9 µm, underscoring the impact of the pressure applied to the chip during the process and the presence of the die and copper paste. As a result, the principal determinant driving warpage variation within the same substrate is the annealing temperature.

Table 6.1: The warpage measurement of sintering substrate

Sample	Sample BSM	
Action	Annealing	Sintering
Final warpage	286.3 µm	279.4 µm
Final warpage result	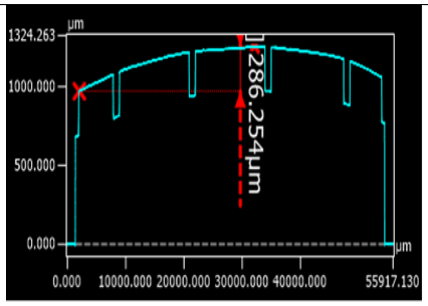	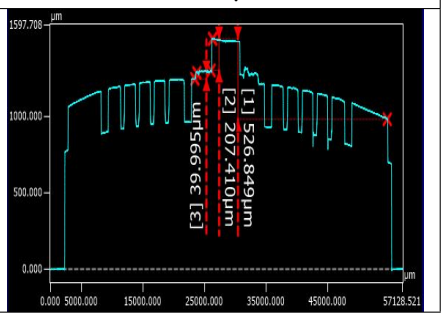

6.4. FEM simulation of sintering process

The FEM model of the sintering process was also simulated. Figure 6.4 illustrates the sintering configuration of sample BSM. The brown-colored rectangle, measuring 3.5 mm × 3.5 mm × 0.04 mm, on the substrate signifies the copper sintering paste. On top of the sintering paste is the die with dimensions of 2.29 mm × 2.29 mm × 0.2 mm. A crucial aspect of the sintering process involves the application of pressure to facilitate the bonding of the chip and substrate. To replicate the process, the right rigid domain measuring 3.5 mm × 3.5 mm × 0.2 mm was positioned under the backside copper layer, functioning as a support table to support the applied pressure during chip attachment. The interface between the rigid support and the bottom surface of the substrate was described as a contact pair. The contact pair emulated the interaction between distinct components within the system that came into direct physical contact. The material properties of the copper paste and the die are outlined in Table 6.2.

Figure 6.4: Schematic of sintering BSM substrate

Table 6.2: Material properties of copper paste and die in simulation model [41] [42]

Material	Copper paste	Die
Young's modulus (GPa)	72.5	450
Poisson's ratio	0.35	0.17
CTE (K^{-1})	17×10^{-6}	3.5×10^{-6}
Yield stress (MPa)	330	
Tangent modulus (GPa)	13.7	

The simulation model was initiated by simulating the cooling process, starting from 800 °C and gradually reaching 20 °C. Subsequently, deactivated the specific to mimic the etching process, then, followed by the removal of constraints on all four sides to simulate the segmentation process. The existing sintering paste and die were then activated to replicate the application of sintering paste and die placement procedures. Furthermore, the temperature was elevated to 280 °C, and a pressure of 7 MPa was applied to the chip to emulate the sintering process. The simulation concluded with a cooling process back to 20 °C.

Table 6.3 presents the final warpage values for sample BSM obtained from the 2D and 3D simulations of the annealing and sintering processes, resulting in 240.2 µm and 218.4 µm, respectively. The calculation for the sintering result involved subtracting the lowest height from the highest height in the figure while also subtracting the thickness of the die and sintering paste, which amounts to 200 µm and 40 µm, respectively. The annealing and sintering results exhibit similarities, with a difference of 21.8 µm. It depicts that the additional pressure applied to the surface during sintering still has a minor influence on the simulation model. Furthermore, the contact pair included the penalty method in the simulation system, facilitated the analysis process, and ensured convergence. However, the penalty method enforced constraints or conditions that introduced some numerical instability. Consequently, this led to errors in the simulation outcomes, as shown in the observed effects between sintering and annealing results.

Table 6.3: The warpage simulation result of sintering substrate

Sample	Sample BSM	
Action	Annealing	Sintering
Final Warpage	240.2 µm	218.4 µm
2D warpage result	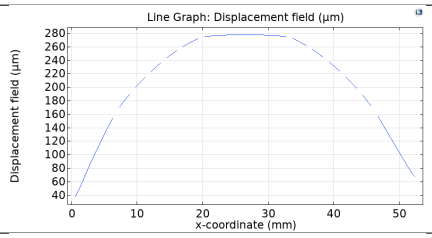	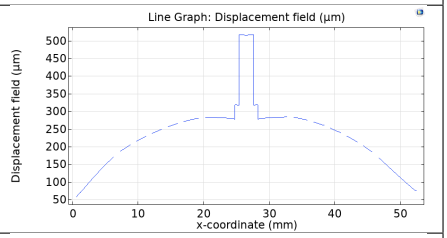
3D Warpage Result		

6.5. Comparison of simulation and experimental results

Table 6.4 compares the simulation and experimental results for both the annealing and sintering processes. From the comparison, the warpage values observed during the annealing process are slightly larger in magnitude compared to those during the sintering process in both simulation and experiment. This difference can be attributed to the additional pressure applied during the sintering process, which slightly impacts the warpage outcome. However, all recorded values exceeded 200 µm, and the process temperature happened at 280 °C, indicating that the most significant factor influencing warpage is the ambient temperature during the annealing and sintering procedures.

Table 6.4 compared the results of annealing and sintering in simulation and experiment. Simulation and experiment results show that the warpage value of the annealing process is larger than the sintering process. It shows the added pressure, which slightly influences the warpage result. However, all the values are more significant than 200 µm, and the annealing and sintering temperature happen at 280 °C, indicating that the most significant factor influencing the warpage is the ambient temperature during the annealing and sintering procedures.

Moreover, the table reveals that simulation values consistently appear lower than their experimental counterparts. This can be attributed to the rigid support, which had the exact dimensions as the copper paste and was situated beneath the substrate in the simulation model. This rigid support constrained the convex shape of the warpage deformation. The 2D warpage result provided in Table 6.3 displays a relatively flat region in the middle of the curve. Consequently, the simulation values are lower than the corresponding experimental results.

Table 6.4: The warpage simulation result of sintering substrate

Sample	Sample BSM	
Action	Simulation	Experiment
Annealing	240.2 μm	286.3 μm
Sintering	218.4 μm	279.4μm

6.6. Chapter summary

This chapter delved into an in-depth exploration and demonstration of the sintering manufacturing process and its associated steps. It happened at 280 °C with 7 MPa pressure for 10 minutes. The final experiment warpage value is 279.4 μm, signifying a 6.9 μm disparity in comparison to the result of the annealing process. In parallel, the simulation final sintering process warpage is 218.4 μm, revealing a 21.8 μm difference from the annealing process outcome. It acknowledges that the numerical analysis of the contact pair settings influences the simulation outcome. However, it also indicates that the pressure applied affects the overall outcome. As a result, the main influencing factor contributing to warpage throughout the manufacturing process is the control of the annealing temperature.

7

Summary and Conclusion

7.1. Project summary

Driven by the rapid development of power electronics, the reliability performance of power modules becomes a primary concern to ensure performance. In terms of power module substrates, the stacking of multiple copper and ceramic layers with significant CTE differences can lead to warpage issues during manufacturing. Warpage, caused by thermo-mechanical stress at the interface, poses a risk of cracks and delamination in the devices.

The literature review underscored the influence of ceramic substrate pattern design, examining it from simulation or experimental perspectives. Furthermore, the sintering process and the potential additive manufacturing process, 3D printing, were included. Nevertheless, there existed a research gap concerning a comprehensive understanding of the root causes of warpage and the crucial step of validating simulations through practical experiments.

As a result, the primary goal of this project is to comprehend the warpage phenomenon, effectively mitigate it through FEM simulation and experimentation, and ultimately optimize the manufacturing process. The project unfolded in three distinct phases: investigation of the cause of the warpage, the validation of the simulation model and experiment result, and implementation of optimization strategies.

The primary conclusions are presented below,

- **Investigation of the cause of the warpage**

    1. Warpage evolution characterization

       To have accurate warpage measurement data, various non-contact warpage measurement equipment in different labs or companies, including laser microscopes, optical microscopes, white light interferometers, and a real-time laser scanner, were thoroughly tested to measure the warpage of the received AMB substrates. The Keyence laser microscope emerged as the optimal choice among several options due to its high accuracy. The warpage values of sample BSM and FRT were defined by subtracting the highest point minus the lowest point

on the same surface as 66.7 μm and 44.1 μm, respectively. By implementing the annealing process, a 3 to 4 times difference was noticed in an AMB substrate. The further annealing process caused less warpage than the first time.

2. Material properties experiment To explain the cause of the warpage, a 2D FEM model with materials properties extracted from experiments was built up. The CTE for annealed OFC, measured across a range of 25 °C to 365 °C at a heating and cooling rate of 5 °C/min, was determined to be 16.7×10^{-6} K^{-1}. Additionally, the annealed OFC sample, with dimensions of 5 mm × 39 mm × 0.8 mm, underwent tensile testing at various environmental temperatures (20 °C, 95 °C, 170 °C, and 250 °C). The resulting yield strengths for the annealed OFC were measured at 18.8 MPa, 17.5 MPa, 17.3 MPa, and 16.3 MPa for the respective temperatures. The model's accuracy was confirmed by its alignment with experimental trends, reaffirming its validity.
3. Mechanical behavior during the manufacturing process

   The FEM simulation's mechanical analysis revealed that the elastic strain variation inside the copper layer introduced the initial warpage due to the unbalanced strain released by the front side copper etching process. The plastic strain difference inside the copper layer influenced the final warpage because the layer extended and compressed in the annealing process, introducing a non-reversible plastic strain change. After annealing, the plastic strain showed 3.5 times more significant difference than the elastic strain. Based on stress distribution, strain can be related to the moment inside the substrate. The value of the moment also presented a 3.4 times difference, which made a clear linkage between the plastic strain and warpage.

- **Validation of the simulation model and experiment result**

1. Comparison of warpage change before and after 280 °C annealing

   The simulation result of sample BSM warpage change was from 62.8 μm to 263.1 μm (418.7 %), and the experiment result was from 66.7 μm to 286.3 μm (429 %). It presented the harmony between the simulation and experimental outcome of which FEM model.
2. Comparison of warpage change at different annealing temperatures

   The simulation and experiment revealed consistently increasing trends in warpage change, progressing from 140 °C to 280 °C. Simulation results increased from 205.9 μm (327.8 %) to 244.8 μm (389.8 %), and experiment rose from 174.8 μm (282.2 %) to 287.3 μm (463 %) of sample BSM. The discrepancy could be attributed to the inaccurate material properties model.
3. Comparison of warpage at different annealing cycles

   Assessing three annealing cycles for sample BSM, simulation and experimentation values were consistent with mild warpage increment over increased thermal processes from 263.1 μm to 286.5 μm and from 286.25 μm to 307.36 μm, respectively. It indicated that substantial warpage change predominantly occurs during the first annealing cycle.

The comparison of simulation and experimental findings proved a high correspondence and validated the trustiness of the FEM model.

- **Factor analysis and optimization Work**

  1. Warpage influence factor analysis

     The influence of the thickness of the copper layer of front and backside, the trench width between different copper pads was successfully analyzed by the RSM method. It indicated that the thickness of the copper layer had 20 times more influence than trench size on both copper layers. Specifically, thinner backside copper was crucial to achieve warpage reduction. As a result, the primary factor to mitigate warpage was the balance of the residual copper volume. The optimization model results presented a 74.8 % warpage reduction by reducing the backside copper thickness and shortening the front side trench width to reach the same residual copper volume for both side layers.
  2. Subtractive copper design and technology

     The subtractive backside pattern design, with the same copper removing amount, ring structure achieved a warpage reduction of 222.7 %, and plain surface structure attained 178.7 % in experiment results. It showed residual copper volume, and the pattern significantly affected warpage reduction. The simulation outcomes echoed this relationship, affirming that more significant copper volume removal correlates with reduced warpage.
  3. Additive copper design and technology

     The pillar structure, utilizing 3D laser printing technology on the front side of the copper, delivered 102.7 % and 197.6 % warpage reduction through experimentation and simulation results. The discrepancy can be attributed to the heat generation during the 3D printing experiment, which was ignored in the simulation.
  4. Influence of sintering process on warpage

     The sintering process involved a 7 MPa pressure on the die for 10 minutes at 280 °C. Compared to the results with and without pressure, it showed a difference of 6.9 μm in experiments and 21.8 μm in simulations. It proved the main factor affecting warpage in the manufacturing process was the control of annealing temperature.

  The outcomes of both subtractive and additive technologies corroborated the findings of the RSM analysis. The manipulation of copper volume validated the warpage alleviation.

7.2. Recommendations

- Re-conduction of Tensile test: Measure the tensile test with an extensometer to ensure the acquisition of more accurate material properties.
- Investigation of internal stress: Perform experiments to inspect internal stress, providing a deeper understanding of its effects to conjunct with the simulation results.
- Investigation of variant backside pattern design: Introduce more pattern designs on the backside, such as mirroring the frontside patterns, to assess the influence on warpage outcomes.
- Exploration of additive structures: Design additional additive structures, such as hanging or heat sink structures, to investigate the relationship between surface area, volume, material type, and the impact on warpage.

- Comparative of manufacturing techniques: Implement the backside pattern manufactured in the etching process when manufacturing the front side. Analyze the influence of milling by compared with the etching methods to understand how the different manufacturing technologies affect warpage.
- Enhancement of simulation model: Refine the simulation model by introducing supplementary constraints or steps aimed at minimizing the disparities between simulation and experimental outcomes.
- Extension of manufacturing step: Explore the warpage analysis into subsequent manufacturing steps, such as clip attaching, lead-frame bonding, and molding compound ejection, to comprehensively capture the complete warpage behavior within the assembly process.

References

[1] Tingrui Gong et al. “Thermo-mechanical optimization of ceramic substrate with through ceramic vias by Taguchi-Grey method”. In: *Microelectronics Reliability* 132 (2022), p. 114535.

[2] MY Tsai et al. “Mechanical design and analysis of direct-plated-copper aluminum nitride substrates for enhancing thermal reliability”. In: *Microelectronics Reliability* 55.12 (2015), pp. 2589–2595.

[3] Yuhang Yang et al. “Automotive power module packaging: Current status and future trends”. In: *IEEE Access* 8 (2020), pp. 160126–160144.

[4] Guiqin Chang et al. “Forward design research on the warpage of baseplate for IGBT module”. In: *2022 23rd International Conference on Electronic Packaging Technology (ICEPT)*. 2022, pp. 1–5. DOI: 10.1109/ICEPT56209.2022.9873393.

[5] Allen Jose George et al. “Nonconchoidal fracture in power electronics substrates due to delamination in baseplate solder joints”. In: *2018 7th Electronic System-Integration Technology Conference (ESTC)*. IEEE. 2018, pp. 1–6.

[6] Daren Slee et al. “Introduction to printed circuit board failures”. In: *2009 IEEE Symposium on Product Compliance Engineering*. 2009, pp. 1–8. DOI: 10.1109/PSES.2009.5356012.

[7] Kazuhiko Sugiura et al. “Reliability Evaluation of SiC Power Module With Sintered Ag Die Attach and Stress-Relaxation Structure”. In: *IEEE Transactions on Components, Packaging and Manufacturing Technology* 9.4 (2019), pp. 609–615. DOI: 10.1109/TCPMT.2019.2901543.

[8] Chenjiang Yu, Cyril Buttay, and Éric Labouré. “Thermal Management and Electromagnetic Analysis for GaN Devices Packaging on DBC Substrate”. In: *IEEE Transactions on Power Electronics* 32.2 (2017), pp. 906–910. DOI: 10.1109/TPEL.2016.2585658.

[9] “Effect of high temperature cycling on both crack formation in ceramics and delamination of copper layers in silicon nitride active metal brazing substrates”. In: *Ceramics International* 43.6 (2017), pp. 5080–5088. ISSN: 0272-8842. DOI: https://doi.org/10.1016/j.ceramint.2017.01.020.

[10] M.Y. Tsai et al. “Mechanical design and analysis of direct-plated-copper aluminum nitride substrates for enhancing thermal reliability”. In: *Microelectronics Reliability* 55.12, Part A (2015), pp. 2589–2595. ISSN: 0026-2714. DOI: https://doi.org/10.1016/j.microrel.2015.08.010. URL: https://www.sciencedirect.com/science/article/pii/S0026271415301463.

[11] A. George et al. “Reliability investigation of large area solder joints in power electronics modules and its simulative representation”. In: *Microelectronics Reliability* 88-90 (2018). 29th European Symposium on Reliability of Electron Devices, Failure Physics and Analysis (ESREF 2018), pp. 762–767. ISSN: 0026-2714. DOI: https://doi.org/10.1016/j.microrel.2018.06.049. URL: https://www.sciencedirect.com/science/article/pii/S0026271418304669.

[12] J. Schulz-Harder and K. Exel. “Recent developments of direct bonded copper (DBC) substrates for power modules”. In: *Fifth International Conference onElectronic Packaging Technology Proceedings, 2003. ICEPT2003.* 2003, pp. 491–496. DOI: 10.1109/EPTC.2003.1298787.

[13] Jinling Lv et al. “AlN/Cu composite ceramic substrate fabricated using a novel TiN/AgCuTi composite brazing alloy”. In: *Journal of the European Ceramic Society* 40.15 (2020), pp. 5332–5338. ISSN: 0955-2219. DOI: https://doi.org/10.1016/j.jeurceramsoc.2020.07.060. URL: https://www.sciencedirect.com/science/article/pii/S0955221920306154.

[14] Yukun Zhang, Jinsong Zhang, and Jichun Chen. “Effect of interfacial microstructure evolution on the peeling strength and fracture of AMB Cu-metalized AlN substrate”. In: *Journal of the American Ceramic Society* 105.1 (), pp. 577–589. DOI: https://doi.org/10.1111/jace.18092. eprint: https://ceramics.onlinelibrary.wiley.com/doi/pdf/10.1111/jace.18092. URL: https://ceramics.onlinelibrary.wiley.com/doi/abs/10.1111/jace.18092.

[15] Roberto Louis Moran et al. “Reduction of IC Package Warpage through Finite Element Analysis and Direct Optimization”. In: *2019 IEEE 11th International Conference on Humanoid, Nanotechnology, Information Technology, Communication and Control, Environment, and Management (HNICEM)*. 2019, pp. 1–6. DOI: 10.1109/HNICEM48295.2019.9072881.

[16] Jürgen Schulz-Harder. “Advantages and new development of direct bonded copper substrates”. In: *Microelectronics Reliability* 43.3 (2003), pp. 359–365. ISSN: 0026-2714. DOI: https://doi.org/10.1016/S0026-2714(02)00343-8. URL: https://www.sciencedirect.com/science/article/pii/S0026271402003438.

[17] Emmanuel Arriola et al. “Evaluation of the Effects of Introducing Channels to Composite Materials to Reduce Warpage on Semiconductor Packages Due to Coefficient of Thermal Expansion Mismatch”. In: *2019 IEEE 11th International Conference on Humanoid, Nanotechnology, Information Technology, Communication and Control, Environment, and Management (HNICEM)*. 2019, pp. 1–5. DOI: 10.1109/HNICEM48295.2019.9072815.

[18] Yuci Shen, Leilei Zhang, and Xuejun Fan. “Achieving warpage-free packaging: A capped-die flip chip package design”. In: *2015 IEEE 65th Electronic Components and Technology Conference (ECTC)*. 2015, pp. 1546–1552. DOI: 10.1109/ECTC.2015.7159803.

[19] Ling Xu et al. “An optimal structural design to improve the reliability of Al2O3–DBC substrates under thermal cycling”. In: *Microelectronics Reliability* 56 (2016), pp. 101–108. ISSN: 0026-2714. DOI: https://doi.org/10.1016/j.microrel.2015.11.013. URL: https://www.sciencedirect.com/science/article/pii/S0026271415302286.

[20] Jenelyn Simbulan Rodriguez, Faiz Zuhairy Redzuan, and Raymund Nonato Jotea Concepcion. “SSDC SiC Mosfet Panel Warpage Challenges at Sintering Process”. In: *2022 IEEE 39th International Electronics Manufacturing Technology Conference (IEMT)*. 2022, pp. 1–6. DOI: 10.1109/IEMT55343.2022.9969505.

[21] Hao Zhang, Shijo Nagao, and Katsuaki Suganuma. “Addition of SiC particles to Ag die-attach paste to improve high-temperature stability; grain growth kinetics of sintered porous Ag”. In: *Journal of Electronic Materials* 44 (2015), pp. 3896–3903.

[22] Omid Mokhtari. “A review: Formation of voids in solder joint during the transient liquid phase bonding process-Causes and solutions”. In: *Microelectronics Reliability* 98 (2019), pp. 95–105.

[23] SA Paknejad et al. “Microstructure evolution during 300 C storage of sintered Ag nanoparticles on Ag and Au substrates”. In: *Journal of Alloys and Compounds* 617 (2014), pp. 994–1001.

[24] Maximilian Schmid et al. “Comparison of Nondestructive Testing Methods for Solder, Sinter, and Adhesive Interconnects in Power and Opto-Electronics”. In: *Applied Sciences* 10.23 (2020). ISSN: 2076-3417. DOI: 10.3390/app10238516. URL: https://www.mdpi.com/2076-3417/10/23/8516.

[25] S Chen and H Zhang. “Silver sintering and soldering: Bonding process and comparison”. In: *Die-Attach Materials for High Temperature Applications in Microelectronics Packaging: Materials, Processes, Equipment, and Reliability* (2019), pp. 1–33.

[26] Elviz George and Michael Pecht. “RoHS compliance in safety and reliability critical electronics”. In: *Microelectronics Reliability* 65 (2016), pp. 1–7.

[27] Jingru Dai et al. “Comparative thermal and structural characterization of sintered nano-silver and high-lead solder die attachments during power cycling”. In: *IEEE Transactions on Device and Materials Reliability* 18.2 (2018), pp. 256–265.

[28] Julian Kahler et al. “Pick-and-place silver sintering die attach of small-area chips”. In: *IEEE transactions on components, packaging and manufacturing technology* 2.2 (2011), pp. 199–207.

[29] Xiao Cao et al. “Characterization of lead-free solder and sintered nano-silver die-attach layers using thermal impedance”. In: *IEEE Transactions on Components, Packaging and Manufacturing Technology* 1.4 (2011), pp. 495–501.

[30] Zhiqiang Wang et al. “A 50-kW air-cooled SiC inverter with 3-D printing enabled power module packaging structure and genetic algorithm optimized heatsinks”. In: *IEEE Transactions on Industry Applications* 55.6 (2019), pp. 6256–6265.

[31] Alexander Sewergin et al. “Highly Integrated Switching Cell Design based on Copper Diamond Heat Spreader, 3D Printed Heat Sink and HTCC Logic Board”. In: *CIPS 2020; 11th International Conference on Integrated Power Electronics Systems*. VDE. 2020, pp. 1–6.

[32] Prashanth Konda Gokuldoss, Sri Kolla, and Jürgen Eckert. “Additive manufacturing processes: Selective laser melting, electron beam melting and binder jetting—Selection guidelines”. In: *materials* 10.6 (2017), p. 672.

[33] Aarief Syed-Khaja, Philip Patino Perez, and Joerg Franke. “Production and characterization of high-temperature substrates through selective laser melting (SLM) for power electronics”. In: *2016 IEEE CPMT Symposium Japan (ICSJ)*. 2016, pp. 255–258. DOI: 10.1109/ICSJ.2016.7801276.

[34] E. Huerta et al. “Universal testing machine for mechanical properties of thin materials”. In: *Revista mexicana de fisica* 56 (Aug. 2010), pp. 317–322.

[35] W. Broughton. “Testing the Mechanical, Thermal and Chemical Properties of Adhesives for Marine Environments”. In: May 2012. ISBN: 9781845694524. DOI: 10.1016/B978-1-84569-452-4.50006-0.

[36] Linli Zhu and Xiao-Jing Zheng. “Influence of interface energy and grain boundary on the elastic modulus of nanocrystalline materials”. In: *Acta Mechanica* 213 (Sept. 2010), pp. 223–234. DOI: 10.1007/s00707-009-0263-3.

[37] Shanshan Zhang et al. “Thermal ratchetting effect of AMB-AlN ceramic substrate: Experiments and calculations”. In: *Ceramics International* 45.12 (2019), pp. 14669–14674. ISSN: 0272-8842. DOI: https://doi.org/10.1016/j.ceramint.2019.04.186.

[38] H.B. Motra, J. Hildebrand, and A. Dimmig-Osburg. “Assessment of strain measurement techniques to characterise mechanical properties of structural steel”. In: *Engineering Science and Technology, an International Journal* 17.4 (2014), pp. 260–269. ISSN: 2215-0986. DOI: https://doi.org/10.1016/j.jestch.2014.07.006. URL: https://www.sciencedirect.com/science/article/pii/S2215098614000597.

[39] J.R. Davis. *Tensile Testing, 2nd Edition*. ASM International, 2004. ISBN: 9781615030958. URL: https://books.google.nl/books?id=5uRIb3emLY8C.

[40] Christoph Deininger. *Copper machining with lasers: How to benefit from the advantages and to overcome the obstacles*. 2011.

[41] Xuliu. “Pressure-assisted CU sintering for SiC Die-attachment application”. PhD thesis. Delft University of Technology, 2023.

[42] Nicolas Heuck et al. “Analysis and Modeling of Thermomechanically Improved Silver-Sintered Die-Attach Layers Modified by Additives”. In: *IEEE Transactions on Components, Packaging and Manufacturing Technology* 1.11 (2011), pp. 1846–1855. DOI: 10.1109/TCPMT.2011.2167154.

A

Warpage Measurement Equipment

Table A.1: Summary of warpage measurement equipment-1

Equipment	Keyence-Laser	Keyence-Laser	Keyence-VR
Location	EKL Lab	Nexperia	Aerospace department
Sample	Sintered BSM sample		
Dimension	53 mm × 2 mm	25 mm × 49 mm	53 mm × 49 mm
Measurement time	2.5 hours	3 hours	3 mins
Measurement Detail	• Using 10X magnification lens • Stitching 53 pictures • Measurement result : 241 μm	• Using 5X magnification lens • Stitching 187 pictures • Measurement result : 252 μm	• Calculated triangulation of reflected light • Stitching 6 pictures • Measurement result : 270 μm
Result data	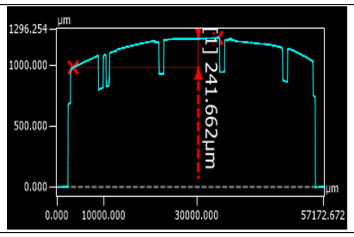	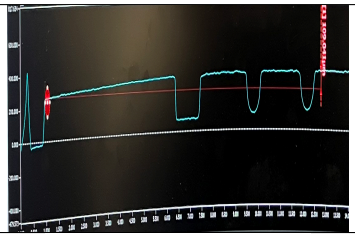	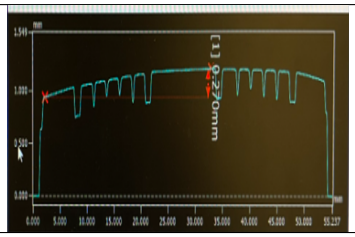
Result picture	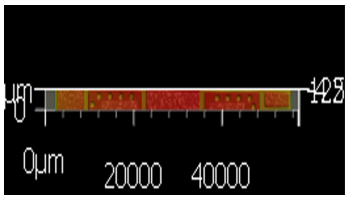		
Equipment picture	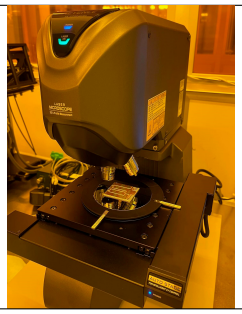		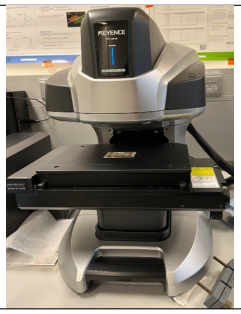
Conclusion	• Measurement speed : Long • Accuracy:High • Only measure the middle line	• Measurement speed : Medium • Accuracy:High-medium • Measure half side of substrate	• Measurement speed : Fast • Accuracy:High-medium •Measure the whole substrate

Table A.2: Summary of warpage measurement equipment-2

Equipment	White light interferometer(WLI)	WLI ContourX-500	SNEOX
Location	PME department	Kavli Lab	STInstruments
Sample	Sintered BSM sample		BSM sample
Measurement dimension	53 mm × 2 mm	1.8 mm × 1.8 mm	53 mm × 49 mm
Measurement time	30 mins	2 mins	
Measurement detail	• Stitching 26 pictures • Measurement result : 313 μm	• No Stitching • Measurement result : 231 μm	• Outsourced measurement • Confocal Optical profilers
Result data	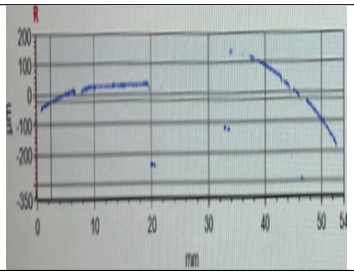	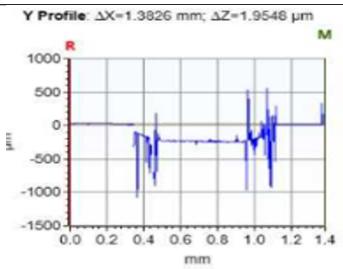	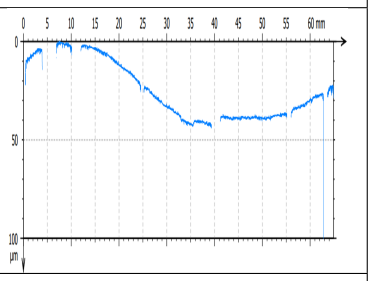
Result picture	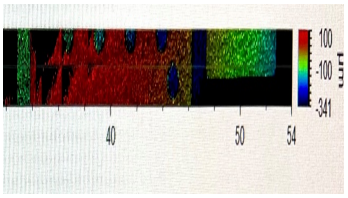	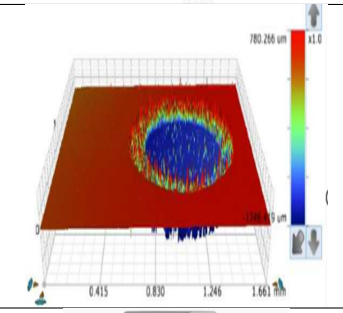	
Equipment picture			
Conclusion	• Measurement speed : Medium • Accuracy : Low • Only measure the middle line • Data missing with height variance.	• Measurement speed : Medium • Accuracy : High • Measure a small hole on the substrate • Data missing with height variance.	• Accuracy : Low •Measure the whole substrate

Table A.3: Summary of warpage measurement equipment-3

Equipment	SWIDE	Keyence Optical	scan CONTROL
Location	STInstrument	Applied science department	Aerospace department
Sample	BSM sample		
Measurement dimension	53 mm × 2 mm	1.8 mm × 1.8 mm	53 mm × 49 mm
Measurement time		1 min	Real-time
Measurement detail	• Outsourced measurement • Integrated digital microscope	• No Stitching • Measurement result : 71.5 μm	• Real time laser scanner
Result data	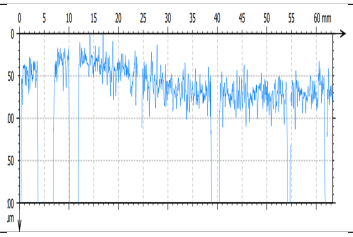	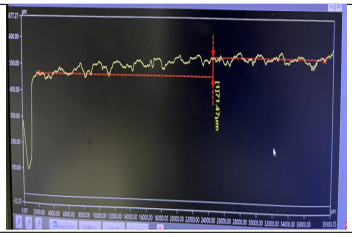	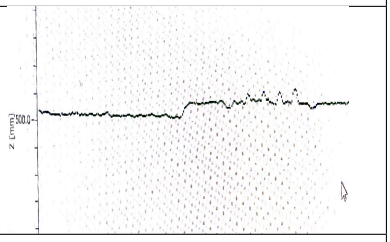
Result picture		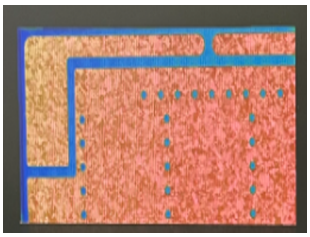	
Equipment picture			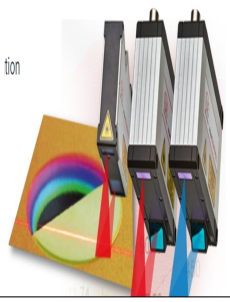
Conclusion	• Accuracy : Low • Measure the whole substrate • Result data has too much variance	• Measurement speed : Fast • Accuracy : Medium • Measure quarter of the substrate	• Measurement speed : Fast • Accuracy : Low • Measure one middle line of substrate •Real time data but too much noise

B

CTE Measurement Equipment

Table B.1: Summary of CTE measurement equipment

Equipment	TMA	Dilatometer	TMA
Location	Fudan University	Material science department	Aerospace department
Sample	Annealed Copper		
Dimension	10 mm × 10 mm × 0.8 mm	10 mm × 4 mm × 0.8 mm	10 mm × 4 mm × 0.8 mm
Heating/ Cooling rate	5 °C/ min	1 °C/ sec	5 °C/ min
Temperature setup	• From 20 °C to 900 °C • Staying at highest temperature for 10 mins		
Result data	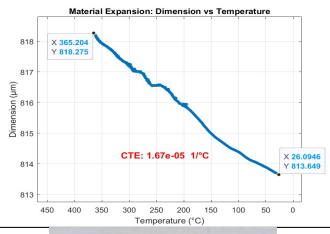	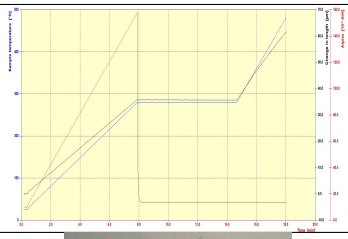	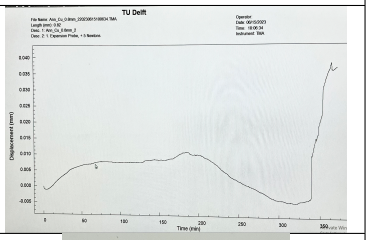
Result picture			
Equipment picture		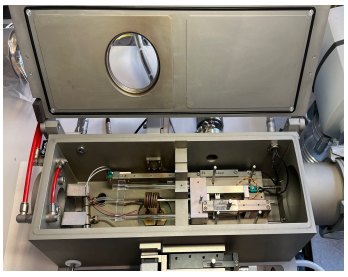	
Conclusion	• Nitrogen gas during heating • No serious degradation deposited on the sample	• Measurement speed : Fast • No degradation happened •Unable to measure high conductivity material	• Using Nitrogen gas during heating • Serious degradation deposited on the sample

C

FEM Simulation Results for Factor Analysis

Table C.1: FEM simulation results for factor analysis-1

	Factor 1	Factor 2	Factor 3	Factor 4	Factor 5	Factor 6	Response 1
Run	A:cuh [mm]	B:cuh2 [mm]	C:cubh [mm]	D:gapf [mm]	E:gapb [mm]	F:gap [mm]	Warpage [um]
1	0.8	0.3	0.3	1.5	0.5	1.5	-564.4
2	0.55	0.55	0.158	1	1	1	-870.2
3	0.8	0.8	0.8	0.5	1.5	0.5	59.4
4	0.3	0.8	0.8	0.5	1.5	0.5	649.8
5	0.3	0.8	0.3	0.5	0.5	0.5	-755.1
6	0.55	0.55	0.55	1.8	1	1	165.7
7	0.8	0.3	0.8	0.5	0.5	1.5	890.8
8	0.8	0.8	0.3	1.5	0.5	0.5	-1142.5
9	0.94	0.55	0.55	1	1	1	-508.4
10	0.8	0.8	0.3	0.5	0.5	0.5	-1167.6
11	0.55	0.55	0.55	1	1	1	131
12	0.8	0.3	0.8	1.5	0.5	1.5	884.5
13	0.3	0.3	0.3	1.5	0.5	1.5	146.8
14	0.8	0.8	0.8	1.5	1.5	0.5	75.9
15	0.55	0.55	0.55	1	1	1	131
16	0.8	0.3	0.8	0.5	1.5	0.5	805.5
17	0.8	0.8	0.8	1.5	1.5	1.5	103.6

Table C.2: FEM simulation results for factor analysis-2

	Factor 1	Factor 2	Factor 3	Factor 4	Factor 5	Factor 6	Response 1
Run	A:cuh [mm]	B:cuh2 [mm]	C:cubh [mm]	D:gapf [mm]	E:gapb [mm]	F:gap [mm]	Warpage [um]
18	0.8	0.3	0.8	1.5	0.5	0.5	868.4
19	0.55	0.55	0.55	1	1	1	131
20	0.3	0.8	0.8	0.5	1.5	1.5	632.1
21	0.8	0.8	0.3	1.5	1.5	0.5	-1046.6
22	0.3	0.3	0.3	0.5	1.5	1.5	86.1
23	0.3	0.3	0.8	1.5	1.5	0.5	1221.2
24	0.3	0.8	0.8	1.5	0.5	1.5	767.3
25	0.3	0.3	0.3	1.5	1.5	1.5	108.8
26	0.8	0.3	0.8	0.5	0.5	0.5	872.6
27	0.3	0.3	0.3	0.5	0.5	1.5	117.7
28	0.55	0.158	0.55	1	1	1	678.4
29	0.55	0.55	0.55	1	1	1	131
30	0.55	0.55	0.94	1	1	1	1127
31	0.8	0.3	0.3	0.5	0.5	0.5	-671.1
32	0.3	0.8	0.3	0.5	1.5	0.5	-732.4
33	0.8	0.3	0.3	0.5	1.5	0.5	-595.3
34	0.3	0.8	0.8	0.5	0.5	1.5	741.3
35	0.3	0.8	0.3	1.5	0.5	0.5	-716.2
36	0.3	0.8	0.3	1.5	1.5	0.5	-701
37	0.55	0.55	0.55	1	1	1	131
38	0.3	0.8	0.8	1.5	1.5	1.5	661.1
39	0.8	0.8	0.8	1.5	0.5	0.5	106.1
40	0.3	0.8	0.8	0.5	0.5	0.5	763.6
41	0.8	0.8	0.8	1.5	0.5	1.5	131.1
42	0.3	0.8	0.8	1.5	1.5	0.5	688.3
43	0.3	0.3	0.8	0.5	0.5	0.5	1352.8
44	0.55	0.94	0.55	1	1	1	-503.8
45	0.55	0.55	0.55	1	1	0.22	91.7
46	0.8	0.3	0.3	0.5	1.5	1.5	-500.8
47	0.3	0.3	0.8	1.5	0.5	0.5	1351.4
48	0.55	0.55	0.55	1	1	1	131
49	0.55	0.55	0.55	1	1	1	131
50	0.3	0.3	0.3	1.5	1.5	0.5	86.6
51	0.3	0.3	0.8	1.5	0.5	1.5	1347.2
52	0.3	0.3	0.3	0.5	0.5	0.5	63.8
53	0.8	0.8	0.3	0.5	1.5	1.5	-949.4

Table C.3: FEM simulation results for factor analysis-3

	Factor 1	Factor 2	Factor 3	Factor 4	Factor 5	Factor 6	Response 1
Run	A:cuh [mm]	B:cuh2 [mm]	C:cubh [mm]	D:gapf [mm]	E:gapb [mm]	F:gap [mm]	Warpage [um]
54	0.8	0.8	0.3	0.5	1.5	0.5	-1063.5
55	0.8	0.3	0.3	1.5	1.5	0.5	-597.6
56	0.3	0.3	0.3	1.5	0.5	0.5	93.1
57	0.3	0.3	0.8	0.5	1.5	0.5	1224.3
58	0.3	0.8	0.8	1.5	0.5	0.5	790.4
59	0.8	0.8	0.8	0.5	0.5	0.5	85.9
60	0.3	0.8	0.3	1.5	0.5	1.5	-613.2
61	0.3	0.8	0.3	0.5	1.5	1.5	-635.1
62	0.8	0.3	0.8	0.5	1.5	1.5	827.4
63	0.3	0.3	0.8	1.5	1.5	1.5	1218.9
64	0.8	0.8	0.3	1.5	1.5	1.5	-931.3
65	0.8	0.8	0.8	0.5	0.5	1.5	114.8
66	0.158	0.55	0.55	1	1	1	595.7
67	0.8	0.3	0.3	1.5	0.5	0.5	-664.3
68	0.8	0.8	0.3	1.5	0.5	1.5	-1017.6
69	0.55	0.55	0.55	1	1	1	131
70	0.3	0.8	0.3	1.5	1.5	1.5	-604.1
71	0.8	0.3	0.3	1.5	1.5	1.5	-503.3
72	0.8	0.8	0.8	0.5	1.5	1.5	89.1
73	0.55	0.55	0.55	1	1	1.8	169.5
74	0.8	0.8	0.3	0.5	0.5	1.5	-1044.1
75	0.3	0.3	0.8	0.5	0.5	1.5	1350.5
76	0.55	0.55	0.55	1	1	1	131
77	0.3	0.8	0.3	0.5	0.5	1.5	-650.1
78	0.8	0.3	0.8	1.5	1.5	1.5	818.2
79	0.55	0.55	0.55	1	1	1	131
80	0.8	0.3	0.8	1.5	1.5	0.5	800.2
81	0.3	0.3	0.8	0.5	1.5	1.5	1221.2
82	0.8	0.3	0.3	0.5	0.5	1.5	-569.9
83	0.55	0.55	0.55	1	1.8	1	94.9
84	0.55	0.55	0.94	1	1	1.8	1126.8
85	0.55	0.55	0.55	1.8	1.8	1	124.3
86	0.55	0.94	0.94	1	1	1	621.7
87	0.55	0.55	0.55	1	1	1.8	169.5
88	0.94	0.94	0.94	1	1	1	69.8
89	0.94	0.55	1.5	1	1	1	1399
90	0.94	0.94	0.55	1	1	1	-937